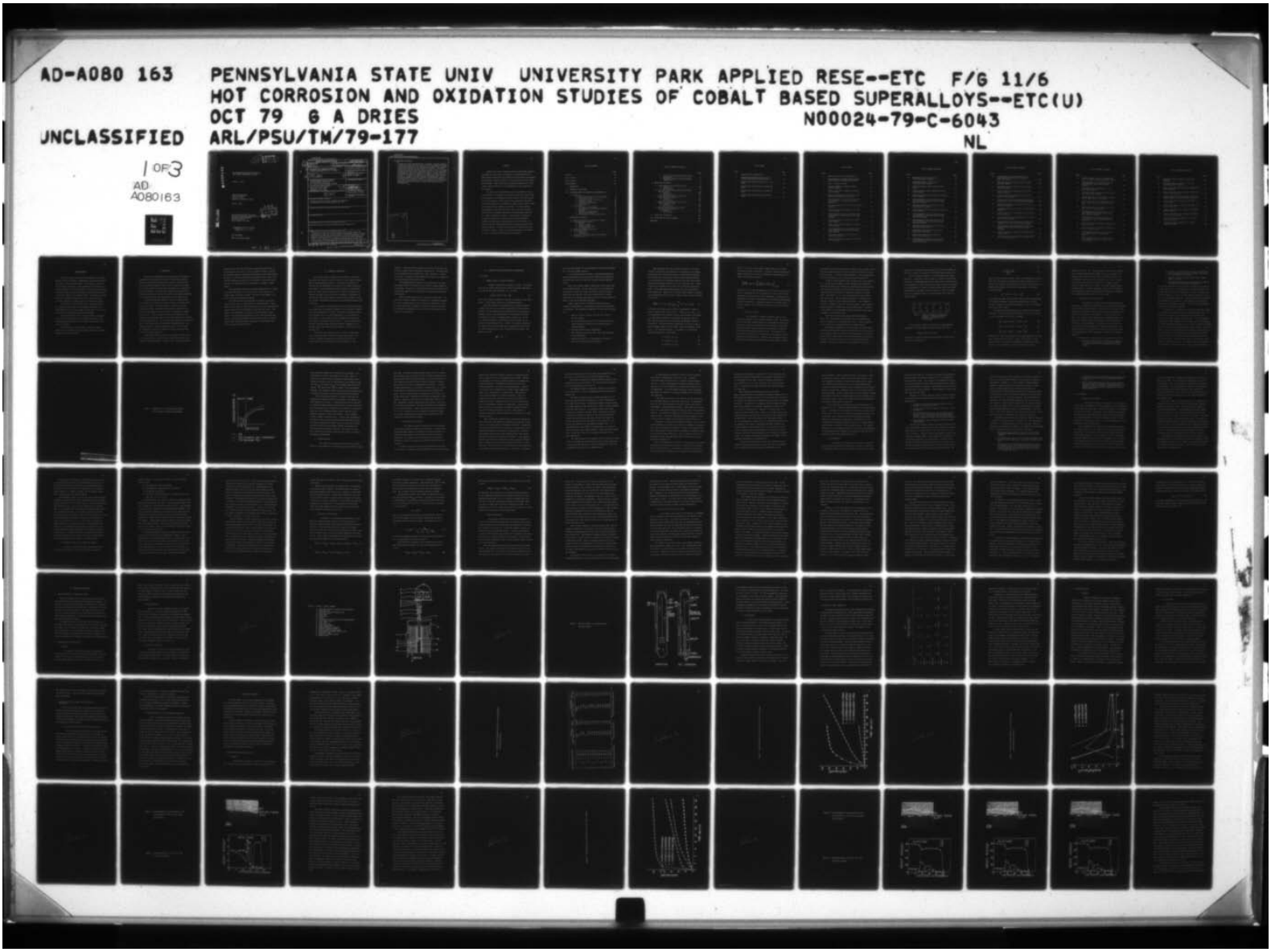
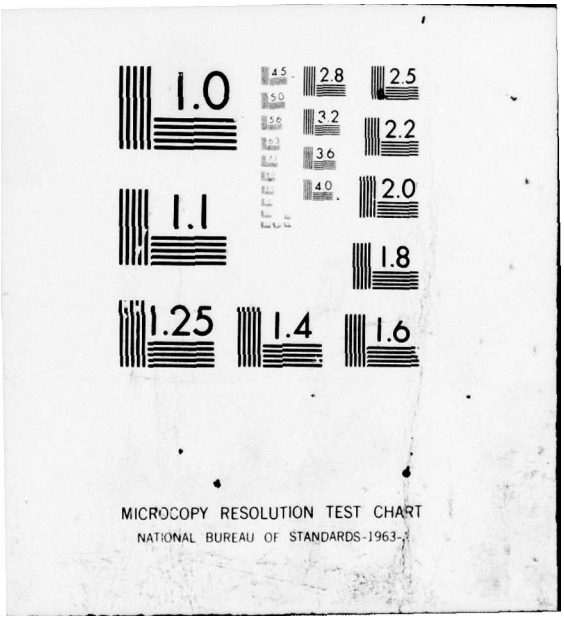
AD-A080 163 PENNSYLVANIA STATE UNIV UNIVERSITY PARK APPLIED RESE--ETC F/G 11/6
HOT CORROSION AND OXIDATION STUDIES OF COBALT BASED SUPERALLOYS--ETC(U)
OCT 79 G A DRIES N00024-79-C-6043
UNCLASSIFIED ARL/PSU/TM/79-177 NL

1 OF 3
AD
A080163




1.0
1.1
1.25
1.4
1.6
1.8
2.0
2.2
2.5
2.8
3.2
3.6
4.0
4.5
5.0
5.6
MICROCOPY RESOLUTION TEST CHART
NATIONAL BUREAU OF STANDARDS-1963-

(12) LEVEL II

AD A080163

HOT CORROSION AND OXIDATION STUDIES OF COBALT BASED SUPERALLOYS AT 1000°C

Gregory A. Dries

Technical Memorandum
File No. TM 79-177
October 9, 1979
Contract No. N00024-79-C-6043

Copy No. 12

DDC
RECEIVED
JAN 28 1980
A

The Pennsylvania State University
Institute for Science and Engineering
APPLIED RESEARCH LABORATORY
Post Office Box 30
State College, PA 16801

DDC FILE COPY

APPROVED FOR PUBLIC RELEASE
DISTRIBUTION UNLIMITED

NAVY DEPARTMENT

NAVAL SEA SYSTEMS COMMAND

80 1 28 013

UNCLASSIFIED

SECURITY CLASSIFICATION OF THIS PAGE (When Data Entered)

REPORT DOCUMENTATION PAGE

READ INSTRUCTIONS BEFORE COMPLETING FORM

1. REPORT NUMBER: ARL/PSU/TM 79-177
2. GOVT ACCESSION NO.: (9) Master's Thesis
3. RECIPIENT'S CATALOG NUMBER:
4. TITLE (and Subtitle): (6) HOT CORROSION AND OXIDATION STUDIES OF COBALT BASED SUPERALLOYS AT 1000°C.
5. TYPE OF REPORT & PERIOD COVERED: MS Thesis, November 1979
6. PERFORMING ORG. REPORT NUMBER: TM 79-177
7. AUTHOR(s): (10) Gregory A. Dries
8. CONTRACT OR GRANT NUMBER(s): (15) N00024-79-C-6043
9. PERFORMING ORGANIZATION NAME AND ADDRESS: The Pennsylvania State University, Applied Research Laboratory, P. O. Box 30, State College, PA 16801
10. PROGRAM ELEMENT, PROJECT, TASK AREA & WORK UNIT NUMBERS:
11. CONTROLLING OFFICE NAME AND ADDRESS: Naval Sea Systems Command, Department of the Navy, Washington, D.C. 20362 — (11) 9
12. REPORT DATE: October 9, 1979
13. NUMBER OF PAGES: 206 pages & figures
14. MONITORING AGENCY NAME & ADDRESS (if different from Controlling Office): (12) 207
15. SECURITY CLASS. (of this report): Unclassified, Unlimited
15a. DECLASSIFICATION/DOWNGRADING SCHEDULE:
16. DISTRIBUTION STATEMENT (of this Report): Approved for public release, distribution unlimited, per NSSC (Naval Sea Systems Command), 10/23/79
17. DISTRIBUTION STATEMENT (of the abstract entered in Block 20, if different from Report):
18. SUPPLEMENTARY NOTES:
19. KEY WORDS (Continue on reverse side if necessary and identify by block number): superalloys, cobalt, corrosion, oxidation, sodium sulfate, hot
20. ABSTRACT (Continue on reverse side if necessary and identify by block number):

Recently, the trend in superalloy design has been aimed toward the development of alloys which are resistant to the harmful effects of sodium sulfate formed within gas turbines operated in marine environments. This phenomenon, commonly referred to as hot corrosion, has been extensively studied. These studies have elucidated the mechanism of sodium sulfate attack and have led to the development of alloys resistant to hot corrosion.

One approach to the development of alloys resistant to hot corrosion involves the formation of a protective oxide layer based on SiO_2. The

DD FORM 1 JAN 73 1473 EDITION OF 1 NOV 65 IS OBSOLETE

UNCLASSIFIED

391 007

SECURITY CLASSIFICATION OF THIS PAGE (When Data Entered)

20. ABSTRACT (Continued)

feasibility of this approach has been verified. The data reported in this study agree well with those of other investigators and show a significant increase in the resistance of alloys to hot corrosive attack with increased silicon content of the alloys. Two rather limiting observations were made from this study. First, the scales forming on the high silicon containing alloys were very susceptible to spalling as a result of temperature changes. A means should be developed to increase the adherence of these scales onto the metal substrate. Secondly, the high silicon containing alloys were very brittle and probably could not withstand the mechanical stresses occurring within operating turbines. It would be more feasible for these alloys to be utilized as a surface coating on an alloy whose mechanical properties are more in accord with turbine material requirements.

Accession For
NTIS GRA&I
DDC TAB
Unannounced
Justification
By
Distribution/
Availability Codes
Dist. Avail and/or special
A

ABSTRACT

Recently the trend in superalloy design has been aimed toward the development of alloys which are resistant to the harmful effects of sodium sulfate formed within gas turbines operated in marine environments. This phenomenon, commonly referred to as hot corrosion, has been extensively studied. These studies have elucidated the mechanism of sodium sulfate attack and have led to the development of alloys resistant to hot corrosion.

One approach to the development of alloys resistant to hot corrosion involves the formation of a protective oxide layer based on SiO_2. The feasibility of this approach has been verified. The data reported in this study agree well with those of other investigators and show a significant increase in the resistance of alloys to hot corrosive attack with increased silicon content of the alloys. Two rather limiting observations were made from this study. First, the scales formed on the high silicon containing alloys were very susceptible to spalling as a result of temperature changes. A means should be developed to increase the adherence of these scales onto the metal substrate. Secondly, the high silicon containing alloys were very brittle and probably could not withstand the mechanical stresses occurring within operating turbines. It would be more feasible for these alloys to be utilized as a surface coating on an alloy whose mechanical properties are more in accord with turbine material requirements.

TABLE OF CONTENTS

	Page
Abstract	iii
List of Tables	vi
List of Figures	vii
Acknowledgments	xii
I. INTRODUCTION	1
II. STATEMENT OF OBJECTIVES	3
III. LITERATURE SURVEY AND THEORETICAL CONSIDERATIONS	5
A. Oxidation	5
1. Wagner's Theory of Parabolic Oxidation	5
2. Point Defect Theory	8
3. Oxidation of Cobalt Based Alloys	12
4. Superalloy Design	16
5. Oxidation of Superalloys	17
6. Scale Behavior	22
B. Hot Corrosion	25
1. The Nature of the Problem	25
2. Environmental Conditions and Combustion Chemistry	27
3. Formation of Sodium Sulfate	30
4. General Considerations	32
5. Hot Corrosion of Cobalt Based Alloys	34
IV. EXPERIMENTAL PROCEDURES	41
A. General Description of Experimental Methods	41
B. Thermogravimetric Analysis	41
1. Balance	41
2. Reaction Chamber	42
3. Furnace and Controller	42
4. Gas Preparation	47
C. Material and Sample Preparation	48
D. Experimental Method	51
1. Oxidation	51
2. Hot Corrosion	52
E. Examination of Scales Formed After Oxidation and Hot Corrosion	53

TABLE OF CONTENTS (Continued)

		Page
	1. X-ray Diffraction (Debye-Sherrer Powder Techniques)	53
	2. Microprobe Analysis and Metallographic Examinations	54
V.	RESULTS AND DISCUSSION	55
	A. Cobalt-Chromium-Silicon-Yttrium Alloys	55
	1. Oxidation	55
	2. Hot Corrosion	86
	B. G.E. X-40 Series (Silicon and Silicon-Yttrium Modified Alloys)	108
	1. Oxidation	108
	2. Hot Corrosion	121
	C. Haynes 188 Series (Silicon and Silicon-Yttrium Modified Alloys)	128
	1. Oxidation	128
	2. Hot Corrosion	139
	D. Haynes 157 Series (Silicon and Silicon-Yttrium Modified Alloys)	151
	1. Oxidation	151
	2. Hot Corrosion	160
	E. Mar-M302 Series (Silicon and Silicon-Yttrium Modified Alloys)	170
	1. Oxidation	170
	2. Hot Corrosion	177
VI.	SUMMARY AND CONCLUSIONS	186
VII.	SUGGESTIONS FOR FUTURE RESEARCH	188
	REFERENCES	189

LIST OF TABLES

Table		Page
1	Commercial Alloy Compositions	49
2	Parabolic Rate Constant Data $\Delta m/A$ for the Cobalt-Chromium-Silicon-Yttrium Alloys	58
3	Parabolic-Rate Constant Data for G. E. X-40 Series	111
4	Parabolic-Rate Constant Data for Haynes 188 Series	129
5	Parabolic-Rate Constant Data for Haynes 157 Series	152
6	Parabolic-Rate Constant Data for Mar-M302 Series	171

LIST OF FIGURES

Figure		Page
1	Cobalt oxide as a p-type semiconductor	10
2	Representation of alloying addition effects on the internally oxidized zone thickness	15
3	Balance - Furnace Assembly	44
4	Reaction chambers for oxidation and hot corrosion studies	46
5	($\Delta m/A$) versus time of oxidation of Co-5 Cr-0.2 Y-Si alloys	60
6	Parabolic oxidation rates of Co-Cr-0.2 Y-Si alloys versus weight percent silicon	62
7	Photomicrograph of the cross-section of the scale formed on Co-5 Cr-0.2 Y-5 Si after *oxidation*	65
8	Microprobe profile of Co-5 Cr-0.2 Y-5 Si after oxidation	65
9	($\Delta m/A$) versus time of oxidation of Co-10 Cr-0.2 Y-Si alloys	69
10	Photomicrograph of the cross-section of the scale formed on Co-10 Cr-0.2 Y-2.5 Si after oxidation	71
11	Microprobe profile of Co-10 Cr-0.2 Y-10 Si after oxidation	71
12	($\Delta m/A$) versus time of oxidation of Co-15 Cr-0.2 Y-Si alloys	74
13	Photomicrograph of the cross-section of the scale formed on Co-15 Cr-0.2 Y-1 Si alloy after oxidation	77
14	Microprobe profile of Co-15 Cr-0.2 Y-5 Si alloy after oxidation	77
15	($\Delta m/A$) versus time of oxidation of Co-20 Cr-0.2 Y-Si alloys	80

LIST OF FIGURES (Continued)

Figure		Page
16	Microprobe profile of Co-20 Cr-0.2 Y-2.5 Si alloy after oxidation	82
17	Microprobe profile of Co-20 Cr-0.2 Y-10 Si alloy after oxidation	82
18	Parabolic oxidation rates of Co-Cr-0.2 Y-Si alloys	85
19	(Δm/A) versus time of hot corrosion of Co-5 Cr-0.2 Y-Si alloys	89
20	(Δm/A) versus time of hot corrosion of Co-10 Cr-0.2 Y-Si alloys	91
21	Photomicrograph of the cross-section of the scale formed on Co-10 Cr-0.2 Y-2.5 Si alloy after hot corrosion	94
22	Microprobe profile of Co-10 Cr-0.2 Y-2.5 Si alloy after hot corrosion	94
23	(Δm/A) versus time of hot corrosion of Co-15 Cr-0.2 Y-Si alloys	96
24	Photomicrograph of the cross-section of the scale formed on Co-15 Cr-0.2 Y-2.5 Si alloy after hot corrosion	99
25	Photomicrograph of the cross-section of the scale formed on Co-15 Cr-0.2 Y-5 Si alloy after hot corrosion	99
26	Microprobe profile of Co-15 Cr-0.2 Y-2.5 Si alloy after hot corrosion	101
27	Microprobe profile of Co-15 Cr-0.2 Y-5 Si alloy after hot corrosion	101
28	(Δm/A) versus time of hot corrosion of Co-20 Cr-0.2 Y-Si alloys	105
29	Photomicrograph of the cross-section of the scale formed on Co-20 Cr-0.2 Y-1 Si alloy after hot corrosion	107

LIST OF FIGURES (Continued)

Figure		Page
30	Photomicrograph of the cross-section of the scale formed on Co-20 Cr-0.2 Y-5 Si alloy after hot corrosion	107
31	Microprobe profile of Co-20 Cr-0.2 Y-1 Si alloy after hot corrosion	110
32	Microprobe profile of Co-20 Cr-0.2 Y-5 Si alloy after hot corrosion	110
33	(Δm/A) versus time of oxidation of G. E. X-40 + Si set of alloys	113
34	(Δm/A) versus time of oxidation of G. E. X-40 + Si + 0.2 Y set of alloys	116
35	Photomicrograph of the cross-section of the scale formed on G. E. X-40 + 5 Si alloy after oxidation	118
36	Microprobe profile of G. E. X-40 + 2.5 Si + 0.2 Y alloy after oxidation	120
37	Microprobe profile of G. E. X-40 + 5 Si alloy after oxidation	120
38	(Δm/A) versus time of hot corrosion of G. E. X-40 + Si set of alloys	123
39	(Δm/A) versus time of hot corrosion of G. E. X-40 + Si + 0.2 Y set of alloys	125
40	Photomicrograph of the cross-section of the scale formed on G. E. X-40 alloy after hot corrosion	127
41	Photomicrograph of the cross-section of the scale formed on G. E. X-40 + 10 Si alloy after hot corrosion	127
42	(Δm/A) versus time of oxidation of the Haynes 188 + Si set of alloys	132
43	(Δm/A) versus time of oxidation of the Haynes 188 + Si + 0.2 Y set of alloys	134

LIST OF FIGURES (Continued)

Figure		Page
44	Parabolic oxidation rates of the Haynes 188 series of alloys versus weight percent silicon	136
45	Photomicrograph of the cross-section of the scale formed on Haynes 188 alloy after oxidation	138
46	Microprobe profile of Haynes 188 + 2.5 Si alloy after oxidation	141
47	Microprobe profile of Haynes 188 + 2.5 + 0.2 Y 0.2 Y alloy after oxidation	141
48	(Δm/A) versus time of hot corrosion of Haynes 188 and Haynes 188 + 7.5 Si alloys	143
49	(Δm/A) versus time of hot corrosion of Haynes 188 + 2.5 Si alloy and of Haynes 188 + 5 Si alloy	145
50	(Δm/A) versus time of hot corrosion of Haynes 188 + Si + 0.2 Y set of alloys	147
51	Photomicrograph of the cross-section of the scale formed on Haynes 188 + 2.5 Si + 0.2 Y alloy after hot corrosion	150
52	Photomicrograph of the cross-section of the scale formed on Haynes 188 alloy after hot corrosion	150
53	(Δm/A) versus time of oxidation of Haynes 157 + Si set of alloys	155
54	(Δm/A) versus time of oxidation of Haynes 157 + Si + 0.2 Y set of alloys	157
55	Photomicrograph of the cross-section of the scale formed on Haynes 157 alloy after oxidation	159
56	Photomicrograph of the cross-section of the scale formed on Haynes 157 + 2.5 Si + 0.2 Y after oxidation	159

LIST OF FIGURES (Continued)

Figure		Page
57	Microprobe profile of Haynes 157 alloy after oxidation	162
58	Microprobe profile of Haynes 157 + 7.5 Si + 0.2 Y alloy after oxidation	162
59	($\Delta m/A$) versus time of hot corrosion of Haynes 157 + Si set of alloys	165
60	($\Delta m/A$) versus time of hot corrosion of Haynes 157 + Si + 0.2 Y set of alloys	167
61	Photomicrograph of the cross-section of the scale formed on Haynes 157 alloy after hot corrosion	169
62	($\Delta m/A$) versus time of oxidation of Mar-M302 + Si set of alloys	173
63	($\Delta m/A$) versus time of oxidation of Mar-M302 + Si + 0.2 Y set of alloys	176
64	($\Delta m/A$) versus time of hot corrosion of Mar-M302 + Si set of alloys	179
65	($\Delta m/A$) versus time of hot corrosion of Mar-M302 + Si + 0.2 Y set of alloys	181
66	Microprobe profile of Mar-M302 + 2.5 Si alloy after hot corrosion	184
67	Microprobe profile of Mar-M302 + 5 Si alloy after hot corrosion	184

ACKNOWLEDGMENTS

The author wishes to express his deep gratitude to Dr. George Simkovich for his suggestions, recommendations and inspiration during the conduct of this research project. He also wishes to thank the Applied Research Laboratory at The Pennsylvania State University for financial support of this research project, as well as General Electric Corporation, Cabot Corporation, and Howmet Turbine Components Corporation for their material and equipment support. Furthermore the author would like to express his appreciation to Dr. Earle Ryba for his invaluable assistance in completing the x-ray diffraction analysis.

The assistance of Mr. John Daly and Dr. George Simkovich in the design and construction of the experimental apparatus, of Mr. Leland Eminhizer in the electron probe microanalysis, and of Mr. Bruce Warnes and Mr. Mark Prugar is gratefully acknowledged.

The author would also like to thank the faculty, the graduate students and the technical staff of the Metallurgy Section of The Pennsylvania State University for their varied contributions to the author's development.

With deep sincerity he also wishes to express his utmost appreciation to his family for their continual support and assistance throughout the author's education.

I. INTRODUCTION

Under certain circumstances an accelerated rate of oxidation of high-temperature alloys has been observed. Within the gas turbine industry, this accelerated oxidation is referred to as hot corrosion. It is a particularly aggressive attack, and is caused by the fluxing of the normally protective oxide layers responsible for a superalloy's oxidation resistance. The metallurgical problems associated with hot corrosion within the hot sections of gas turbine power generating plants or jet engines have been under investigation for over twenty years.

The general mechanisms involved in the hot corrosion process are initiated by the deposition of sodium sulfate on the turbine blade and nozzle materials. The sodium sulfate is formed in a reaction between alkali salts, principally sodium chloride, ingested with air in marine environments; and sulfur, present as an impurity, primarily from fuel oils. The hot corrosion problem has been enhanced by the utilization of increasingly higher turbine inlet temperatures to improve operating efficiencies (1), and increased turbine usage in marine environments. This requires very critical material characterization. To an increasing degree, in aircraft engine applications, it is no longer the time-rupture strength, but rather the corrosion resistance which is the life-limiting factor (2).

Several ideas have been considered as possible solutions to the hot corrosion problem. Among the present possibilities is the use of corrosive inhibiting additions to the fuel oils. This method has been

discarded on the basis that the increased engineering difficulties are not warranted by the severity of the hot corrosion problem. Currently two acceptable methods of approaching the problem are under investigation. The first is to alloy the base metal with components which promote self-protection against hot corrosion by the formation of protective scales that are, to a certain extent, less susceptible to fluxing by sodium sulfate.

The second method involves the mechanical application of a coating to the base alloy before it is put in service. This coating may be either ceramic or metallic in nature. The current trend appears to be in the utilization of protective coatings.

Much work has been done concerning the promotion of Cr_2O_3 and Al_2O_3 protective scales on high temperature turbine materials. Recent studies on both cobalt and nickel based alloys (3,4), have shown promising results associated with the formation of SiO_2 protective scales. This study has been undertaken as a follow-up on these preceding investigations. The idea has been extended to the more complicated superalloy systems. Cobalt-based superalloys have been chosen because it has been reported that cobalt-based alloys are superior to nickel-based alloys under hot corrosion conditions (5,6).

II. STATEMENT OF OBJECTIVES

Hot corrosion, being a highly accelerated form of corrosion on high temperature alloys, has been the subject of many scientific investigations and professional conferences. The primary mechanism of hot corrosion has been established to be fluxing of the normally protective solid oxide by a low melting alkali sulfate, present as a liquid phase. Most solid oxides formed on superalloys are electronic conductors, and therefore the growth of the solid scale is governed by the movement of ionic species. When these scales are liquefied due to fluxing by a salt, ionic motion is dramatically increased, and an accelerated oxidation rate is observed.

If scale growth is controlled by the motion of electronic species in the solid state, an accelerated oxidation rate should not be observed even upon liquefication of the scale. The motion of electronic species is not as much a function of the existing phase, as is the motion of ionic species. In this respect, an ionic conducting scale should be less effected to fluxing by alkali sulfates. It has been verified that the alloys containing higher silicon percentages, independent of the chromium content, were generally less susceptible to the effects of hot corrosion (4).

To obtain an ionic conducting scale, a series of cobalt-based alloys containing chromium, silicon and yttrium were produced. Also four major commercial superalloys were modified with silicon and yttrium, with the hope of forming an SiO_2 scale which is an ionic

conductor. Yttrium was added to promote the formation of the SiO_2 scale and also to improve scale morphology and adherence (7). The cobalt-based alloys investigated may be divided into 3 basic categories: I, Co-Cr-Si-Y alloys, II, commercial alloys modified with silicon, III, commercial alloys modified with silicon and yttrium.

The investigation was conducted to gain insight into the interrelationships between the elements and the scales in complex commercial alloy systems. The effects of silicon and yttrium as alloy additions and the resulting changes in scale composition and morphology are important considerations.

Kinetic studies were conducted to ascertain reaction rates. All alloys were oxidized at 1000°C in dry oxygen at 0.1 atmospheric pressure. For the hot corrosion studies, the specimens were coated with 1 mg/cm^2 of sodium sulfate prior to oxidation. The scales formed on the alloys were examined by metallographic, x-ray diffraction and microprobe techniques as noted previously.

III. LITURATURE SURVEY AND THEORETICAL CONSIDERATIONS

A. Oxidation

1. Wagner's Theory of Parabolic Oxidation

Oxidation is generally an exothermic process. The driving force for the reaction results from the Gibbs free energy change associated with the metal oxide formation. For a reaction,

$$M + \frac{1}{2}O_2 \rightarrow MO \quad \Delta G_f^\circ = \Delta H_f^\circ - T\Delta S_f^\circ \tag{1}$$

and the free energy of formation of the oxide is negative for most metal oxides. In this respect oxidation is a spontaneous process.

Some fifty years ago, it was observed that at high temperatures a compact scale will act as a barrier and decrease the rate of metal oxidation. At high temperatures the oxidation rate will eventually be dependent upon the solid state diffusion of the reactants across the oxide layer if the scale is adherent, compact and pore free. As the oxide thickness increases, the diffusion distance increases and the reaction rate decreases with time. If $\Delta m/A$, the increase in weight per unit surface area is plotted versus time, a parabola will result, and if $(m/A)^2$ is plotted versus time, a straight line will result. This parabolic rate law

$$\left(\frac{\Delta m}{A}\right)^2 = Kp \cdot t \tag{2}$$

first derived by Tammann (8), and independently by Pilling and Bedworth (9), is the most commonly observed.

As the oxidation process continues, concentration gradients of reactants associated with the oxide scale formation are formed within the oxide itself; this is to say that a chemical potential gradient occurs.

There are an infinite number of variations of oxide scales that can be formed on metals. The goal with respect to scale formation is the pursuit of a pore-free, compact and adherent layer on the metal which grows at a slow rate. This type of oxide layer will afford protection to the substrate metal and will act as a barrier between the metal or alloy and the oxidizing environment.

Wagner's theory (10,11) of parabolic oxidation produces a fundamental understanding of the mechanisms occurring in high temperature oxidation. The preliminary assumptions to be noted are as follows (12):

1. Applies to compact, adherent, and pore free scales of reaction products.
2. The rate determining process for the total reaction is the volume diffusion of reacting ions (or point defects) or electron transport.
3. Electrons and ions migrate independently.
4. Phase boundary reactions are rapid since volume diffusion is rate determining.
5. Reactants and oxide are in thermodynamic equilibrium at the metal/oxide and gas/oxide interfaces.

High temperature oxidation proceeds as a result of solid state diffusion of metal ions and electrons in the direction of the oxide/gas boundary with cation point defects moving to the metal/oxide interface. The situation may be reversed and anion or electron holes may diffuse in the direction of the metal/oxide interface (with anion point defects moving to the oxide/gas interface) or, both of these may occur. Volume diffusion is the primary means of anion and cation motion through the oxide. At low temperatures grain boundary and surface diffusion may become significant. Wagner (10,11), derived, among a number of relations, the following equation for the flux of anions J_1 and/or cations J_2 within a solid oxide.

$$\frac{d(n/q)}{dt} = J_1 + |J_2| = \frac{1}{\Delta x}\left\{\frac{1}{|Z_2|F^2}\int_{\mu_0'}^{\mu_0''}(t_1 + t_2)\, t_3\, \sigma d\mu_0\right\} \qquad (3)$$

$d(n/q)/dt$ is the oxidation rate in terms of equivalents of oxidation products formed per unit cross section, q, (cm^2), per unit time. Δx is the instantaneous scale thickness in cm, Z_2 is the valence of the anions, μ_0 is the chemical potential of the nonmetal, μ_0' and μ_0'' are the nonmetal chemical potentials at the metal/oxide and oxide/gas interfaces, respectively. The total electrical conductivity is σ and t_1, t_2 and t_3 are the transport numbers for the cations, anions and electrons, respectively. F is the Faraday constant. The transport (or transference numbers) are defined by the following:

$$t_1 = \ell_1/(\ell_1 + \ell_2 + \ell_3) \qquad (4)$$

$$t_2 = \ell_2/(\ell_1 + \ell_2 + \ell_3) \qquad (5)$$

$$t_3 = \ell_3/(\ell_1 + \ell_2 + \ell_3) \qquad (6)$$

where ℓ_1, ℓ_2 and ℓ_3 are the specific conductivities of the cations, anions and electrons, respectively. In terms of diffusion coefficients, Wagner's equation for the case of an electronic semiconducting scale takes on the following form (11):

$$\left[\frac{d(n/q)}{dt} = \frac{1}{\Delta x} \; Ceq \int_{a_0'}^{a_0''} \left(\frac{Z_1}{|Z_2|} D_1^* + D_2^*\right) d\ell n \; a_0\right]_{t_3 \tilde{=} 1} \qquad (7)$$

where $Ceq = Z_1 C_1 = |Z_2| C_2$ and represents the concentration of cations or anions in equivalents per cm^3, D_1^* and D_2^* are the tracer self-diffusion coefficients for the cation and anion, respectively. a_0' and a_0'' are the thermodynamic activities of the nonmetal at the metal/oxide and oxide/gas interfaces respectively. A significant feature of the Wagner theory of parabolic oxidation is the correlation with the theory of point defects in solids.

2. Point Defect Theory

The formation of a compact, protective oxide is due to solid state diffusion of the reactants through the oxide. The mechanism by which solid state diffusion may occur in oxides may be understood in terms of the formation of imperfections or point defects in the oxide. These point defects include cation and anion vacancies, interstitial ions, quasi-free electrons and electron holes. The mobility of the electrons and electron holes is much greater than point defects such as vacancies and interstitial ions. Therefore non-stoichiometric oxides which contain equivalent concentrations of electronic defects and ionic

point defects are essentially electronic semiconductors, and growth of the electronic conducting compound will be controlled by diffusion of one or both of the ions. In terms of transport numbers, t_3 will be essentially one, and the quantity $(t_1 + t_2)$, will be much less than one (14).

Consider a totally opposite case, the case of pure ionic conductivity. In this case the numbers of cation and anions are essentially equivalent to maintain stoichiometry and therefore electrical neutrality. Ionic conducting compounds are characterized by having much greater concentrations of ionic defects as compared to electrons or electron holes. The quantity $(t_1 + t_2)$ will be essentially one and t_3 will be much less than one. The rate controlling species is, therefore, the electronic species for ionic conducting compounds. A good example of this type of compound is AgCl (15), where the number of cation vacancies equals the number of interstitial cations (Frenkel defect). Diffusion of the cations is then accomplished by jumps into vacant lattice sites or movement via interstitial sites.

Electronic semiconducting compounds were first modeled by Wagner (16). Kubaschewski (14) and Hauffe (15) have subdivided this group of compounds into 3 classifications; p-type, n-type and intrinsic. P- and n-types are of primary importance in oxidation studies.

Semiconducting compounds of the n-type variety are characterized as having an internal defect structure consisting of excess metal cations and an equivalent number of quasi-free electrons located on interstitial lattice sites or anion vacancies with an equivalent number of quasi-free electrons. ZnO which has the first type of point defect structure described in the previous sentence is a good example of this type of

compound (15). The Wagner theory predicts that for n-type compounds the electrical conductivity decreases with increasing oxygen pressure (17).

CoO is an excellent example of a p-type semiconducting compound (14,18,19). A deficiency in metal cations or an excess of interstitial anions with a corresponding number of electronic defects (electron holes) is characteristic of p-type semiconducting oxides. Electrical neutrality may be maintained by the creation of higher valence state cations which are equivalent to the number of electron holes, $\oplus$. Electron movement occurs via an exchange between the lower and higher valent cations as shown in Figure 1.

$O^{=}$	Co^{+3}	$O^{=}$	Co^{++}	$O^{=}$	Co^{++}
Co^{++}	$O^{=}$	$\square$	$O^{=}$	Co^{++}	$O^{=}$
$O^{=}$	Co^{+3}	$O^{=}$	Co^{++}	$O^{=}$	Co^{++}

Figure 1. CoO as an example of a p-type semiconductor. Trivalent cobalt ions represent the location of the electron holes.

The point defect equation representing the high temperature equilibrium of CoO with oxygen is written as (20), (21), (13):

$$\frac{1}{2}O_2(g) \rightleftarrows V(Co)' + \oplus + CoO \qquad (8)$$

where V(Co)' represent a monovalent cation vacancy. The mass action balance may be expressed as:

$$K = \frac{[V(Co)'] \cdot [\oplus]}{P_{O_2}^{1/2}} \tag{9}$$

where K is the equilibrium constant. Since the concentration of electron holes, $[\oplus]$, must equal the concentration of cobalt vacancies, we can combine this restriction with equation (9) and obtain the relation of the oxygen partial pressure with the defect concentration. This may be written as follows:

$$[\oplus] = [V(Co)'] \approx \text{Const.} \cdot P_{O_2}^{1/4} \tag{10}$$

By increasing the oxygen partial pressure the point defect concentration will increase, resulting in an increased oxidation rate. This was predicted by Wagner and confirmed by Bridges et al. (22), in the temperature range of 950 to 1150°C.

The effects of alloying elements can be predicted on the basis of this model. The three major alloying additions Cr, Si, and Y, utilized in this investigation, will be used as examples.

$$\tfrac{1}{2}O_2 + Cr_2O_3 \rightleftarrows 2Cr(Co)^{\cdot} + 2V(Co)' + 4CoO \tag{11}$$

$$\tfrac{1}{2}O_2 + SiO_2 \rightleftarrows Si(Co)^{\cdot\cdot} + 2V(Co)' + 3CoO \tag{12}$$

$$\tfrac{1}{2}O_2 + Y_2O_3 \rightleftarrows 2Y(Co)^{\cdot} + 2V(Co)' + 4CoO \tag{13}$$

Equations (11), (12), (13) represent the new equilibrium defect stoichiometry resulting from the addition of Cr_2O_3, SiO_2, and Y_2O_3 in solid solution in CoO. In general the introduction of higher valent cations increases the concentration of cobalt ion vacancies as shown in

equations (11), (12), (13). The end result is that electrical conductivity is decreased and diffusion through the scale is increased. The oxidation rate of cobalt has been shown to increase with up to 9 wt % Cr. additions (12,13,14,15), (23), Additions of up to 1 wt % Si have increased the oxidation rate of cobalt (4). At higher concentrations of chromium and silicon, a change in the ionic diffusion control mechanism occurs. In essence this change results from the formation of mixed oxides and/or spinels which hinder ionic diffusion by mechanisms to be explained in greater detail in a later chapter.

3. Oxidation of Cobalt-Based Alloys

The oxidation of alloys is much more complex than that of pure metals. A number of new factors must be considered when interpreting how the oxidation process continues. Among these are the relative oxygen affinities of the component metals, their respective concentrations, and the mutual solubilities of each component in the alloy and the oxide phase. These factors play an important role in determining oxide scale morphology. Diffusion rates of each component in both the alloy and oxide phases are very important. The importance of these factors together with the external parameters of temperature and pressure of the oxidizing gas must be realized, and the interaction between the factors must be correlated in order to understand and compare alloy oxidation behavior.

Four basic types of alloy oxidation are outlined by Kostad (12):

1. Selective oxidation in which the least noble component of an alloy is selectively or preferentially oxidized to form an outer oxide layer consisting of one phase (23,24).

2) Formation of composite scales consisting of oxides which may be considered to be mutually insoluble, and which do not react with each other (23,25).

3) Formation of scales containing complex oxides (double oxides or spinels).

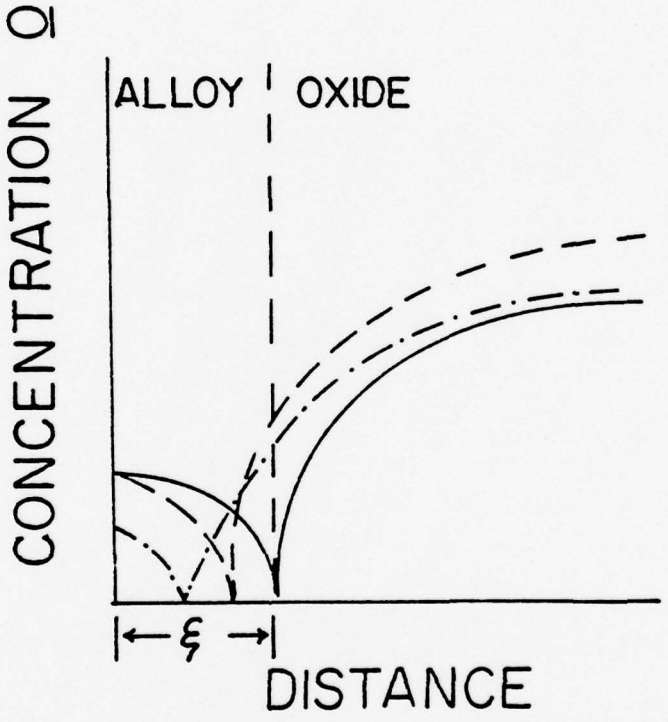
4) The formation of discontinuous oxide particles within the continuous alloy phase (internal oxidation).

At one time or another during the oxidation of complex alloys, each one of these types may occur. The phenomenon of internal oxidation can be very detrimental to the life of superalloys in service. Generally this occurs not because of a loss in the alloy oxidation resistance, but due to a loss in mechanical properties. Selective oxidation occurs along the grain boundaries, and attacks the carbide networks and intermetallic phases present at the grain boundaries. The alloy loses its mechanical hardness and creep rupture properties.

The tendency for a component in an alloy to be internally oxidized may be controlled by further alloying, as outlined by Wagner (24). For a system "Me-I-H," where "Me" represents an alloy component with a relatively low oxygen affinity (example cobalt), "I" is an intermediate oxygen affinity alloy component such as chromium, and "H" is an addition of a high oxygen affinity element such as silicon, the internally oxidized zone (ξ) can be decreased in magnitude, and the formation of a protective oxide layer of "H" can be promoted by three methods. Consider Figure 2: For the system Co-Si, if C_{Si} represents the concentration of silicon, then the thickness of the internally oxidized zone may be reduced by the following means. The first method would be to increase the concentration of silicon in the alloy. This would increase the concentration of silicon in the oxide and decrease ξ. The P_{O_2} could be lowered in

PRECEDING PAGE BLANK - NOT FILMED

Figure 2. Representation of alloying addition effects on the internally oxidized zone thickness.



—— C_{Si}

– – – C_{Si} (increased alloy concentration)

–·–·– C_{Si} (decreased Po_2)

the oxidizing environment as a second means of decreasing ξ. The third method is to add a third element to the alloy. With the addition of an element with an intermediate oxygen affinity such as chromium in solution, since the equilibrium P_{O_2} for Cr/Cr_2O_3 is less than the P_{O_2} for Co/CoO, the P_{O_2} at the oxide/gas interface would be lowered. The overall result would be similar to the second method discussed. The internally oxidized zone (ξ) would be decreased and the concentration of silicon in the external oxide would be increased.

From the preceding discussion, it should be noted that the formation of a protective oxide can be promoted by the addition of a third component to the alloy. A protective oxide layer of SiO_2 would be promoted by adding chromium in solution with the cobalt and silicon. Many investigations have concluded that the formation of a protective oxide layer of an intermediate oxygen affinity metal can also be promoted by additions of more active elements. This is somewhat contrary to Wagner's formulation (24). The major and distinguishing difference is that the more active metal (high oxygen affinity) must be initially associated with oxygen. This is to say that it appears necessary for the more active element addition to be present as a fine oxide particle dispersion (25,27,28). The effects of active metal oxides will be discussed in greater depth later in the section concerning scaling behavior.

4. Superalloy Design

Most commercial superalloys owe their strong oxidation resistance to the formation of a protective Cr_2O_3 layer within the oxide

scale (29). The higher chromium containing alloys, 25 wt % or greater, form continuous Cr_2O_3 layers while the lower chromium containing alloys generally form spinels containing chromium. The spinel particles block ionic diffusion and therefore impart oxidation resistance. Chromium also provides solid solution strengthening in the alloys. At typical chromium concentrations it is necessary to stabilize the f.c.c. modifications present in superalloys and also to raise the stacking fault energy. The most common addition is approximately 10 wt % Ni, but Fe and Mn are also used. Additional solid solution strengthening is often required. Tungsten is often used in the concentration range of 5 to 10%. Molybdenum, niobium and tantalum are often present to aid in the solid solution strengthening. The final strengthening is accomplished by a carbide distribution. Carbon concentrations are usually between 0.5-1.0 wt %; in simple alloys the carbides are chromium-rich $M_{23}C_6$, but in alloys containing high refractory metal concentrations other carbides such as M_6C and MC are present.

5. The Oxidation of Superalloys

The complex alloying of superalloys has been intesively investigated by numerous scientists and researchers. In general there is good agreement between the investigators concerning the effects of numerous alloying elements on the oxidation processes occurring in superalloys. The previous section discussed the role of alloying additions in terms of the mechanical and physical property design of superalloys.

The effects of these and other alloying additions on the oxidation resistance of superalloys have been studied by numerous investigators.

Angerman (30) studied the oxidation resistance of twenty-four superalloys exposed in still air at temperatures up to 1150°C. Chromium was determined to be the most important addition for increasing the oxidation resistance. Molybdenum and tungsten were felt to be slightly beneficial to the overall oxidation resistance. Tungsten is beneficial only at temperatures near 1000°C; higher temperatures result in the volatilization of tungsten oxide. Increasing the silicon content decreases the oxidation resistance. This is in disagreement with other investigators, and will be discussed in greater detail later. Manganese was felt to be only slightly beneficial to the oxidation resistance of superalloys. Iron and nickel showed no effect on the oxidation resistance as expected because of their similar chemical properties to cobalt. Small amounts of lanthanum increased the oxidation resistance for given levels of other alloying elements.

These superficially observed effects of different alloying additions may result from changed scale morphology not directly attributable to the chemical nature of the element in question. Irving et al. (31) studied the effects of Mn, Fe and Ni (f.c.c. stabilizers) on the oxidation resistance of Co-Cr alloys in greater detail. The oxide scales spalled severely from all Mn containing alloys upon cooling. This effect increased with increasing Mn contents. It was suggested that Mn causes the scale to become more brittle, especially CoO-based scales. Contents of less than 15 wt % Mn had little effect on scale morphology. The scales on the Co-Cr-Mn alloys were coarse grained Co-O with an inner layer of spinel particles in a CoO matrix. A manganese-

rich layer existed beneath the outer layer, and was identified to be $(Mn, Co)_2O_4$, a solid solution of cobalt and manganese oxides.

The nickel containing alloys showed an initial increase in the oxidation rate with low Ni contents. The oxidation rate decreases as the Ni content increased over 10 wt % Ni.

Iron additions showed no significant changes in the oxidation rate of Co-Cr alloys. This is in agreement with the observations of Angerman (30).

The effects of tungsten on the oxidation resistance of Co-Cr alloys were investigated by El-Dahshan et al. (32), at temperatures up to 1200°C in pure oxygen. Increasing the tungsten content resulted in a slight reduction on the reaction rate. However, internal oxidation became much less pronounced. At temperatures below 1200°C, $CoWO_4$ formed and was confined to the inner scale. Microanalysis indicated a substantial enrichment of tungsten at the alloy/scale interface. Tungsten does not enter the Cr_2O_3 layer, but acts as a getter in lowering the oxygen activity and assists in Cr_2O_3 formation. This behavior is predicted by an interpretation of Wagner (24). At temperatures greater than 1200°C, the $CoWO_4$ phase is no longer confined to the inner scale. Massive amounts of $CoWO_4$ border the columnar grains of CoO, which result in the increased volatility of WO_3 at these temperatures.

The slight decrease in the oxidation rate with increasing tungsten contents is probably due to the increased amount of $CoWO_4$ reducing the cross sectional area available for diffusion through CoO. There were no tendencies for $CoWO_4$ to form a completed layer.

The high temperature oxidation of Co-20% Cr alloys containing tantalum were investigated by Irving et al. (29). In general, tantalum increased the oxidation rate if present in amounts greater than 5 wt %. Small tantalum amounts accelerated oxidation, whereas additions of 6 wt % were beneficial to lowering the oxidation rate at all temperatures. The oxides present were Cr_2O_3, $CrTaO_4$ and $CoTa_2O_6$. The spinels were effective in lowering the oxidation rate by blocking ionic diffusion.

Scale spalling was severe. CoO, formed as an outer oxide layer, was often absent because it spalled off upon cooling. An intermediate layer rich in Cr with significant Ta and very little Co was found via microanalysis. Internal oxidation occurred. These oxides were Ta-rich with low Co, indicating that Ta_2O_5 and $CrTaO_4$ may form at the alloy/scale interface. The formation of $CrTaO_4$ may be responsible for lowering the oxygen activity at the surface promoting Cr_2O_3 layer formation, in much the same way that W promoted Cr_2O_3 formation in Co-Cr-W alloys (32).

The effects of silicon on the oxidation resistance of Co-Cr alloys differs depending upon whether it is present as an element or associated with oxygen as a dispersed oxide phase. If present as a dispersed oxide phase, small amounts of silicon oxide will promote the formation of Cr_2O_3 layer in Co-Cr and Ni-Cr alloys (27). This is similar to the way that dispersions of Y_2O_3, ThO_2 and Al_2O_3 promote the formation of Cr_2O_3 as described by Stringer (26).

Hock (4), investigated the effects of silicon present as an element. Increasing the silicon content resulted in a decrease in the oxidation rate of Co-15 Cr-Si alloys. The formation of Co_2SiO_4 particles blocks ionic diffusion and is responsible for a decrease in the oxidation rate

associated with Si additions. Deadmore (33), in an investigation concerning the formation and breakdown of the protective Cr_2O_3 layer, due to the presence of water vapor, stated that anything that promotes Cr_2O_3 formation such as Si, will prolong the life of the protective layer. It was stated that higher Si contents will further stablilze the Cr_2O_3 layer.

This interpretation by Deadmore, appears to contradict Wagner's concept (24) and the conclusions presented by Stringer (27). An investigation by Douglass and Armijo (34) into the effects of silicon on the oxidation of nickel-20 wt % chromium-alloys, may resolve this apparent discrepancy. The presence of an amorphous SiO_2 layer between the Cr_2O_3 layer and the substrate was confirmed. Additions of Si below 3 wt % did not form a continuous layer. Additions of Si greater than 3 wt % formed a much more complete layer. However, it was emphasized that high temperatures and/or long times would be required to form a complete and continuous layer. Due to the silicon's very high oxygen affinity, it may not be unreasonable to assume that as the oxidation front moves into the substrate, there exists a preoxidized (internally oxidized) zone consisting mainly of silicon preceding the main oxidation front (28). If this is the case then the main oxidation front would "see", and be chemically affected by SiO_2 particles and not the presence of elemental silicon. The observed results would be expected to be similar to those observed by Stringer (27), and Deadmore (33).

To discuss in detail the role of each alloy addition present in commercial grade superalloys would be beyond the scope of this investigation. However there are two remaining elements which must be

discussed briefly. These are boron and carbon. The presence of boron in superalloys is said to benefit only the mechanical behavior. One theory suggests that because of boron's small atomic size, it tends to fill structural discontinuities that exist at grain boundaries and increase the structural perfection, thereby increasing the bond strength between the grains (35). Chemically, boron is very active and tends to form stable oxides. However, elements such as boron, beryllium, vanadium and columbium were found to be quite harmful due to the formation of low melting point oxides. Either oxide decomposition and/or volatilization destroyed the effectiveness of Cr_2O_3 (36).

The role of carbon in superalloys has been investigated by El-Dahshan et al. (37). Superalloy strength depends on the carbide network $M_{23}C_6$. The formation of this carbide may diminish the chromium content of the matrix. The results of El-Dahshan's investigations indicate that the oxidation rate is increased with increasing carbon percentages. However, the increase was not significant. El-Dahshan et al. (37) concluded that the decreased chromium activity due to carbide formation does not affect the ability to form a protective layer. The chromium availability at the oxide/alloy interface is the important consideration. The mechanical properties, however, may be greatly affected due to the formation of voids in the carbide network (37).

6. Scale Behavior

The ability of an oxide scale to adhere to its substrate material under differing thermal conditions is primarily a function of the difference between the thermal expansion coefficients of the oxide

and the metallic substrate. In general, the greater the difference in thermal expansion coefficients, the greater will be the tendency for the oxide scale to spall. This tendency can be minimized by altering scale growth mechanisms and scale morphology through further additions to the alloy substrate. In general, these additions are in the form of dispersed oxides of active elements. Typical examples are ThO_2, Al_2O_3, CeO_2, Y_2O_3, and SiO_2 (26,27).

Stringer et al. (28,26) discussed four major effects resulting from additions of active element dispersed oxide particles to cobalt-chromium alloys.

1) A reduction in the amount of chromium required to form a continuous, external Cr_2O_3 scale.

2) The rate of scale growth is reduced, particularly at high temperatures.

3) The transport mechanism in the oxide is changed from predominantly metal ion transport to predominantly oxygen transport. (The scale forming reaction is transferred from the oxide/bas interface to the oxide/alloy interface.)

4) Scale adhesion is greatly improved, particularly during thermal cycling.

Many theories have been proposed to explain the effects of dispersed oxide phases. Giggins and Pettit (38), attributed the reduced oxidation rate to a blocking effect by the dispersoid in the inner layer of the scale. Initially the Cr_2O_3 layer grows by normal cation diffusion of chromium outward. This increases the concentration of the dispersoid particles at the alloy surface. Eventually outward movement of chromium is restricted and dissociation of Cr_2O_3 occurs. The released oxygen can now pass around the inert oxide particles and form a new inner layer of Cr_2O_3 incorporating the dispersoid. The

outer layer volatilizes at high temperatures and the scale continues to grow, but at the alloy/oxide interface, thus improving its adhesion to the substrate. Stringer et al. (39), proposed a slightly different mechanism to explain the shift in the position and control of scale growth. Stringer suggests that the dispersoid particles act as nucleation sites for the initially-formed oxides, increasing the number of oxide nuclei and hence accelerating the approach to the steady state scale condition, i.e., Cr_2O_3 layer formation. This would explain the reduction in the amount of chromium necessary in the alloy for Cr_2O_3 layer formation. Stringer further suggests that the reduction in grain size reduces the number of short circuit diffusion paths for chromium, while increasing the oxygen transport via grain boundaries. The final result is that oxygen transport is rate controlling in the scale forming reaction and thus the oxide grows at the alloy/oxide interface.

The adherence of the oxide scale is greatly promoted by this shift in control of the oxidation process. Stringer et al. (28) investigated the effects of Y and Hf additions to Co-Cr-Al alloys under oxidizing conditions at high temperatures (1000°C). They suggested several possible models to account for the excellent adherence of the scales.

1. Mechanical keying or pegging of the oxide to the substrate by selective oxidation of the addition at the scale-alloy interface.

2. The internal particles of the active element additions provide sites for vacancy condensation, eliminating interfacial porosity.

3. The formation of a compound oxide layer between the scale and substrate occurs. This compound oxide has a coefficient of thermal expansion that gradually changes from a value similar to the alloy to a value close to that of the scale, i.e., a graded seal effect.

4. A modification of the oxide plasticity allows accommodation of the thermally induced stresses accompanying thermal cycling.

5. Yttrium becomes incorporated into the scale and eliminates the lateral growth of the oxide. This suppresses the diffusion of chromium and greatly reduces or prevents oxide formation within the scale and the development of a convoluted morphology.

B. Hot Corrosion

1. The Nature of the Problem

Hot corrosion of metals is characterized by sulfidation of surface layers, accompanied by accelerated oxidation. It is an aggressive attack by both sulfur and oxygen. The sulfur is present as a contaminent in the fuel oils burned in jet engines. Hot corrosion was recognized in the 1940's, and is most commonly found in marine gas turbines employed for propulsive machinery and auxiliary equipment in ships. Aircraft flying at low altitudes over the sea or in a marine environment are also susceptible to hot corrosive attack.

The accelerated rate of oxidation occurs when metals and alloys are coated with (a) salts, (b) liquid metal oxides, and (c) mixtures of the two (40). The catastrophic oxidation is initiated by combustion of high sulfur-bearing fuel oils (as high as 3.5 wt %) in the presence of sea salt ingested in the intake air to form Na_2SO_4 (41). Estimates of the amount of sea-salt ingested may vary from 1-5 ppm at altitudes of about 20 ft above sea level, to 0.01 ppm at several thousand feet. DeCrescente and Bornstein (42) have pointed out that the sulfur activity

produced by dissociation of Na_2SO_4 is not sufficient to effect the corrosion of the metal. They concluded that condensation of the salt on the metal had to occur. This is generally agreed upon by the majority of investigators. The salt concentration required in the atmosphere to result in condensation on blade materials has been calculated by DeCrescente and Bornstein (42). It depends on the pressure within the turbine, and hence the compression ratio. This will be discussed in greater detail later.

There are a number of theories which attempt to explain how the condensation of sodium sulfate on an alloy surface causes fluxing of a normally protective oxide layer. Stringer et al. (43) reviewed two proposed fluxing mechanisms. The first model, known as basic fluxing, involves an Na_2SO_4 layer which becomes enriched in oxide ions (more basic) by the loss of sulfur to the alloy to form sulfides. This allows fluxing of the oxide as salt-soluble anionic species. The anions are transported outwards toward the salt/gas interface where the oxygen ion activity is lower. Here they decompose to form oxides again as precipitated particles within the molten salt; a loose, non-protective oxide layer forms. This mechanism has been substantiated in the case of accelerated oxidation observed with nickel base alloys (44,45,42).

Acid fluxing is also possible when the oxide ion content of the molten Na_2SO_4 layer is decreased by the formation of complex ions, such as tungstates or molybdates. The normally protective oxide dissociates and is removed from the alloy surface. With acid fluxing the alloy composition is very important (43).

Another group of investigators (46,47) postulated that the loss of oxidation resistance was due to chromium depletion of the alloy at the alloy/oxide interface by the formation of chromium-rich sulfide precipitates. Quets and Dresher (48), indicated that the formation of alkali compounds, i.e., $NaAlO_2$ or Na_2CrO_4, was the necessary driving force to release sulfur for sulfide formation.

Other impurities, besides sea salts and sulfur, needed for Na_2SO_4 formation, are present both in the fuel gas initially and as combustion residues which enter into the corrosion process. The gas turbine environment contains O_2, H_2, N_2, CO_2, SO_2 and SO_3 gases as well as gaseous, liquid or solid Na_2SO_4, NaCl, Na_2O, V_2O_5, PbO and $PbSO_4$ at high temperature, pressures and velocity. It is evident that the hot corrosion mechanism can become very complex. This was shown by Pontony et al. (49) in an investigation of the effects of V_2O_5 slags on the corrosion of cobalt, and by Bornstein et al. (40) on the effects of vanadium and sodium compounds on the accelerated oxidation of nickel based alloys. The effect of lead compounds in the oxidizing environment on the corrosion resistance of cobalt based alloys, were evaluated by Vialatte and Apert (50). It is however difficult to evaluate test results for comparitive purposes due to the variety of ways hot corrosion degradation can be initiated and the variation in testing procedures.

2. Environmental Conditions and Combustion Chemistry

In order to develop a conceptual understanding of the hot corrosion mechanisms, it is essential that the environmental

conditions within a gas turbine be understood. These environmental factors are (51):

1) Metal temperatures and fluctuations.

2) Gas temperature, compositions and fluctuations.

3) Gas pressure and velocity.

4) Presence of certain impurities in the intake air and in the fuel, e.g., S, Na, V, Pb, etc.

The alloys wihthin a gas turbine are subject to temperatures which depend upon the particular application. Inlet temperatures above 1250°C are not uncommon in a high performance aircraft turbine. Blade materials are cooled and their temperatures are maintained about 850-900°C. Blade surface temperature fluctuations greater than 15°C per second have been acknowledged for turbines operating at constant power settings (52). Blades are also highly stressed; average stresses for an aircraft turbine are 20,000 psi. Normal operation involves thermal cycling of the turbine which affects blade lifetimes. These vary from 5,000 to 10,000 hours. A typical turbine engine is cooled to room temperature and heated up again for 2 to 3 hours running time (51).

The ongoing environmental conditions existing in the gas turbine hot sections are chemically and thermodynamically complex. These conditions can not be considered stoichiometric, or steady state. Residence times in the combustion chamber and the turbine are of the order of five milliseconds. Environmental conditions in the hot section are almost always oxidizing. The possible exception is the existence of reducing conditions during engine starts when carbon is usually present as a result of unburned fuel, and during landing when the turbines

operate with a fuel rich mixture. Fuel/air ratios have been quoted by Tschinkel (53) as about 0.36 at take-off, dropping to 0.2 during cruising and as low as 0.05 during idle. The composition of the ingested sea air will be 0.15-0.20 mole fraction oxygen, 0.73 mole fraction nitrogen and 0.05 mole fraction of both CO_2 and H_2O. One-quarter to one-third of the intake air (primary air) is used in fuel combustion. The remaining three-quarters to two-thirds (secondary-air) is utilized to cool the hot combustion gas going to the first stage of the turbine to acceptable temperature limits, i.e., from approximately 1800-2000°C down to approximately 1000°C. A portion of the cooling air is diverted through the turbine blades for further cooling. The gas pressure, depending on the compression ratio, will be in the 10-20 atm range, traveling at a velocity of Mach 0.9.

During combustion of a fuel containing 0.5 wt % sulfur, the SO_2 concentrations could bec ome of the order of $1x10^{-4}$ mole fraction and the SO_3 concentration will be $0.4x10^{-4}$ to $0.1x10^{-4}$ mole fraction. In actuality the SO_3/SO_2 mole ratio is around 1/100 due to the fact that only a small portion of the intake air is used in fuel combustion; residence times are very short and of the order of 5 to 10 milliseconds (53). The presence of certain impurities in the fuel and intake air is the cause of hot corrosion. The most detrimental are the sodium salts which react with the sulfur oxides, formed by fuel combustion, to form Na_2SO_4. DeCrescente and Bornstein (1), have reported that condensation of Na_2SO_4 should not occur with NaCl concentrations of less than 5 ppm at blade temperatures of 900°C. At temperatures

slightly below 800°C, less than 0.1 ppm of NaCl was required for Na_2SO_4 condensation.

Vanadium is also present in lower grade fuels. Concentrations could become as high as 500 ppm. The vanadium reacts with sodium to form sodium vanadates, which may or may not condense to a significant degree on turbine materials. Gaseous sodium vanadate has been found to only slightly increase the oxidation rate of superalloys, whereas, if present as a condensed liquid phase, it will greatly accelerate the oxidation rate of superalloys. An accepted model of $NaVO_3$ attack states that sodium vanadate fluxes the protective oxide and allows direct oxidation of the metal to occur (54)

3. Formation of Sodium Sulfate

A comparison of the equilibrium vapor pressure of pure NaCl to the partial pressure of NaCl in the turbine section as a function of temperature and pressure was made by DeCrescents and Bornstein (55). They concluded that NaCl was present in the turbine section as a vapor above 725°C for salt concentrations as high as 1 ppm and at pressures from 1 to 20 atm (the engine compression ratio being 20 to 1). Sulfur oxides formed during fuel combustion then react with the NaCl vapor according to the following equations:

$$2NaCl_{(g)} + SO_{2(g)} + 1/2O_{2(g)} + H_2O_{(g)} \rightarrow Na_2SO_{4(g)} + 2HCl_{(g)} \quad (14)$$

and

$$2NaCl_{(g)} + SO_{3(g)} + H_2O_{(g)} \rightleftarrows Na_2SO_{4(g)} + 2HCl_{(g)} \quad (15)$$

Equilibrium constants were calculated for the temperature range of 430-1230°K at constant temperatures. Large values of K_p, 10^{15} at 430°K and 10^7 at 1030°K for reaction (15) indicate that the formation of Na_2SO_4 and HCl was thermodynamically favored over this temperature range. The conversion of NaCl to Na_2SO_4 is expected to be high.

The equilibrium constant, Kp, at 1000°C was then used to calculate the percentage of $NaCl_{(g)}$, present at 1 ppm which can be converted to liquid Na_2SO_4. The equilibrium constant K_x (in terms of mole fraction X of the reactants and products) varies with pressure according to the relationship:

$$K_x = K_p P_t^{-\Delta n} \tag{16}$$

where K_p is the equilibrium constant at constant pressure, and Δn is the sum of the number of moles of gaseous products minus the sum of the number of moles of gaseous reactants. For equation (14), Δn is -2.5

$$K_x = K_p P_T^{2.5} = \frac{X_{HCl}^2}{X_{SO_2} \cdot X_{H_2O} \cdot X_{O_2} \cdot X_{NaCl}^2} \tag{17}$$

At 1000°C and atmospheric pressure it was found that the conversion of NaCl to Na_2SO_4 and HCl was 75 percent complete.

Above 1100°C the conversion of NaCl to NaOH becomes important. This was described by Tschinkel (53), and his considerations were as follows:

$$NaCl_{(g)} + H_2O_{(g)} \rightleftarrows NaOH_{(g)} + HCl_{(g)} \tag{18}$$

NaOH would then further react with SO_3 to form Na_2SO_4 via the following reaction:

$$2NaOH_{(g)} + SO_{3(g)} \rightleftarrows Na_2SO_{4(g)} + H_2O_{(g)} \quad (19)$$

Tschinkel (53), also pointed out that (a) $SO_3(g)$ would be dominant at low gas temperatures during idling, and $SO_2(g)$ would prevail at high temperatures during take off; (b) the formation of Na_2SO_4 vapor could occur only at the lower temperatures existing in the secondary combustion zone; (c) Na_2SO_4 vapor dissociated strongly above 1100°C. As a consequence of a, b, and c, Na_2SO_4 would condense and deposit on turbine airfoils at low power levels such as during idling.

4. General Considerations

An explanation of the hot corrosion is very complex as a result of the many alloys available and the different types of interactions observed with the different alloys when subjected to an environment conducive to hot corrosion. The reaction produces a porous, nonprotective oxide as the principal product. The metal-oxide interface is typically very irregular with intrusions of the oxides into the metal, and particles of the metal isolated within the oxide. The metal ahead of the interface is generally found to contain sulfides, usually chromium rich in most cases (56).

There have been many techniques used to study the hot corrosion reaction. Two principal techniques are the crucible test and the salt coated oxidation test. The crucible test involves the immersion of the test sample up to its midpoint in molten salt contained in a crucible

in still air. This type of test is severe in nature and, in that respect, is advantageous in studies stressing morphological and compositional phenomena. The salt coated test used in this investigation has several advantages over the crucible test. This method involves coating the specimen with a thin layer of salt and oxidizing in an appropriate environment. The advantage of this test is that it can be performed in a conventional thermobalance. Kinetic data may be obtained and the composition of the atmosphere can be readily adjusted allowing better control over the reaction chemistry (56). It has been shown (57) that this method of testing is probably appropriate to weakly corroding conditions and emphasizes the aspect of the reaction in which the protective oxide film is destroyed by being fluxed by the molten salt layer. It does not model well in strongly corroding environments where the penetration of sulfur beneath the oxide plays an important part in the hot corrosion process.

There are many variations of testing procedures used. Many are designed to emphasize a certain aspect of the hot corrosion process. Sulfidation in H_2-H_2S mixtures has been used to study the formation of metal sulfides (57). Presulfidation techniques followed by oxidation have been used to study the effects of sulfides on the oxidation behavior of superalloys (58,59). Burner rig apparatus modified for salt injection are used to study superalloy hot corrosion in conditions which closely simulate the environment within operating gas turbines (60). Care must be exercised when correlating the results of these many testing techniques.

In the models of hot corrosion, the formation of a sulfide is considered secondary; it serves as a mechanism by which the stoichiometry

of the salt may be varied. Numerous investigators have reported that hot corrosion can be induced by sodium carbonate or sodium nitrate coatings. The requirement is that a second oxidant (as well as oxygen) be present and may be removed to allow a stoichiometric displacement (61). El-Dahshan et al. (58,59) have shown that the sulfide may be important in determining the development of the scale morphology in the later stages of attack. It is agreed that the salt fluxing mechanism is responsible for the initial breakdown of the initial oxide layer and may be the dominant mechanism in mildly corrosive environments.

5. Hot Corrosion of Cobalt Based Alloys

Hot corrosion of pure cobalt by the presence of a condensed surface coating does not differ significantly from the oxidation characteristics of pure cobalt. In the case of pure nickel, the coated specimens initially oxidize much faster than the corresponding uncoated nickel specimen but the rate soon dimimishes and becomes less than that of the uncoated nickel (56). This accelerated oxidation is attributed to the basic fluxing model where NiO_2^{-2} ions, created by the reaction of Na_2O with NiO, diffuse to the Na_2SO_4/gas interface where NiO is precipitated, causing the formation of successive oxide layers instead of a compact protective oxide layer.

The "immunity" which cobalt displays toward Na_2SO_4 coatings has been investigated by Johnson et al. (56). Their investigations showed the formation of cobalt sulfides and an increase in the Na_2O content of the salt. Johnson et al. (56) concluded that the increase in oxide ion activity was either not sufficient to form cobaltate ions CoO_2^{2-} or

that this ionic species containing cobalt does not exist. Further investigations with CoO coupons in the presence of Na_2SO_4 made basic by Na_2O additions revealed that CoO_2^{2-} could be formed. Apparently the basicity achieved during the oxidation of Na_2SO_4 coated cobalt specimens is insufficient to cause basic fluxing.

Acid fluxing has been concluded to be the important mechanism in the hot corrosion of cobalt alloys (62), the alloy chemistry being of primary concern. When hot corrosion was first recognized as a problem, it was found that chromium was the key element in preventing severe hot corrosive attack. Davin et al. (63) studied the hot corrosion of Co-10 Cr and Co-30 Cr alloys. At 1000°C the Co-10 Cr alloy was severely corroded while the Co-30 Cr alloy showed good resistance. Several distinct layers were identified: an inner layer consisting of Cr_2O_3, followed by a layer of Cr_2O_3 and CrS, a layer of CoS and finally an outerlayer of CoO. Johnson et al. (62) studied the effects of some individual alloying elements present in the commercial based alloy X-40 (25% Cr, 7.5% W, 10% Ni, 0.5% C, 2% Fe, balance Co) hot corroded at 950°C in pure oxygen. The oxidation of binary Co-Cr alloys was slightly reduced by precoating with Na_2SO_4. Internal sulfidation occurred within the Co-15 Cr alloy with considerable porosity at the alloy/scale interface. The oxide scale was composed of CoO, $CoCr_2O_4$ and Na_2CrO_4, and appeared to be partially fluxed. The Co-25 Cr alloy showed fluxing of the surface scale. Sulfur penetrated into the alloy and chromium-rich sulfide particles precipitated in the grain boundaries. An irregular alloy/scale interface developed due to preferential oxidation of the sulfides. In these tests 25% Cr was just sufficient to form a protective

Cr_2O_3 layer. The presence of chromium results in the solution of chromate ions in the salt which makes the salt more acidic counteracting the basic fluxing mechanism (56). Goward (64) referred to chromium as acting in a "buffering" capacity and neutralizing more acidic species present in the salt. Bergman (65) studied the hot corrosion of various cobalt and nickel base alloys in test stands designed for burning jet engine fuels at low pressure and velocities. He concluded that the higher the chromium content, the greater was the resistance to hot corrosion.

Johnson et al. (62) investigated the role of tungsten on the hot corrosion of Co-Cr alloys. The presence of tungsten in the alloy promoted interaction between the alloy and the salt. This was followed by acid fluxing of the oxide or the metal by the oxide-ion depleted layer of condensed Na_2SO_4. The Co-15 Cr-7.5 W alloy showed considerable porosity in the surface oxide scales; a tungsten-rich region (Na_2WO_4 + WO_3) was present in the alloy/scale interface. The presence of 25% Cr was found sufficient to form a protective Cr_2O_3 layer and prevent tungsten from reacting with the salt and promoting accelerated attack in Co-25 Cr-7.5 W. It was also mentioned that under severe corroding conditions, 25% Cr is insufficient to form an initial Cr_2O_3 layer resulting in acid fluxing of CoO or the unprotected metal, which can continue unabated. Tungsten in the alloy increases the acidity of the salt (56). Johnson (56) noted that a coating of Na_2SO_4 markedly increased the oxidation rate of Co-7.5 W alloys; uncoated samples showed a decrease in the oxidation. Two samples, one of "pure" cobalt and another of Co-7.5 W, were coated with Na_2SO_4 and oxidized at 900°C

for 4 hrs. The cooled specimens were placed in 30 ml of distilled water and boiled in an attempt to leach out any water-soluble salts. The pH of the solutions were measured. The solution from the pure Co specimen had a pH of about 8 and the Co-7.5 W solution had a pH between 5-6 verifying the effect of tungsten to increase the acidity of the salt. Molybdenum was shown to have the same effect as tungsten (64,66).

The scale formed on the Co-7.5 W alloy consisted of an outer porous CoO layer and an inner layer of a tungsten-rich oxide. X-ray diffraction showed that the only sulfide formed was Co_4S_3. Beltran (67) studied that volatilization of refractory element oxides of the type MO_3 is also important. Typical samples of these oxides are TaO_3, WO_3, CbO_3 and MoO_3. Usually present as $CoMO_4$, these refractory oxides lead to the formation of low melting-point mixtures of the type MO_3. Their lack of stability at higher temperatures would tend to promote dissociation to CoO and MO_3, with volatilization of the MO_3 type refractory oxide. Similar experimental evidence points against additions of V and B for the same reason. The presence of acidic oxides may prevent the hot corrosion process from terminating (64).

Johnson et al. (68) studied the effect of Ta and Nb, alternatives to the other solid solution strengthening additions (Mo and W) typically used in cobalt based superalloys. The Na_2SO_4 coating causes a slight acceleration in oxidation rates of Co-4 Nb alloy. A slight reduction occurred with a Co-7.5 Ta alloy. A Nb containing alloy formed a scale typical of acid fluxing: refractory-element rich phases Nb_2O_5 and $Na_2Nb_2O_6$ are present near the alloy/scale interface. An outer porous

mass of CoO developed. In the case of the Co-7.5 Ta alloy, a dense protective CoO layer formed. Seybolt (69) demonstrated that Nb_2O_5, WO_3 and MoO_3 reacted readily with Na_2SO_4. He also found that Ta_2O_5 was even more reactive than Nb_2O_5. It is therefore apparent that tantalum does not promote acid fluxing; however, the reason for this is not yet known.

The effects of iron and manganese additions in Co-25 Cr alloys, have been investigated by Johnson et al. (62) at 950°C under a constant flux of condensing Na_2SO_4. Iron was added to stabilize the f.c.c. structure of the alloys, and was not expected to influence the corrosion behavior. The alloy Co-25 Cr-5 Fe-3 Mn was considerably less attacked than the Co-25 Cr alloy. The formation of a Cr_2O_3 surface layer was promoted although some porosity developed due to sodium chromate formation. It was suggested that manganese-rich sulfides formed at the reaction temperature and reduced the rapid ingession of sulfur and oxygen into the alloy. However, no manganese-rich sulfides were identified. A ternary Co-25 Cr-4 Mn alloy showed similar behavior, confirming that iron played an insignificant role in the hot corrosion of Co-25 Cr alloys.

The effects of yttrium additions to cobalt and Ni base superalloys was evaluated under hot corroding conditions in a jet fuel burner rig apparatus. Elliott and Verma (60), concluded that an enrichment of Cr in the inner layer of the scales was caused by Y additions. Some reduction in the amount of internal sulfidation was also attributed to the presence of Y. Rare earth additions such as Y, present as a dispersed oxide, was investigated by Johnson et al. (62). The rare earth

oxide addition stabilized a compact Cr_2O_3 layer and prevented the formation of internal sulfides. It has been postulated that rare earth oxide may tie up sulfur in the alloy as complex species such as $CeOS_{0.5}$ (70), reducing the inward diffusion of sulfur and the resulting chromium depletion.

The effect of silicon additions have been evaluated by Hock (4) for the case of Co and Co-Cr alloys, and Kerr (3) for the case of Ni and Ni-Cr alloys. Kerr reported that large quantities of silicon, greater than 2.5%, conferred excellent hot corrosion resistance on the alloys. It was reported (71) that SiO_2 can depress the oxide ion content of sodium sulfate. It was further hypothesized that an amorphous SiO_2 layer, formed beneath the Cr_2O_3 layer, may provide resistance to sulfur diffusion. Hock (4) reported similar findings with Co based alloys. Increasing the silicon content decreased the oxidation rate for the samples oxidized under hot corroding conditions. The formation of a thin film of SiO_2 on the alloy surface may be the reason for the low hot corrosion rates. The formation of the spinel Co_2SiO_4 was included to aid in the reduction of the hot corrosion rate. Silicon additions below 1% to commercial Ni base superalloys were reported to be slightly beneficial (72).

The effects of carbon on the oxidation of cobalt-based alloys was investigated by El-Dahshan et al. (59). Co-Cr samples were presulfurized in H_2-H_2S atmospheres sufficient to form cobalt and chromium sulfides. Carbon concentrations in the range of 0-2% were added to test the hypothesis that carbon depletes the chromium concentration via carbide formation reducing chromium's effectiveness in reducing high temperature oxidation and hot corrosion. The conclusion drawn from this

investigation was that carbon additions to a Co-25% Cr alloy progressively increases the oxidation rate but not to as great an extent as a reduction of chromium activity due to carbide formation would warrant. Although the chromium is tied up by the carbon, the exchange reaction

$$Cr_xC_y + \frac{3}{2} x\ S = \frac{1}{2} x\ Cr_2S_3 + yC \qquad (20)$$

is favored thermodynamically, and proceeds with little difficulty. The carbon then released, diffuses inward into the matrix and reacts with chromium and forms new carbides (59).

IV. EXPERIMENTAL PROCEDURES

A. General Description of Experimental Methods

The rate of oxidation and hot corrosion of three major sets of cobalt based alloys were determined via thermogravimetric analysis. The first set, "in house" alloys, consisted of varying amounts of chromium and silicon as the major alloying additions. A small amount of yttrium was added to promote scale adhesion. The second and third sets consisted of four major commercial cobalt based superalloys modified with varying silicon concentrations. The third set was the commercial alloys additionally modified with yttrium.

The oxidation and hot corrosion studies were performed in an atmosphere of dry oxygen at 0.1 atmospheres of oxygen pressure, at 1000°C. The samples to be hot corroded were coated with 1.0 mg/cm^2 of reagent grade sodium sulfate. Scale morphology, structure and element distribution were studied using Debye-Scherrer diffraction techniques, x-ray emission spectrochemical microanalysis (microprobe), and light microscopy.

B. Thermogravimetric Analysis (TGA)

1. Balance

An Ainsworth, Type RV-AU-2S automatic recording semi-microbalance with a full scale range of 10.0 mg, sensitivity of 0.1 mg, readability of 0.01 mg, and reproducibility of $\pm$ 0.02 mg was used to determine weight changes of the sample as a function of time. See

Figure 3 for the balance and furnace set-up. Beam deflections caused by weight changes were transmitted to a strip chart recorder which recorded the weight change as a function of time. A flow of helium was maintained in the bell jar and pyrex tube connecting the balance with the reaction chamber to prevent any corrosive gases from reaching the balance assembly.

2. Reaction Chambers

Two types of reaction chambers were used in these experiments (see Figure 4). Vycor reaction chambers worked well at 1000°C when using helium, hydrogen or oxygen for the high temperature oxidation runs. The hot corrosion experiments required a reaction chamber of high temperature mullite to preclude interaction between hot corrosion reactants and the reaction vessel. Allowance was made to permit the gases to be preheated in the reaction vessel prior to entering the sample area. This preheat assists in maintaining the proper temperature at the sample without temperature gradients between the gas and the gas/oxide interface. Figure 4 indicates the gas flow. Thermocouple wells were constructed as close to the sample area as possible in order to provide more accurate temperature control of the hot zone.

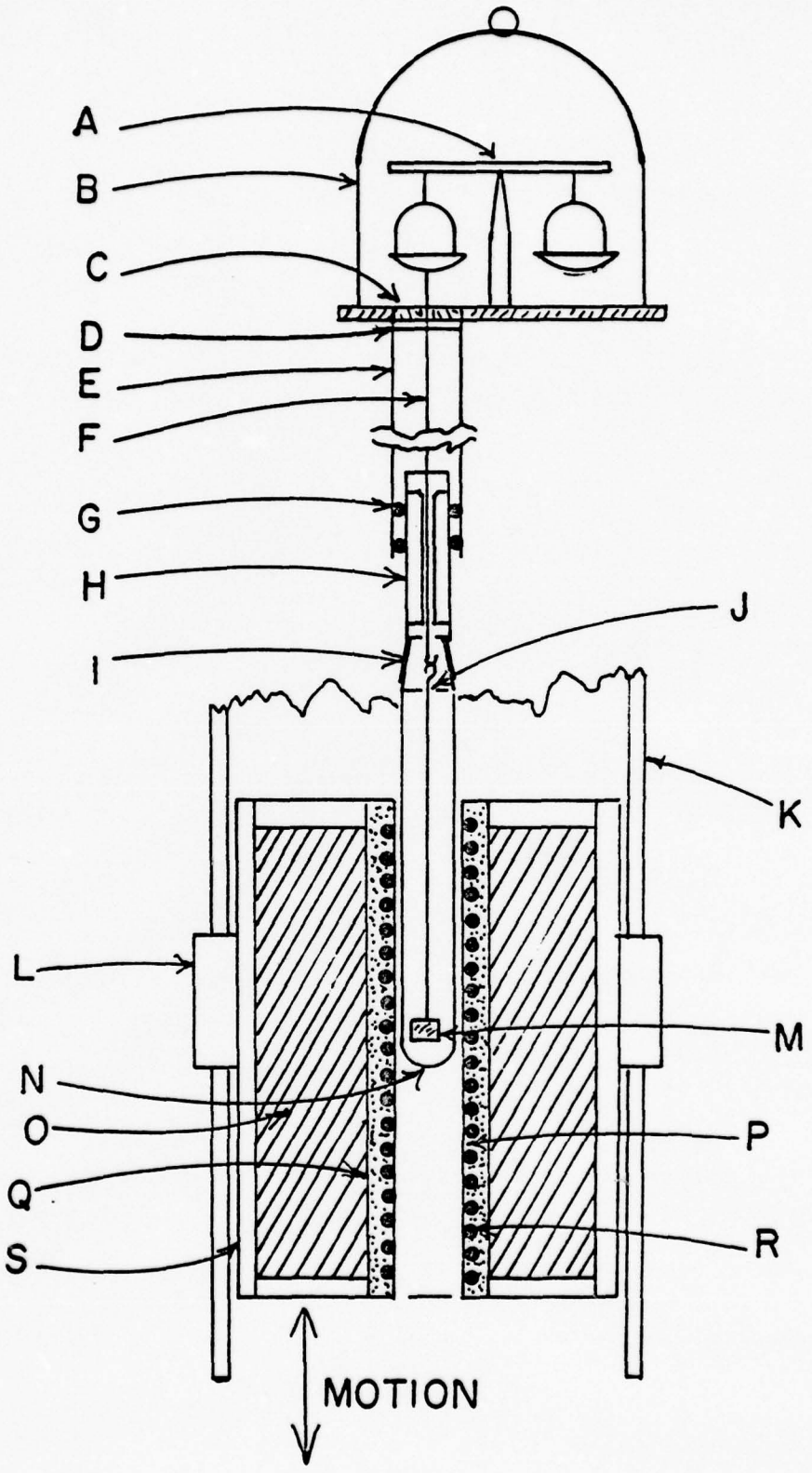
3. Furnace and Controller

The furnace consisted of a Kanthal non-inductively wound (7 turns per inch) high temperature mullite furnace tube cemented with high temperature alumina cement. The furnace tube was insulated with alumina beads and encased in a steel jacket. The hot zone temperature

Blank

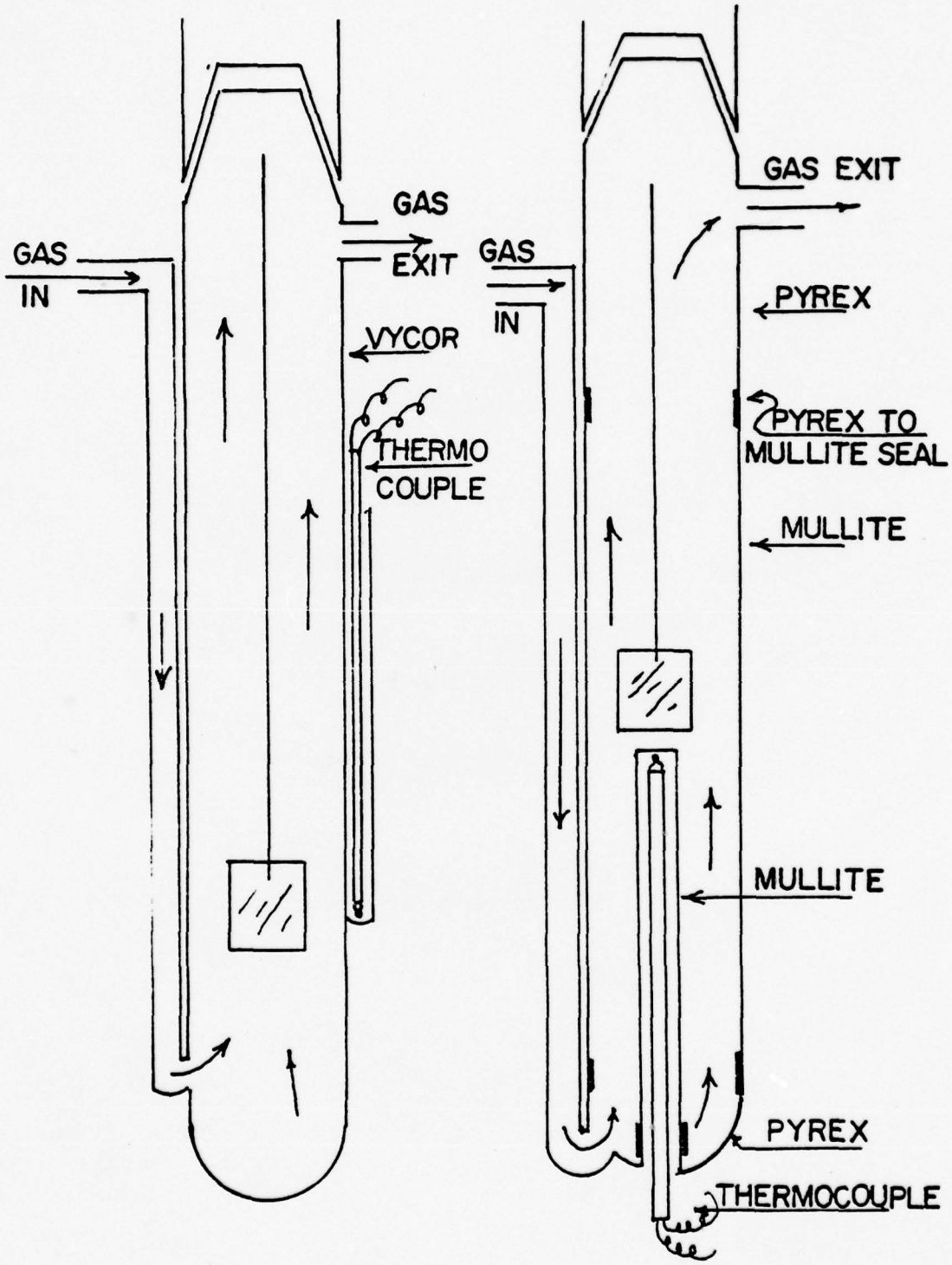
Figure 3. Balance - Furnace Assembly.

A. Ainsworth automatic recording balance (FV-Au-1)
B. Pyrex bell jar
C. Brass disc with 2 mm diameter hole
D. Pyrex-brass seal
E. Pyrex tube
F. Vycor fiber
G. O-ring
H. Pyrex tube 275 mm long with 6 mm inside diameter
I. Ground glass joint
J. Vycor fiber
K. Steel guide rods
L. Furnace guide tubes
M. Sample suspended in hot zone
N. Oxidation reaction chamber
O. Alumina insulating glass beads
P. High temperature mullite furnace tube
Q. Refractory cement
R. Kanthal A-1 furnace winding
S. Furnace shell


A
B
C
D
E
F
G
H
I
J
K
L
M
N
O
P
Q
R
S
MOTION

Blunt

Figure 4. Reaction chambers for oxidation and hot corrosion studies.



OXIDATION HOT CORROSION

was maintained at 1000°C by a Leeds and Northrup controller to within ± 2.0°C using a platinum-platinum 10% rhodium thermocouple. The length of the hot zone was 1.5 inches. The furnace assembly was constructed in such a manner to allow vertical furnace movement. This arrangement permits the furnace to be removed from around the reaction chamber to facilitate removal of the reaction chamber and changing samples. Similar experimental arrangements (3,4) encountered no problems with thermal shocking of the reaction chambers, and therefore no special precautions were taken to prevent thermal shock in this study.

4. Gas Preparation

The gases used in this investigation were commercial grade oxygen, helium, and hydrogen. The hydrogen was passed through a commercial catalytic purifier in order to react any oxygen present as an impurity with hydrogen to form water vapor. The water vapor was then removed by passing the gas through a Drierite ($CaSO_4$) column. The helium was purified by passing it through a copper oxide catalyst at 160°C to remove any hydrogen, present as an impurity, forming water vapor. The gas was next dried by passing it successively through a magnesium perchlorate column, two ascarite columns and a Drierite column. The dry helium was passed through a sintered copper pellet catalyst at 160°C to remove any oxygen present as an impurity. The oxygen gas utilized was dried by passing it through a Drierite column.

Manometric flowmeters were used to regulate the gas flow, so the desired atmosphere could be obtained for the oxidation and hot corrosion experiments. Dibutyl phthalate was used in the manometers and in the

blow-off columns of all flowmeters. The flowmeters were calibrated by measuring the rate at which the gas from a flowmeter displaced a soap bubble up a column of known volume. After the gases were metered, they were passed through a mixing chamber to insure uniform gas composition.

C. Material and Sample Preparation

The commercial superalloys used in this investigation were supplied by General Electric Corporation (G.E. X-40), Martin-Marietta Corporation (Mar-M302), and Cabot Corporation, Haynes Stellite Division (Haynes 188 and 125). The base materials for the "in house" alloys were cobalt metal grade V.P. (99.9% Co) from the Materials Research Corp., silicon metal (99.09% Si, 0.01% Ca, 0.01% Al, 0.49% Fe), electrolytic chromium (99.8% Cr, 0.2% Fe), and yttrium (99.98% Y) turnings. The commercial alloy compositions are listed in Table 1.

The sample alloys were produced by melting the constituent metals or alloys within alumina crucibles, in an induction furnace. Due to the high vapor pressure of yttrium, the yttrium modified alloys were produced by using two melting procedures. First the required amount of yttrium was arc melted with a 4 to 6 gram flat sample of cobalt metal, in the case of the "in house" alloys, or flat sample of superalloy material. The procedure here was to place the yttrium under the cobalt or superalloy pieces. After several pump down and inert gas (argon) purging operations, the melting chamber pressure was reduced to 0.25 atm. This abnormally high arc melting pressure was used to help decrease yttrium losses due to yttrium volatilization. The yttrium was placed below the cobalt or superalloy pieces so that upon melting the yttrium would be

Table 1

Commerical Alloy Compositions
(Nominal Weight Percent)

G. E. X-40

Co	Cr	C	Si	Mn	Fe	Ni	W
52.5	25.2	0.5	1.0	1.0	2.0	11	7.5

Haynes 157

Co	Cr	C	Si	B	W
Bal	21.0	0.07	1.6	2.4	4.5

Haynes 188

Co	Cr	C	Si	Mn	Fe	Ni	W	La
Bal	20-24	.05-.15	.2-.5	1.25 max	3.0	20-24	13-16	.03-.15

Mar-M302

Co	Cr	C	W	B	Zr	Ta
Bal	21.5	.85	10	.005	.2	9.0

immediately blanketed by the molten metal and not directly exposed to the low chamber pressure, to again minimize yttrium losses.

Following the arc melting operation, the weighed constituents were placed in alumina crucibles and melted in an induction furnace under argon. The high silicon containing alloy melts were vacuum degassed prior to solidification, by evacuating the furnace chamber for two minutes. This step was necessary to reduce porosity and segregation revealed in the ingot open sectioning. In several cases the silicon content had to be reduced in order to procure usable ingots. The melted ingots were then solidified and cooled slowly under 1 atm pressure of argon. Several selected alloys were analyzed to ascertain silicon and yttrium concentrations. This analysis showed silicon losses upon melting to be small. Yttrium, however, showed no significant losses and was not present in concentrations greater than 0.01 wt %.

The sample ingots were then vacuum sealed in a vycor tube and homogenized at 1000°C for 24 hrs, and furnace cooled. The ingots were sliced to the approximate thickness using an ultra-thin cut off wheel. Samples were then ground to approximately 14 mm x 10 mm x .7 mm and polished through 600 grit SiC wet paper using standard metallographic sample preparation procedures. The samples used for the oxidation runs had a 1.62 mm (1/16 inch) hole drilled through the sample to facilitate suspending the coupon by quartz fibers from the balance pan. Just prior to suspending the sample in the reaction chamber, the coupon was again polished with 600 grit SiC paper to ensure all oxide films had been removed, and then rinsed with acetone to degrease it. This sample preparation procedure was maintained throughout to ensure a valid comparison and analysis of experimental data.

D. Experimental Method

1. Oxidation

Oxidation experiments were initiated by suspending a sample from the balance into the reaction chamber by quartz fibers. The balance was then tared and calibration checked. Helium flow was then initiated at 180 cc/min, and the entire system (gas lines, reaction chamber, and bell jar balance assembly), was purged for 1 hour. Hydrogen at a rate of about 5 cc/min was then mixed with the helium for 1/2 hour prior to raising the furnace. Following this the furnace was then raised, the helium flow into the reaction chamber was terminated, and hydrogen gas flow was increased to 38 cc/min. The sample was annealed in hydrogen for thirty minutes to remove stresses and to reduce any oxide films that may have remained on the surface. Weight losses were negligible during this time. The hydrogen gas flow was then stopped and helium was introduced at 180 cc/min for 1/2 hour then slowed to 90 cc/min for 1/2 hour to purge the reaction chamber. Next the oxygen, at a flow rate of 10 cc/min, was mixed with the helium to initiate the oxidation process. The partial pressure of oxygen was maintained at 0.1 atm. On termination of the run, the oxygen flow was stopped and the furnace lowered. The sample was cooled to ambient temperature in a helium atmosphere. Run duration was approximately 4200 minutes with some runs lasting only 2400 minutes.

It is estimated that the test samples reached 1000°C in about 30 seconds, and upon cooling attained ambient temperature in approximately 10 minutes (73). Reproducibility of gravimetric data was within $\pm$ 10 percent. Because of the relatively short period of time and an oxidation

temperature of 1000°C, weight gain data corrections due to the oxidation of Cr_2O_3 to CrO_3 gas were neglected. It has been reported that even at 1200°C these effects may be assumed negligible (74).

2. Hot Corrosion

Samples were prepared for hot corrosion by coating the sample with 1 mg/cm^2 of Na_2SO_4. This was done by preheating the coupons with a reducing flame and spraying them with a fine mist of a saturated solution of sodium sulfate. This procedure resulted in depositing a tenacious and uniform coating of sodium sulfate. Coatings were applied with a weight accuracy of $\pm$ .1 mg per total coupon area.

Following this the coupon was hung on a platinum hanger and suspended via a platinum chain into the hot zone of the furnace. The balance was tared and the calibration checked prior to a helium purge of 180 cc/min for 1/2 hour. The helium flow rate was then slowed to 90 cc/min and oxygen flow was initiated at 10 cc/min and mixed with the helium to establish the proper atmosphere. This flow of helium and oxygen was maintained for 1/2 hour prior to raising the furnace.

Following the establishment of the proper atmosphere, the furnace was raised, and the hot corrosion experiment was begun. This procedure was used because it was felt that initiating the hot corrosion process at a lower temperature ($\approx$800°C), caused by heat loss in the process of raising the furnace around the reaction chamber, would be better than waiting for the temperature to reach 1000°C under a non-oxidizing environment. This would result in significant sodium sulfate losses due to vaporization, and would change a parameter that was to be held constant.

Test temperature was reached in 5 minutes. Hot corrosion test duration was 2900 min (48 hrs). Test times varied depending upon individual sample requirements.

E. Examination of Scales Formed after Oxidation and Hot Corrosion

In order to gain insight into the interrelationships between the elements and scales formed during the oxidation and hot corrosion, extensive analyses were undertaken to identify scale composition and elemental distributions. These studies were conducted utilizing Debye-Scherrer powder diffraction techniques, electron microprobe analysis and high magnification light microscopy.

1. X-ray Diffraction (Debye-Sherrer Powder Techniques)

Prior to polishing the oxidized or hot corroded specimens for microprobe and microscopic examination, some of the scale was removed, ground and placed in a glass capillary tube for x-ray analysis. The capillary tube was mounted in the Debye-Scherrer powder diffraction camera, film loaded, and exposed to a collimated beam of FeKα radiation. A manganese oxide filter was used. The samples were exposed for various times ranging from 20 to 30 hours. The samples were rotated through 360 degrees during exposure to reduce any preferred orientation effects. The 2θ angle of each diffraction line was measured and the interplanar spacing (d) for each line was calculated using Bragg's Law. A search manual was used to identify possible compounds. The JCPDF was consulted

for final identification. A compound was considered identified when a match of intensities and d values was obtained.

For thin film oxide layers the oxidized hot corroded specimen was mounted in the camera, so that it made an angle with the beam of 10 to 15 degrees, depending on the oxide film thickness. Qualitative identification of the oxide compounds was made in the same manner as discussed in the previous paragraph.

2. Microprobe Analysis and Metallographic Examination

Prior to microprobe analysis and metallographic examination, the oxidized or hot corroded coupons were mounted in epoxy under vacuum to prevent the oxide layer from spalling during subsequent cross-sectioning and polishing. After the specimens were placed in the sample holder, the system was evacuated. The epoxy was then sucked into the system, and into the sample mounts by the vacuum. After the mounts were filled, the system was opened to air, so the air pressure would help force epoxy into any cracks and pores present in the scale. The mounted coupon was then cross-sectioned and polished through 1.0 μ diamond polish. An ETEC autoprobe with a spot size of 1 to 2 μ, which produced a radiated sample area 5 to 10 times the impinging beam size, was used for the microprobe analysis. The qualitative distributions of all the elements present in each sample, plus oxygen, sodium and sulfur, present in the scale were accomplished through the use of energy dispersive analysis (EDA), elemental x-ray mapping, and concentration profiles. In addition to microprobe analysis, the scale morphology was studied with the aid of a Vickers metallograph. Photomicrographs were taken of representative oxide samples.

V. RESULTS AND DISCUSSION

The basic concept of this research program was the development of a protective external layer of SiO_2 on alloy surfaces. Since SiO_2 is an ionic conducting compound its growth rate, which is controlled by the movements of electrons, should not be increased significantly by the formation of a liquid layer of Na_2SO_4 on the sample surface if electronic conductivity is not simultaneously induced with the formation of the liquid phase.

In order to achieve the formation of an outer SiO_2 layer, high concentrations of silicon, up to 10 wt %, were added to Co-Cr alloys and several commercial superalloys. Wagner (75) predicts that chromium should promote the formation of an external SiO_2 layer. This occurs because Cr_2O_3 will steepen the oxygen chemical potential gradient and prevent silicon precipitation as an internal oxide. The diffusion of silicon to the metal surface may then occur more readily, and a protective layer of SiO_2 is formed beneath the thin previously-formed scale (75,76). The SiO_2 layer formed is often too thin to be detected by metallographic or microprobe techniques.

A. Cobalt-Chromium-Silicon-Yttrium Alloys

1. Oxidation

The kinetics of oxidation of four sets of cobalt-chromium-silicon-yttrium alloys were determined in oxygen at a pressure of 0.1

atmosphere and a temperature of 1000°C. Each set of alloys contained, 1, 2.5, 5 and 10 wt % silicon, and 0.2 wt % Y nominally. The chromium concentrations were 5 wt %, 10 wt %, 15 wt % and 20 wt % chromium. Yttrium was added to these alloys to promote scale adhesion. It is important to mention again that chemical analysis of selected samples failed to identify any yttrium concentrations greater than 0.01 wt % in the alloys. Significant yttrium losses occurred during melting.

The observed value of the parabolic rate constant (Kp) for all the alloys utilized in this study was determined by taking the slope of the straight line which resulted from plotting values of $(\frac{\Delta m}{A})^2$ as a function of time. Parabolic rate constants (Kp) and total weight gain data for the cobalt-chromium-silicon-yttrium alloys are given in Table 2. Parabolic rate constants presented were reproducible to within $\pm$ 5%.

The oxidation behavior of Co-5 Cr-0.2 Y with 1, 2.5, 5 and 10 wt % silicon additions is shown in Figure 5. The parabolic oxidation rates of Co-Cr-0.2 Y-Si alloys as a function of increasing silicon content are shown in Figure 6. The kinetic data shows a sharp decrease in the oxidation rate for corresponding increases in silicon content. The Kp of 0.053×10^{-10} gm^2 cm^{-4} sec^{-1} for Co-5 Cr-10 Si-0.2 Y represents a decrease of five orders of magnitude as compared to 3750×10^{-10} gm^2 cm^{-4} sec^{-1} for the Co-5 Cr-1 Si-0.2 Y alloy.

Metallographic examination of the scales formed on these alloys revealed two layers. The alloys containing 1 and 2.5 wt % Si formed scales containing an outer compact layer containing some large pores and an inner finer-porous layer. X-ray diffraction studies of these scales showed the presence of CoO, Co_3O_4, $CoCr_2O_4$ and Co_2SiO_4.

Blank

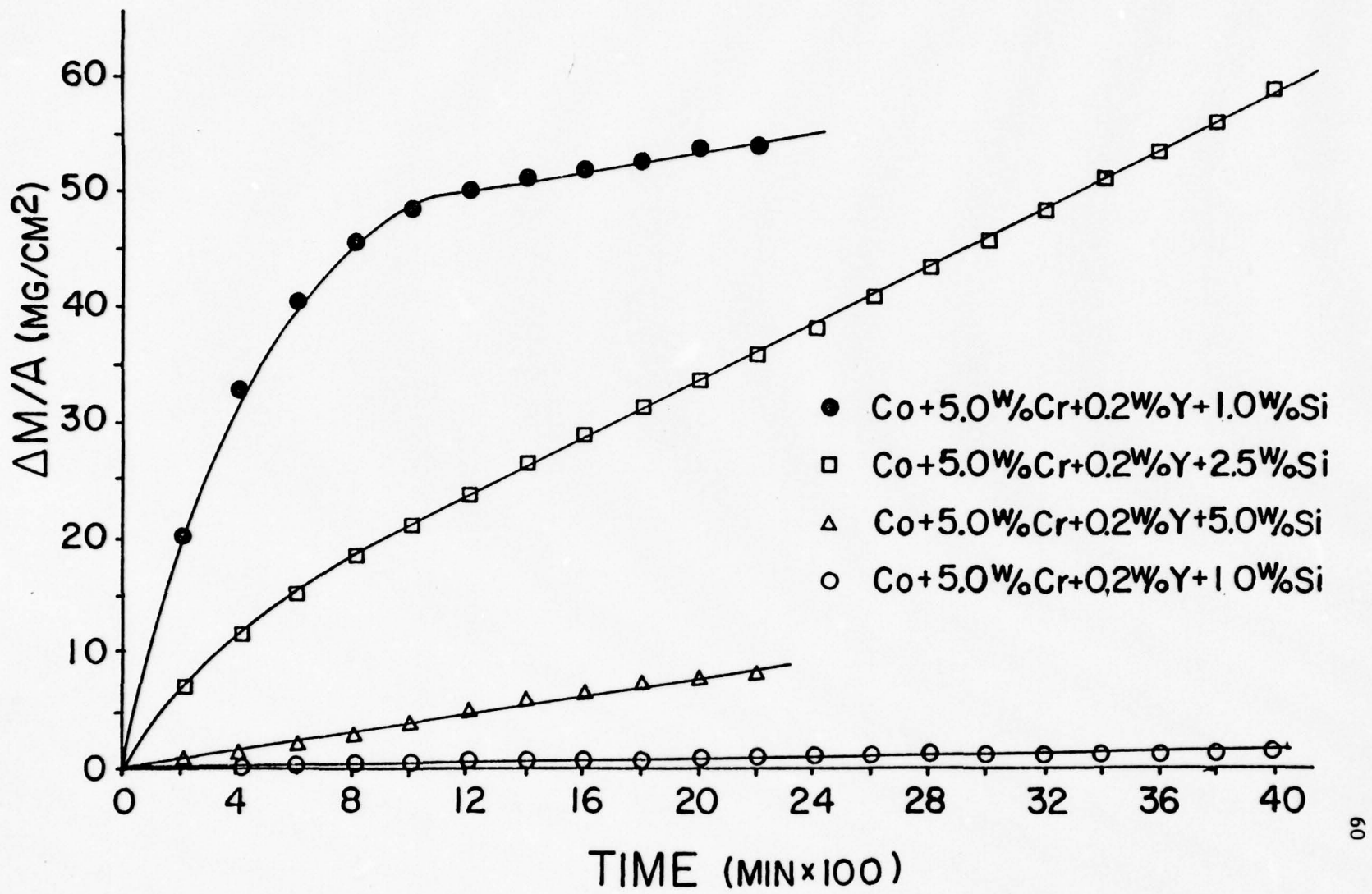
Table 2. Parabolic Rate Constant Data $\Delta m/A$ for the Cobalt-Chromium-Silicon-Yttrium Alloys.

Alloy Composition (Nominal): Cr	Si	Y		Oxidation		Hot Corrosion	
				$K_p \times 10^{10}$ ($gm^2 cm^{-4} sec^{-1}$)	$\frac{\Delta m}{A}$* (mg)	$K_r \times 10^{10}$ ($gm^2 cm^{-4} sec^{-1}$)	$\frac{\Delta m}{A}$*** (gm)
5	1	.2	Bal. Co	3750	53.00**	173000.0	53.33
5	2.5	.2	Bal. Co	300	61.07	65.0	37.76
5	5	.2	Bal. Co	0.092	8.40**	14.0	25.59
5	10	.2	Bal. Co	0.053	1.16	0.036	2.47
10	1	.2	Bal. Co	10	23.28	73.8	41.60
10	2.5	.2	Bal. Co	0.113	1.64	48.3	34.30
10	5	.2	Bal. Co.	0.016	0.63	0.222	8.04
10	10	.2	Bal. Co.	0.064	1.33	0.088	4.02
15	1	.2	Bal. Co	0.591	6.49	3.42	11.73
15	2.5	.2	Bal. Co	0.138	1.50	8.33	23.32
15	5	.2	Bal. Co	0.041	1.39	0.072	6.70
15	10	.2	Bal. Co	0.046	1.19	0.364	4.05
20	1	.2	Bal. Co	0.055	1.21	0.092	6.36
20	2.5	.2	Bal. Co	0.438	3.52	0.010	4.98
20	5	.2	Bal. Co	0.147	2.21	0.046	2.59
20	10	.2	Bal. Co	0.080	1.62	0.004	- .14

*Standard Test Duration 4200 min. **Test Duration 2200 min. ***Standard Test Duration 2900 min.

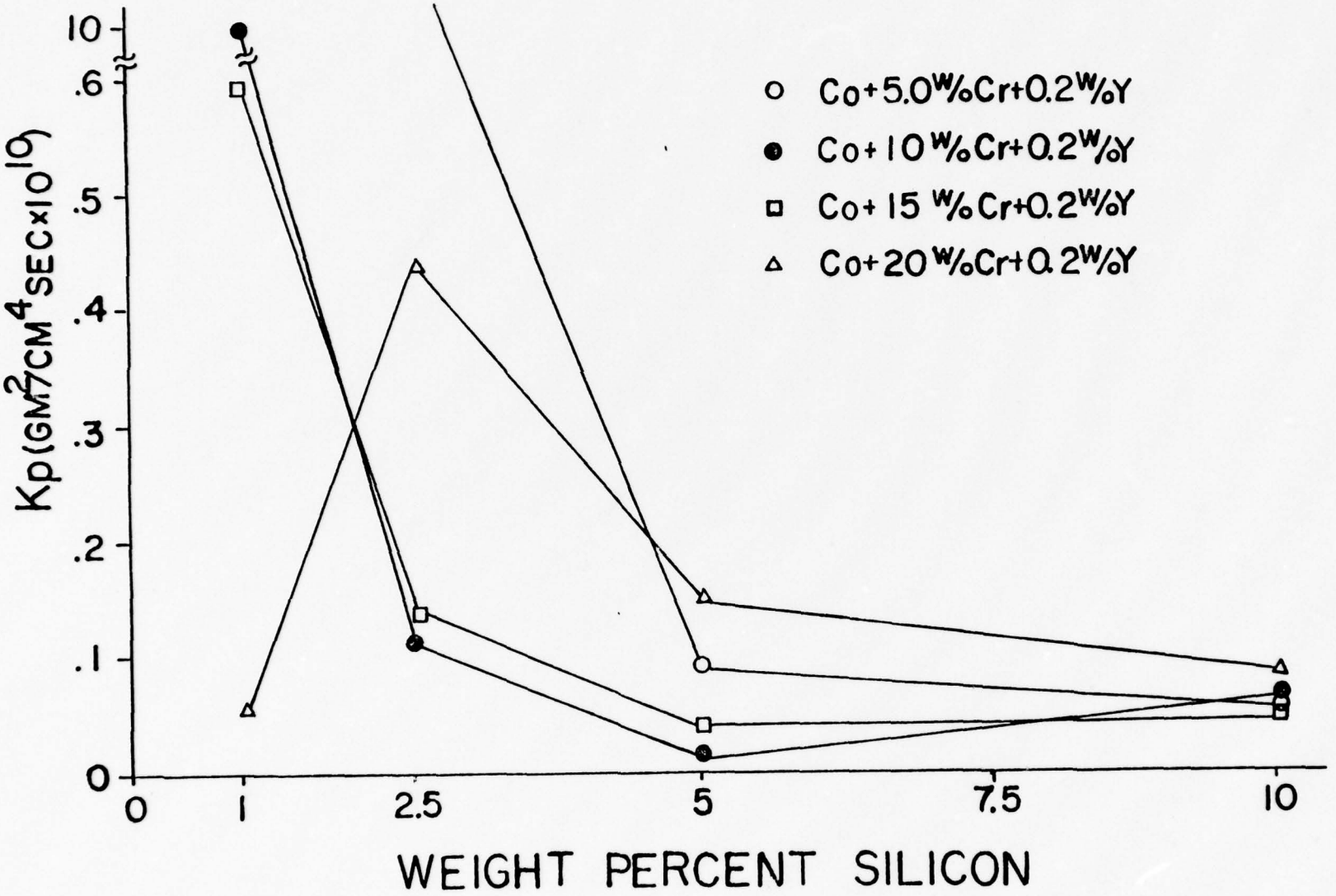
Blank

Figure 5. ($\Delta M/A$) versus time of oxidation of Co- 5Cr- 0.2Y- Si alloys.


ΔM/A (MG/CM2)
60
50
40
30
20
10
0
0
4
8
12
16
20
24
28
32
36
40
TIME (MIN×100)
Co+5.0W%Cr+0.2W%Y+1.0W%Si
Co+5.0W%Cr+0.2W%Y+2.5W%Si
Co+5.0W%Cr+0.2W%Y+5.0W%Si
Co+5.0W%Cr+0.2W%Y+1.0W%Si

Blank

Figure 6. Parabolic oxidation rates of Co- Cr- 0.2Y- Si alloys versus weight percent silicon.


Kp(GM²/CM⁴SEC×10¹⁰)
10
.6
.5
.4
.3
.2
.1
0
0
1
2.5
5
7.5
10
WEIGHT PERCENT SILICON
Co+5.0 W/o Cr+0.2 W/o Y
Co+10 W/o Cr+0.2 W/o Y
Co+15 W/o Cr+0.2 W/o Y
Co+20 W/o Cr+0.2 W/o Y

Microprobe analysis indicated that CoO is the main constituent of the outer layer while the inner layer contains a mixture of CoO, $CoCr_2O_4$ and Co_2SiO_4. The Co_3O_4 probably forms when CoO is cooled. The excess oxygen in the CoO may precipitate in the form of Co_3O_4 (77,78).

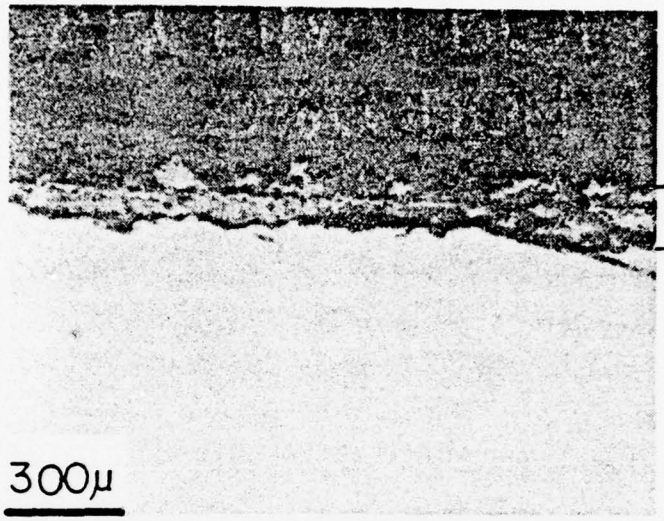
The scale formed on the Co-5 Cr-5 Si-0.2 Y and Co-5 Cr-10 Si-0.2 Y samples was again double layered but the outer layer was much thinner than the 1.0 and 2.5% Si alloys and had a tendency to spall upon cooling. The inner layer was much more compact and exhibited much less porosity, as can be seen in Figure 7. Microprobe analysis showed an increase in silicon at the metal/oxide interface. The chromium concentration was increased and distributed in layers within the inner layer (see Figure 8). X-ray analysis was not attempted on this sample; however, CoO, $CoCr_2O_4$, $CoSiO_4$ and Cr_2O_3 were found in the Co-5 Cr-10 Si-0.2 Y scale. Much higher concentrations of $CoCr_2O_4$ and Co_2SiO_4 were found in the 10% Si scale as compared to the Co-5 Cr-1 Si and 2.5 Si-0.2 Y alloys. At the higher silicon concentrations the formation of a greater amount of Cr_2O_3, and therefore $CoCr_2O_4$, may result from the initial oxidation of silicon. These SiO_2 particles may act in much the same way as dispersions of Y_2O_3, ThO_2 and Al_2O_3 which have been found to promote the formation of Cr_2O_3 in Co-Cr and Ni-Cr alloys (26,27).

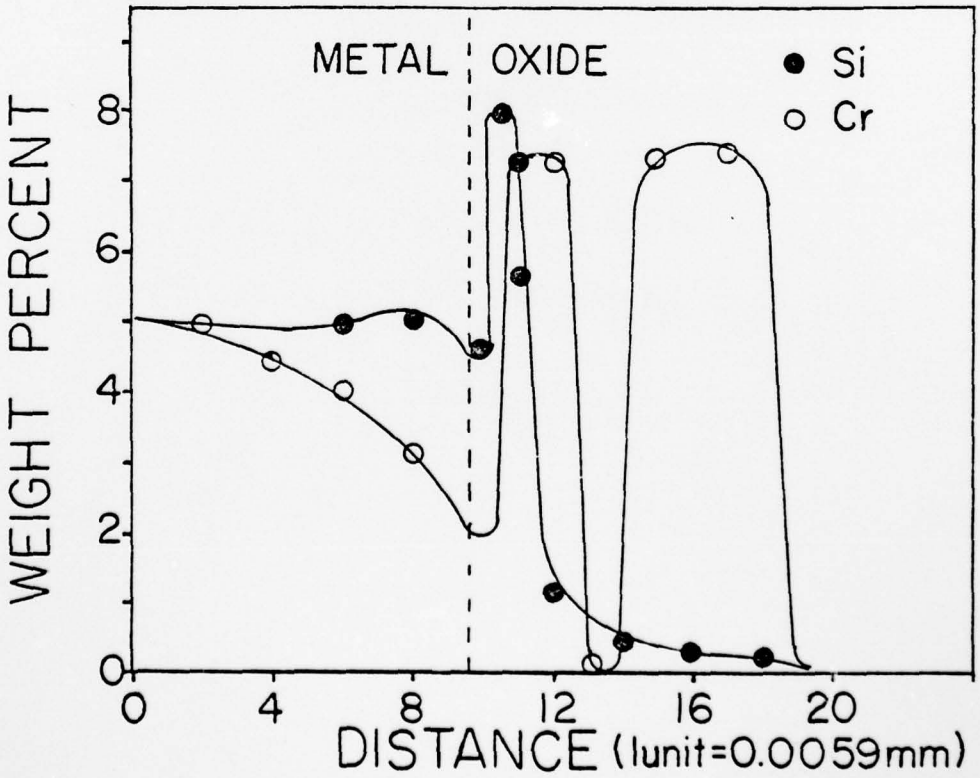
The large decrease in Kp as a function of increasing silicon contents may be explained in terms of concentration of the spinels Co_2SiO_4 and $CoCr_2O_3$. In the 1.0 and 2.5 wt % Si alloys Co_2SiO_4 is the major spinel identified. The reaction rate is controlled by the diffusion of cobalt ions. This is based on the assumption that the

Blank

Figure 7. Photomicrograph of the cross-section of the scale formed on Co- 5Cr- 0.2Y- 5Si alloy after oxidation.

Figure 8. Microprobe profile of Co- 5Cr- 0.2Y- 5Si alloy after oxidation.


CoO
$Co_2Cr_2O_4 + Co_2SiO_4$
ALLOY
300μ


METAL
OXIDE
Si
Cr
WEIGHT PERCENT
0
2
4
6
8
0
4
8
12
16
20
DISTANCE (1unit=0.0059mm)

diffusion of Co in CoO is faster than in Co_2SiO_4, and much faster than in SiO_2. This is also the case in the Co-Cr alloys. It has been postulated that Co diffuses more slowly in Cr_2O_3 and $CoCr_2O_4$ than in CoO (4).

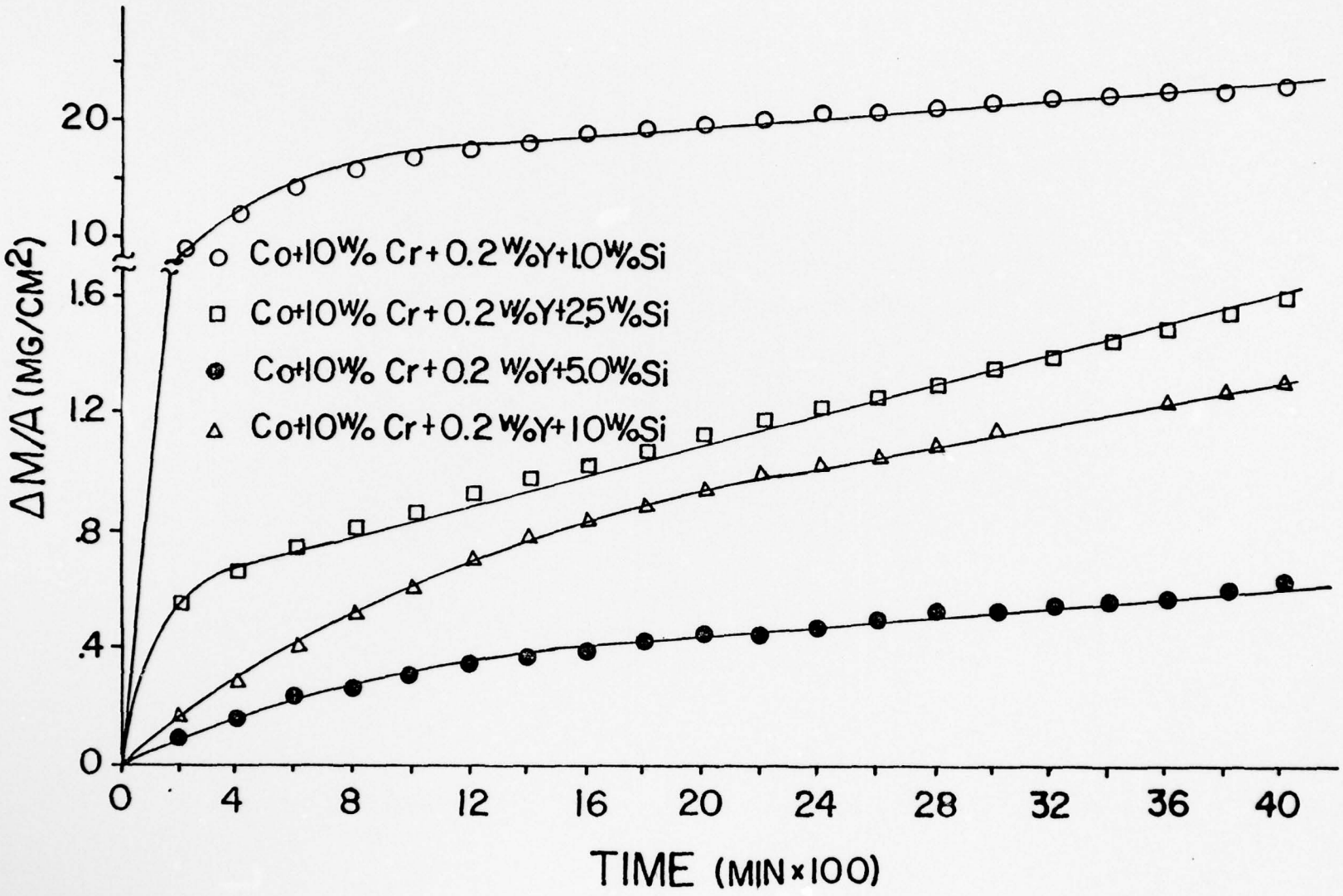
The initial oxidation, especially of the alloys containing the higher silicon concentrations, probably involves the simultaneous formation of CoO, Cr_2O_3, and SiO_2. After a continuous film was formed, the oxidation became controlled by the diffusion of cobalt ions through the CoO phase. The CoO phase continued to grow. A chemical potential gradient then existed through the oxide scale, and at some relative thickness, conditions within the oxide existed and the decomposition of CoO occurred at the metal/oxide interface. This decomposition of CoO will produce oxygen ions for the internal oxidation of Cr and Si. Depending upon the respective chemical potentials of Cr and Si, either one or both may oxidize. The cobalt ion formed will then diffuse outward through the CoO layer. This decomposition of CoO and the subsequent diffusion of Co ion will result in vacancy formation. The cobalt ions also continue to diffuse away from the metal/oxide interface but their diffusion path is blocked by the SiO_2 and Cr_2O_3 particles, which can also serve as sites for cobalt vacancy condensation. This will create porosity. The available area for the solid-state diffusion of cobalt is continuously reduced by the formation of SiO_2 and Cr_2O_3 particles, and cavities formed by vacancy condensation. The SiO_2 and Cr_2O_3 particles surrounded by CoO eventually react to form the spinels $CoSi_2O_4$ and $CoCr_2O_4$. No evidence of an SiO_2 phase was found in these alloys.

The oxidation of the Co-10 Cr-0.2 Y-Si alloys again showed the same trends as in the Co-5 Cr-0.2 Y-Si alloys. There was an overall decrease in the parabolic rate constants as a function of increasing silicon contents. This is represented graphically in Figure 6. Parabolic rate constants are listed in Table 2. The oxidation behavior of the Co-10 Cr-0.2 Y-Si alloys is shown in Figure 9. An interesting anomaly exists in that Kp and the $\frac{\Delta m}{A}$ are greater for the 10% Si alloy than the 5% Si alloy. This will be discussed in greater detail later, however it should be noted that the oxidation behavior was again parabolic. There is a 2.5 order of magnitude decrease in the oxidation rate of Co-10 Cr-0.2 Y-1 Si (10×10^{-10} gm^2 cm^{-4} sec^{-1}) as compared to that of the Co-10 Cr-0.2 Y-10 Si (0.064×10^{-10} gm^2 cm^{-4} sec^{-1}) alloy.

Metallographic examination of the scales formed on this set of alloys again showed a double layered structure. An outer porous layer was formed along with a dense, more compact inner layer (see Figure 10). The outer layer showed a tendency to spall upon cooling. This was especially evident in the 5 and 10 wt % silicon containing alloys. X-ray analysis of the Co-10 Cr-0.2 Y-1 Si alloy indicated the formation of CoO, $CoCr_2O_4$ and Co_2SiO_4. The initial decrease in the oxidation rate as a function of silicon contents is probably due to the effect of spinel particles blocking the diffusion of cobalt ions. At higher concentrations of silicon (5% and greater), Cr_2O_3 was formed which apparently did not react with CoO since no $CoCr_2O_4$ was identified. Microprobe profiles of the Co-10 Cr-0.2 Y-10 Si alloy scale showed significant increase in the silicon concentration at the alloy/oxide interface as shown in Figure 11. The amount of chromium present in the scales

Blank

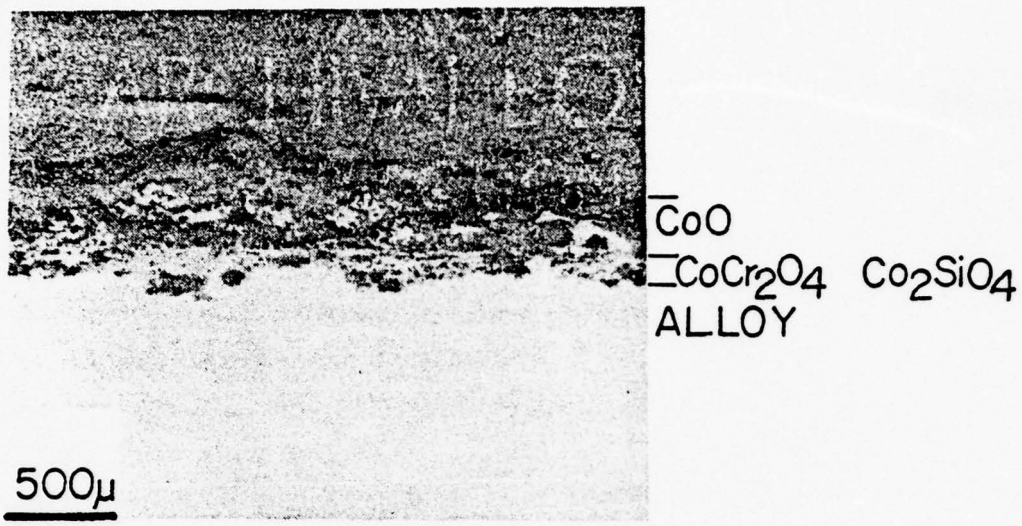
Figure 9. ($\Delta M/A$) versus time of oxidation of Co- 10Cr- 0.2Y- Si alloys.

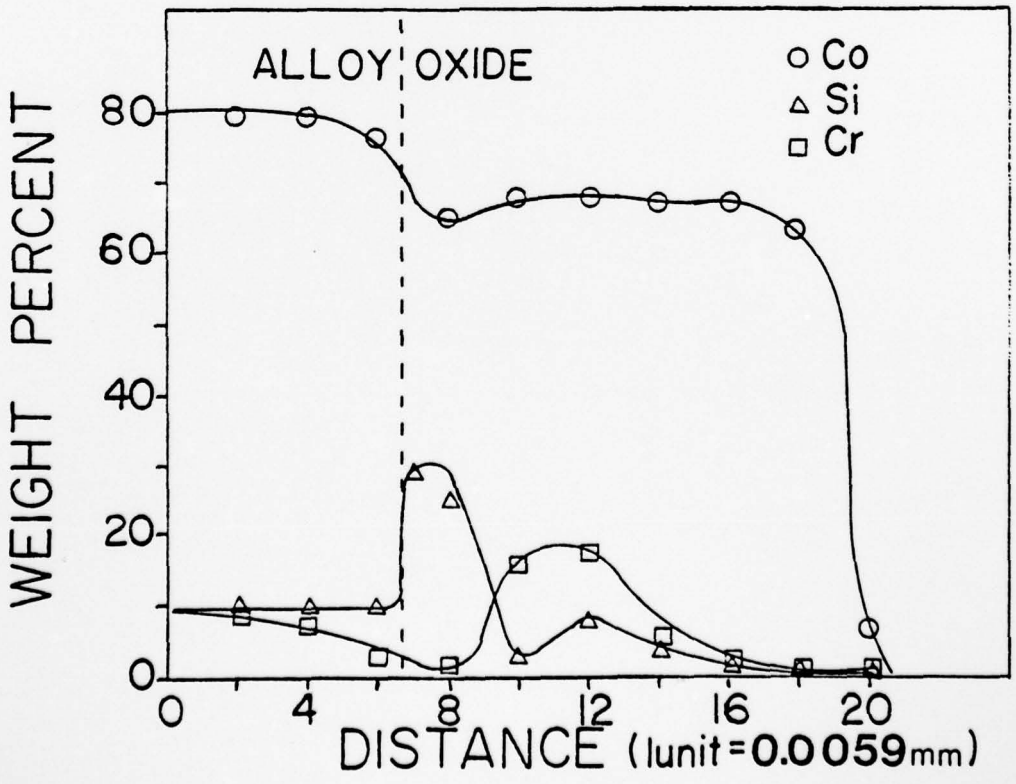

ΔM/A (MG/CM²)
20
10
1.6
1.2
.8
.4
0
0
4
8
12
16
20
24
28
32
36
40
TIME (MIN×100)
Co+10W% Cr+0.2W%Y+1.0W%Si
Co+10W% Cr+0.2W%Y+2.5W%Si
Co+10W% Cr+0.2W%Y+5.0W%Si
Co+10W% Cr+0.2W%Y+10W%Si

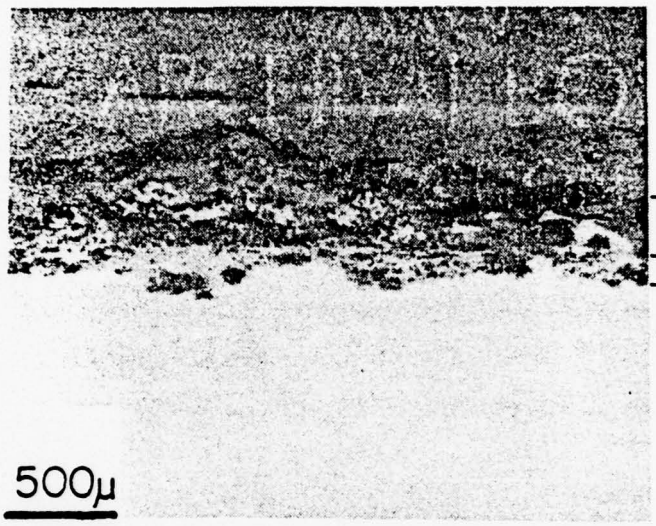
Blank

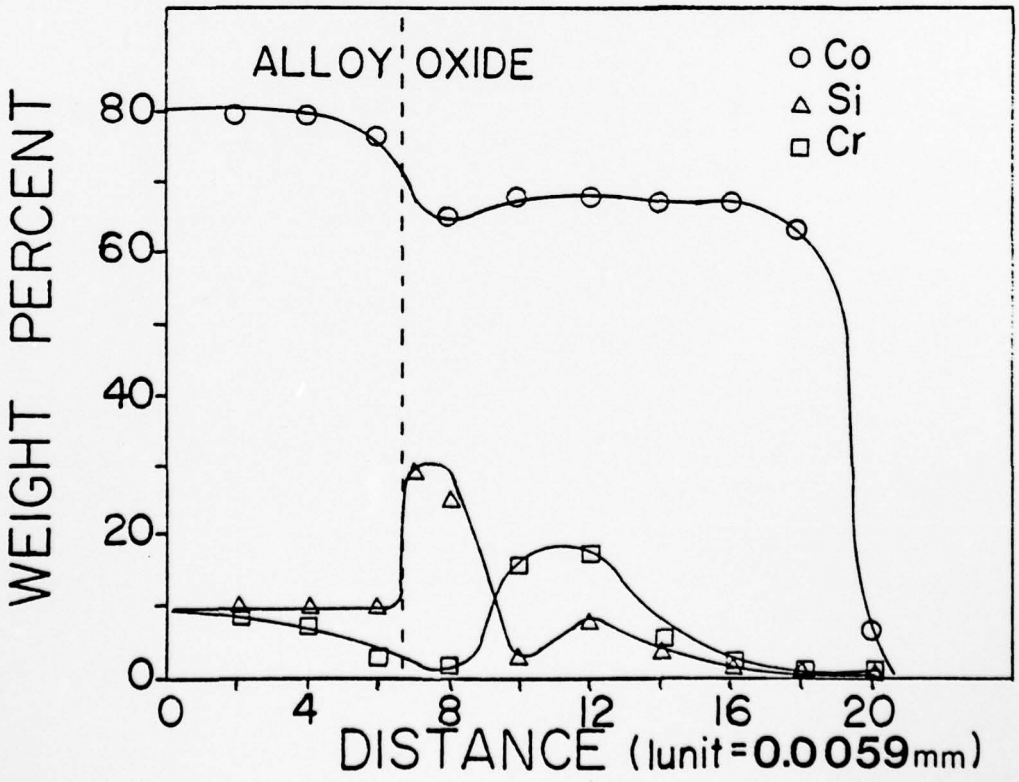
Figure 10. Photomicrograph of the cross-section of the scale formed on Co- 10Cr- 0.2Y- 2.5Si alloy after oxidation.

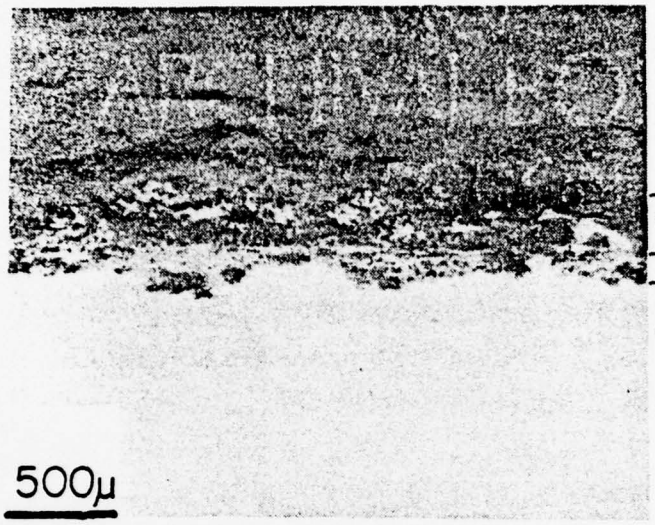
Figure 11. Microprobe profile of Co- 10Cr- 0.2Y- 10Si alloy after oxidation.

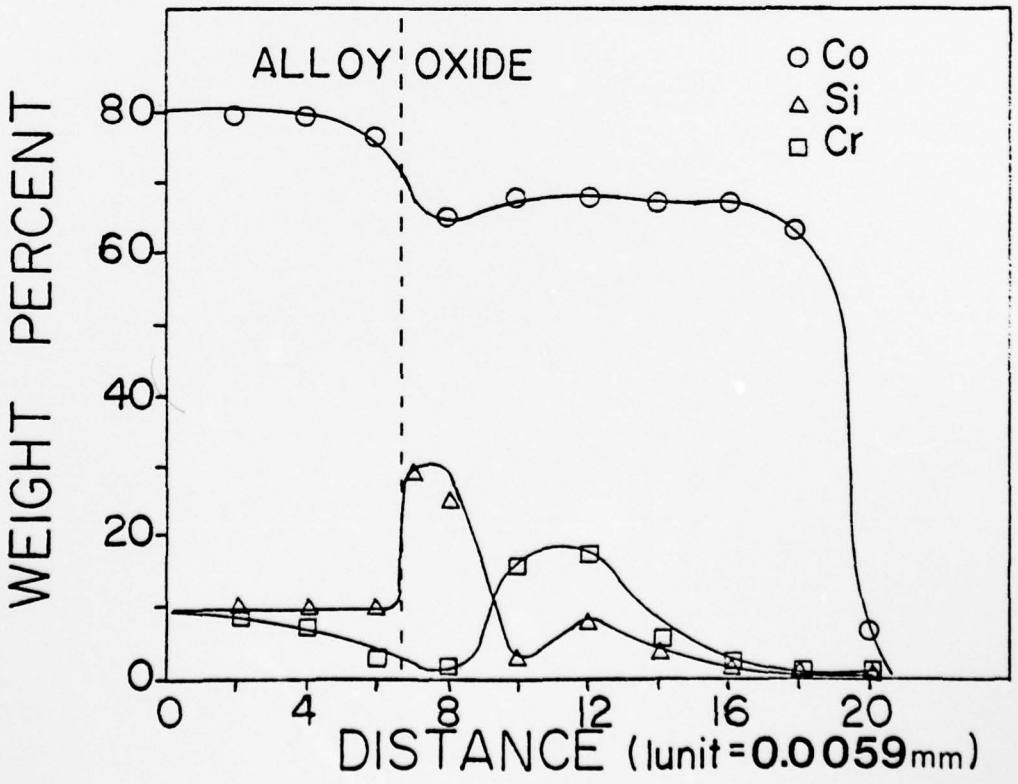

CoO
CoCr2O4
Co2SiO4
ALLOY
500μ


ALLOY
OXIDE
Co
Si
Cr
WEIGHT PERCENT
0
20
40
60
80
0
4
8
12
16
20
DISTANCE (1unit=0.0059mm)


CoO
$CoCr_2O_4$ Co_2SiO_4
ALLOY
500μ


ALLOY
OXIDE
Co
Si
Cr
WEIGHT PERCENT
0
20
40
60
80
0
4
8
12
16
20
DISTANCE (1unit = 0.0059mm)


CoO
$CoCr_2O_4$
Co_2SiO_4
ALLOY
500μ


ALLOY
OXIDE
Co
Si
Cr
WEIGHT PERCENT
0
20
40
60
80
0
4
8
12
16
20
DISTANCE (1unit = 0.0059mm)

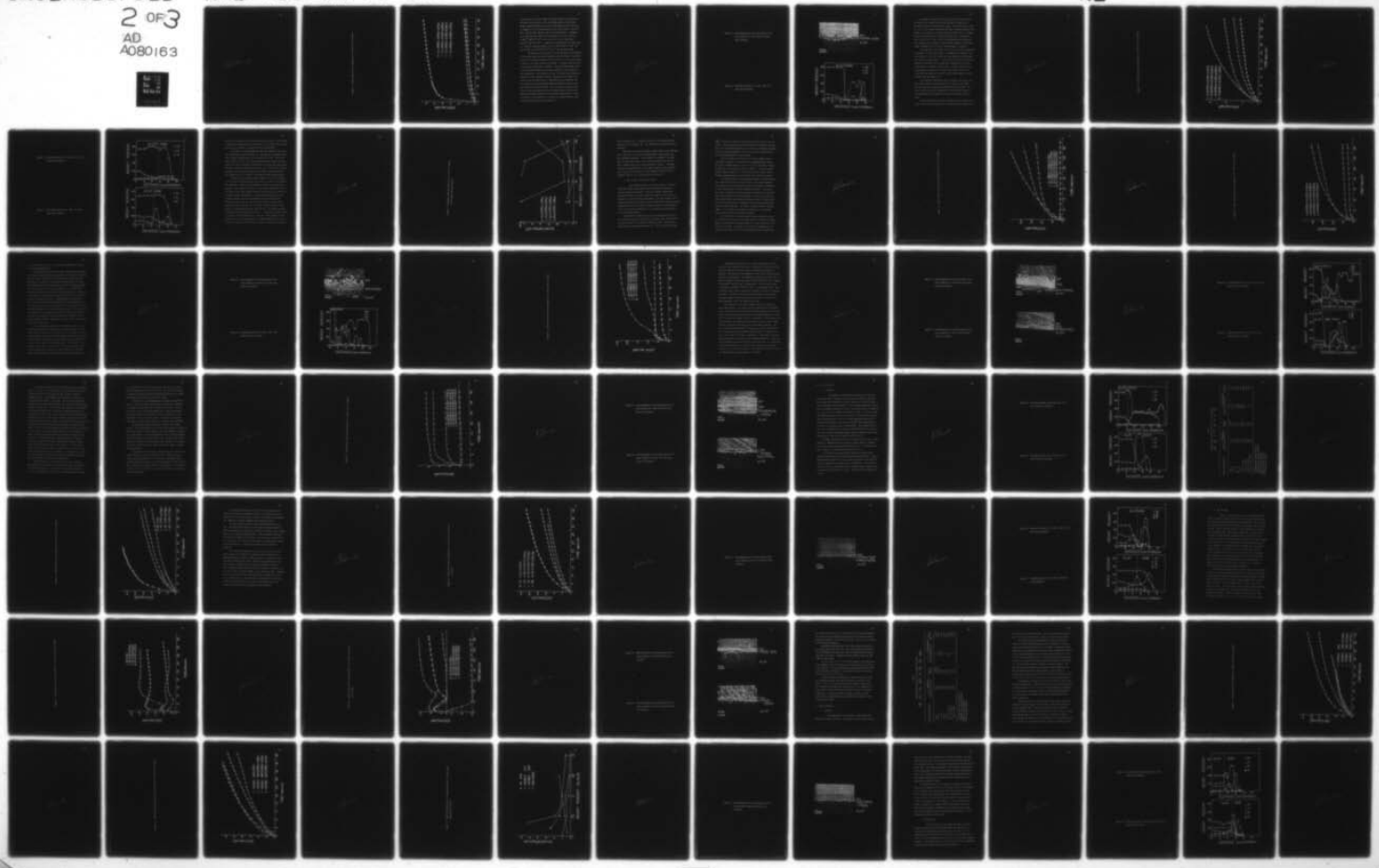
formed on the 5 and 10% Si alloys was significantly reduced relative to the amount formed on the 1 and 2.5% Si alloys.

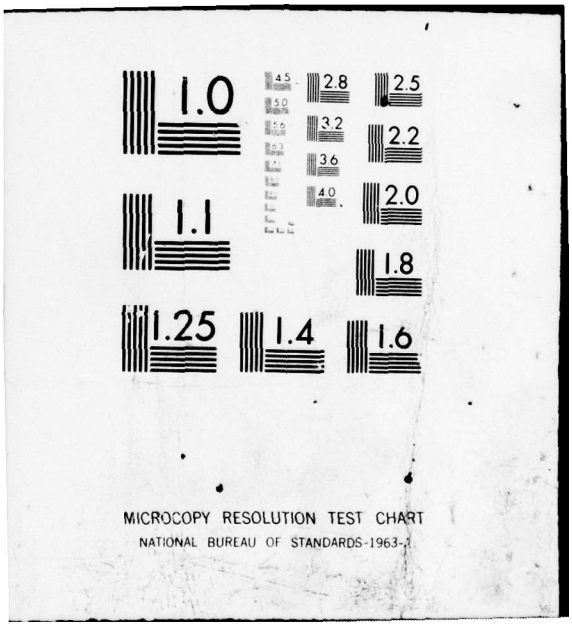
In the previous discussion of the oxidation kinetics of the Co-10 Cr-0.2 Y-Si alloy set, it was noted that the oxidation rate of the 5% Si alloy was less than that of the 10% Si containing alloy. In view of the elemental distribution results on the Co-10 Cr-0.2 Y-10 Si, and the scale composition of the Co-10 Cr-0.2 Y-5 Si alloy, it would appear that the scales formed on both the 5% Si and the 10% Si alloys are similar. Hock (4) investigated a similar set of Co-10 Cr-Si under the exact same conditions utilized in this study. Hock's results showed a constant decrease in the oxidation rate as a function of increased silicon content up to and including the 10% Si alloy. The only difference between this investigation and the study conducted by Hock (4) is Hock did not attempt to add yttrium to the Co-Cr-Si alloy he investigated. Doping theory predicts that ionic transport would be increased in CoO scales if Y_2O_3 were present in CoO in low concentrations (ppm). It is therefore possible that yttrium present in very minor concentrations could be responsible for the increased oxidation rate of the Co-10 Cr-0.2 Y-10 Si alloy as compared to that of the Co-10 Cr-0.2 Y-5 Si alloy. However, chemical analysis of selected samples failed to find any concentrations of yttrium above 0.01 wt %.

The oxidation of Co-15 Cr-0.2 Y-Si alloys, varying in silicon concentration from 1 to 10% silicon, was again parabolic (see Figure 12) All of the reaction rates (Table 12) in this alloy group were of the order of 10^{-11} gm^2 cm^{-4} sec^{-1}. The total weight gain after 4200 minutes

AD-A080 163 PENNSYLVANIA STATE UNIV UNIVERSITY PARK APPLIED RESE--ETC F/G 11/6
HOT CORROSION AND OXIDATION STUDIES OF COBALT BASED SUPERALLOYS--ETC(U)
OCT 79 G A DRIES N00024-79-C-6043
UNCLASSIFIED ARL/PSU/TM/79-177 NL

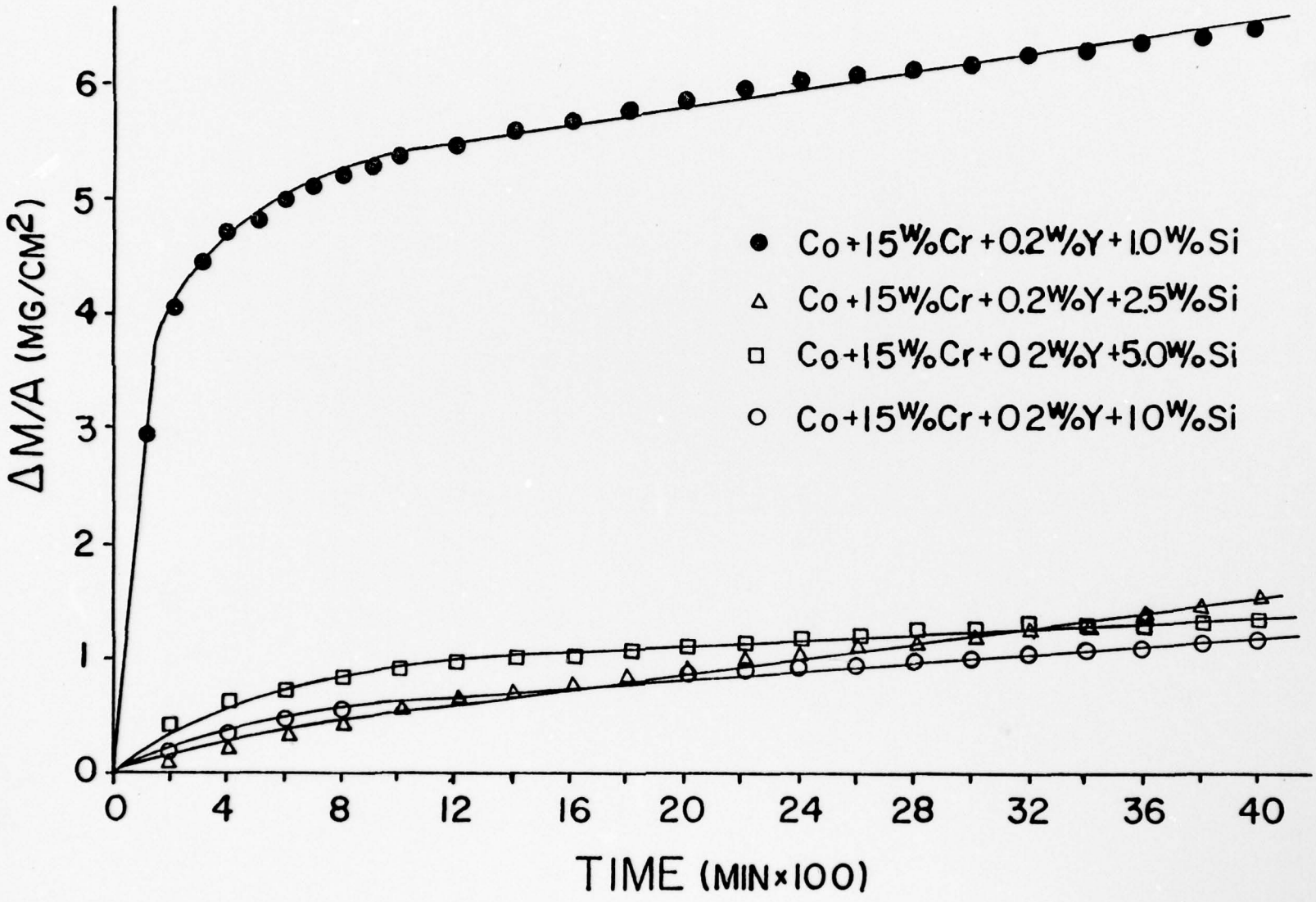
2 OF 3
AD
A080163




1.0
1.1
1.25
1.4
1.6
1.8
2.0
2.2
2.5
2.8
3.2
3.6
4.0
4.5
5.0
MICROCOPY RESOLUTION TEST CHART
NATIONAL BUREAU OF STANDARDS-1963-A

Blank

Figure 12. ($\Delta M/A$) versus time of oxidation of Co- 15Cr- 0.2Y- Si alloys.


ΔM/A (MG/CM²)
0
1
2
3
4
5
6
0
4
8
12
16
20
24
28
32
36
40
TIME (MIN×100)
Co+15W/oCr+0.2W/oY+1.0W/oSi
Co+15W/oCr+0.2W/oY+2.5W/oSi
Co+15W/oCr+0.2W/oY+5.0W/oSi
Co+15W/oCr+0.2W/oY+10W/oSi

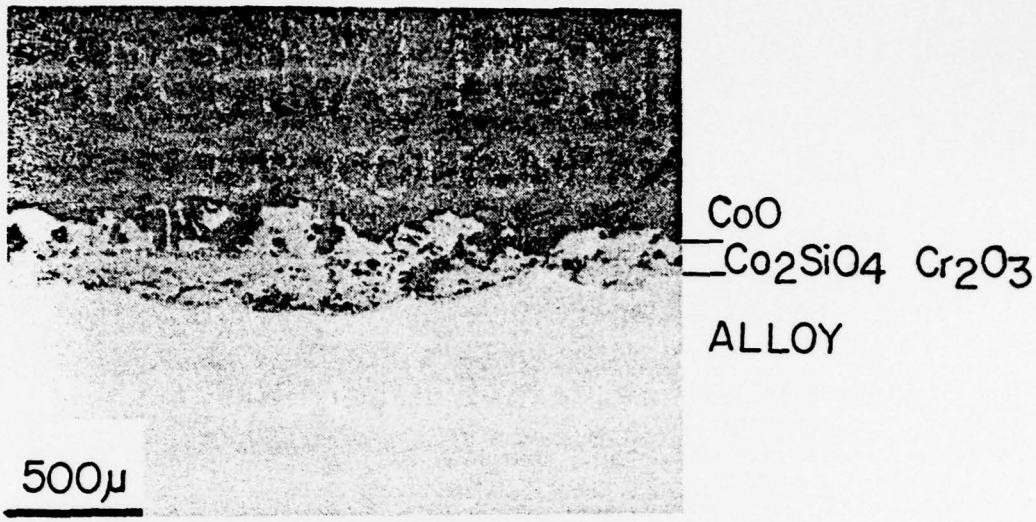
of the alloys in this set showed a constant decrease as a function of increased silicon content. The total weight gain by these alloys showed a sharp decrease from the 6.49 mg increase for the 1% Si alloy as compared to the 1.50 mg increase for the 2.5% Si alloy. The parabolic reaction rate constants were not so well-behaved. A decrease in the reaction rate occurs with the addition of 2.5 wt % Si (K_p = 1.38×10^{-11} gm^2 cm^{-4} sec^{-1}) over that for the 1 wt % alloy (K_p = 5.91×10^{-11} gm^2 cm^{-4} sec^{-1}). Additions of silicon from 5 to 10% Si lead to a slightly increased oxidation rate, 4.1×10^{-11} gm^2 cm^{-4} sec^{-1} for the 5% alloy, and 4.6×10^{-11} gm^2 cm^{-4} sec^{-1} for the 10% Si alloy.

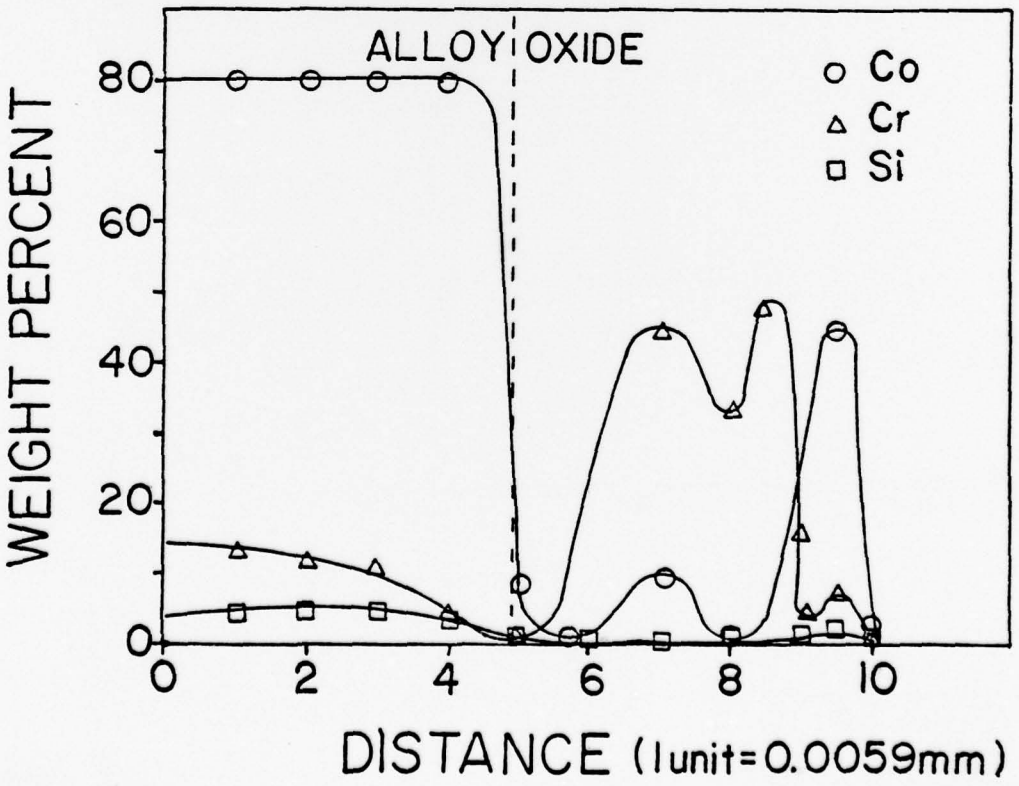
The oxidation of this group of alloys resulted in the formation of thin oxide layers with the exception of the 1% Si alloy. The microstructure of the scale formed on the Co-15 Cr-0.2 Y-1 Si alloy as shown in Figure 13 is double layered in structure. A porous outer layer and a more compact inner layer is evident. The outer scales formed on the 5 and 10% silicon samples had partially spalled off upon cooling to room temperature. X-ray analysis of the 2.5% silicon alloy showed the formation of CoO, Co_2SiO_4 and Cr_2O_3. $CoCr_2O_4$ was also found in the scales on the 10% silicon alloy. Microprobe results indicated that the chromium and silicon concentrations were high but diffuse in the scale formed on thel.0% Si alloy. The 5% Si alloy scale had a much lower silicon concentration, and the chromium content of the scale appeared much more concentrated at the alloy-oxide interface. There is evidence of the formation of a partial or possibly complete layer of Cr_2O_3 within the scale (see Figure 14).

Blank

Figure 13. Photomicrograph of the cross-section of the scale formed on Co- 15Cr- 0.2Y- 1Si alloy after oxidation.

Figure 14. Microprobe profile of Co- 15Cr- 0.2Y- 5Si alloy after oxidation.


CoO
Co2SiO4 Cr2O3
ALLOY
500μ


ALLOY
OXIDE
Co
Cr
Si
WEIGHT PERCENT
0
20
40
60
80
0
2
4
6
8
10
DISTANCE (1unit=0.0059mm)

The greater concentrations of Cr_2O_3 present in the scales of the high silicon containing alloys may indicate a change in the diffusion controlling species in the oxides. The lower silicon alloys (1, 2.5 wt % Si) formed scales which had their oxidation behavior attributable to the presence of spinels within the duplex scale. The high silicon alloys may exhibit a higher oxidation rate, as compared to that of the 2.5 wt % alloy, due to the suppressed silicon oxidation. This resulted from an apparent rapid chromium oxidation which possibly formed a complete layer during the initial stages of oxidation.

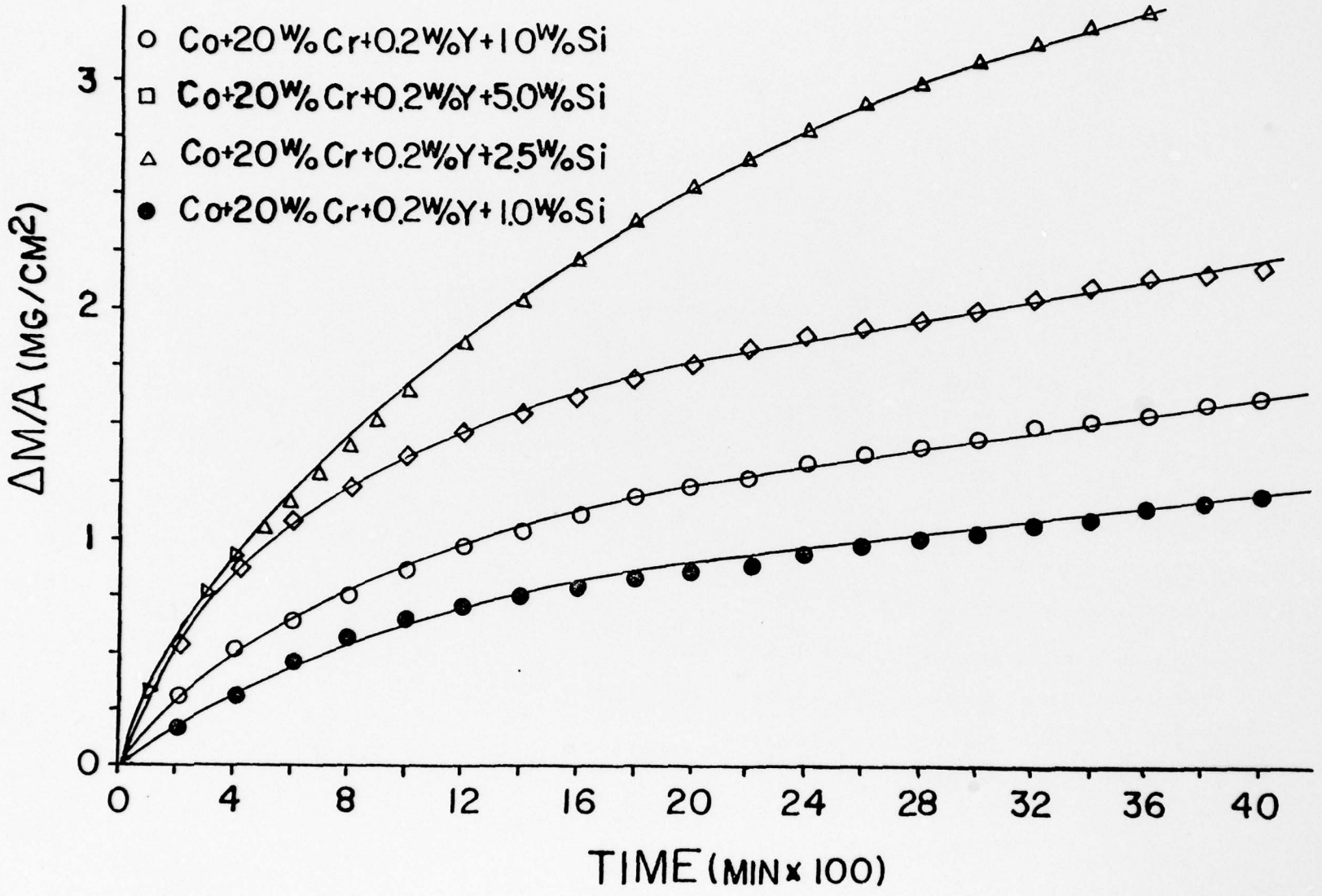
The oxidation of the Co-20 Cr-0.2 Y-Si set of alloys resulted in the formation of thin oxide scales. The oxidation was parabolic for all the alloys. The 1% Si and 10% Si alloys showed the lowest oxidation rates as noted in Table 2. All the alloys in this set showed low oxidation rates and low total weight gain attributable to the high concentration of chromium in these alloys. Overall, higher silicon concentrations in the alloys did lower the oxidation rate as predicted with the exception of the 1% Si alloy which showed the lowest oxidation rate (see Figure 15).

X-ray analysis showed CoO, Co_2SiO_4, $CoCr_2O_4$, and Cr_2O_3 as the major oxides formed on the Co-20 Cr-0.2 Y-Si alloys. The oxides were very thin and a duplex scale morphology was not evident. The higher silicon alloys were susceptible to spalling upon cooling to room temperature, which revealed the metallic substrate below the oxide.

Microprobe profiles presented in Figures 16 and 17 show an increase in the silicon concentration at the alloy/oxide interface as s

Blank

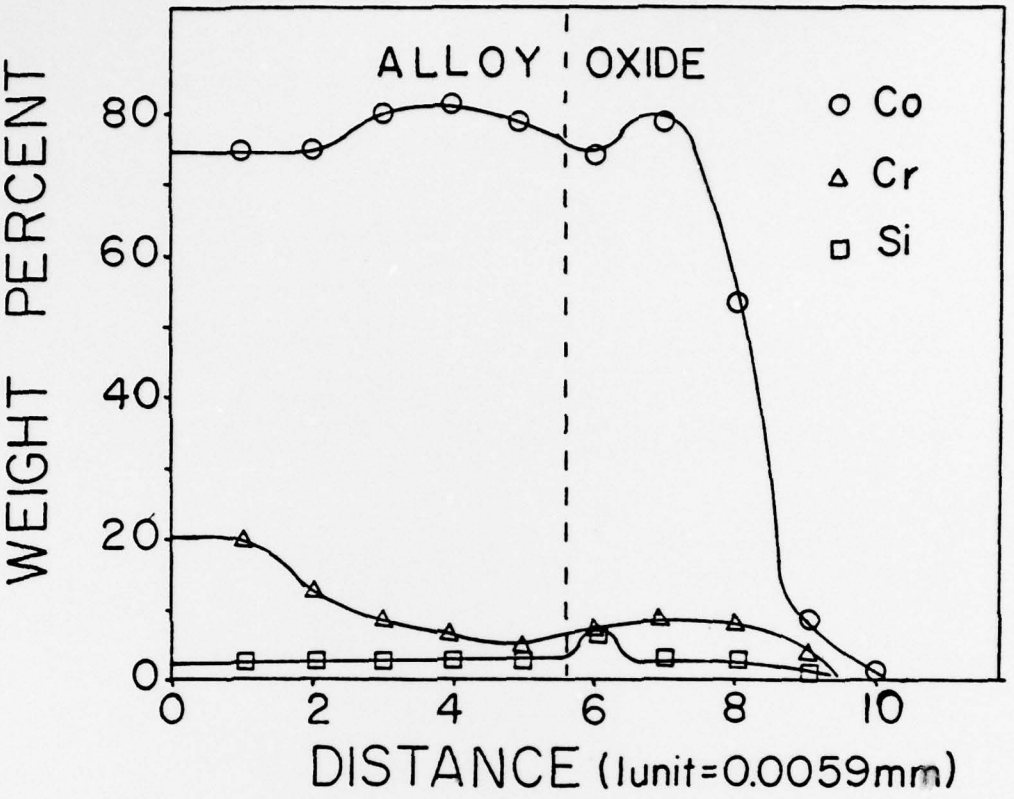
Figure 15. ($\Delta M/A$) versus time of oxidation of Co- 20Cr- 0.2Y- Si alloys.

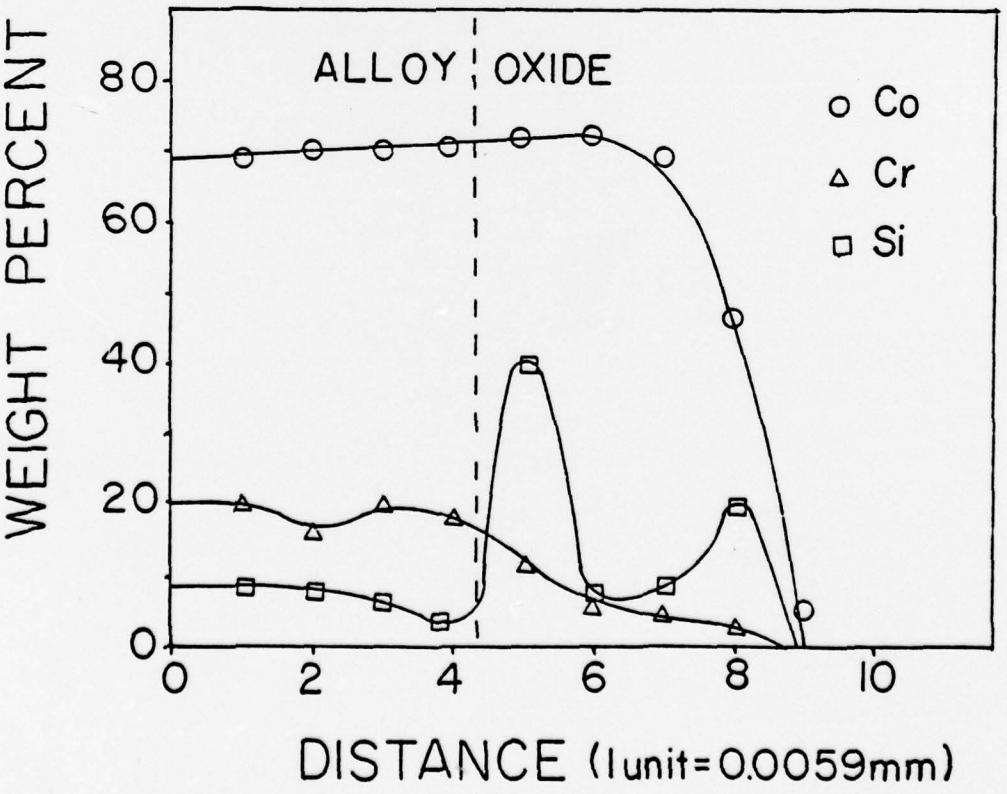

Co+20W%Cr+0.2W%Y+1.0W%Si
Co+20W%Cr+0.2W%Y+5.0W%Si
Co+20W%Cr+0.2W%Y+2.5W%Si
Co+20W%Cr+0.2W%Y+1.0W%Si
ΔM/A (MG/CM2)
0
1
2
3
0
4
8
12
16
20
24
28
32
36
40
TIME (MIN x 100)

Blank

Figure 16. Microprobe profile of Co- 20Cr- 0.2Y- 2.5Si alloy after oxidation.

Figure 17. Microprobe profile of Co- 20Cr- 0.2Y- 10Si alloy after oxidation.


ALLOY
OXIDE
Co
Cr
Si
WEIGHT PERCENT
0
20
40
60
80
0
2
4
6
8
10
DISTANCE (1unit=0.0059mm)


ALLOY
OXIDE
Co
Cr
Si
WEIGHT PERCENT
0
20
40
60
80
0
2
4
6
8
10
DISTANCE (1unit=0.0059mm)

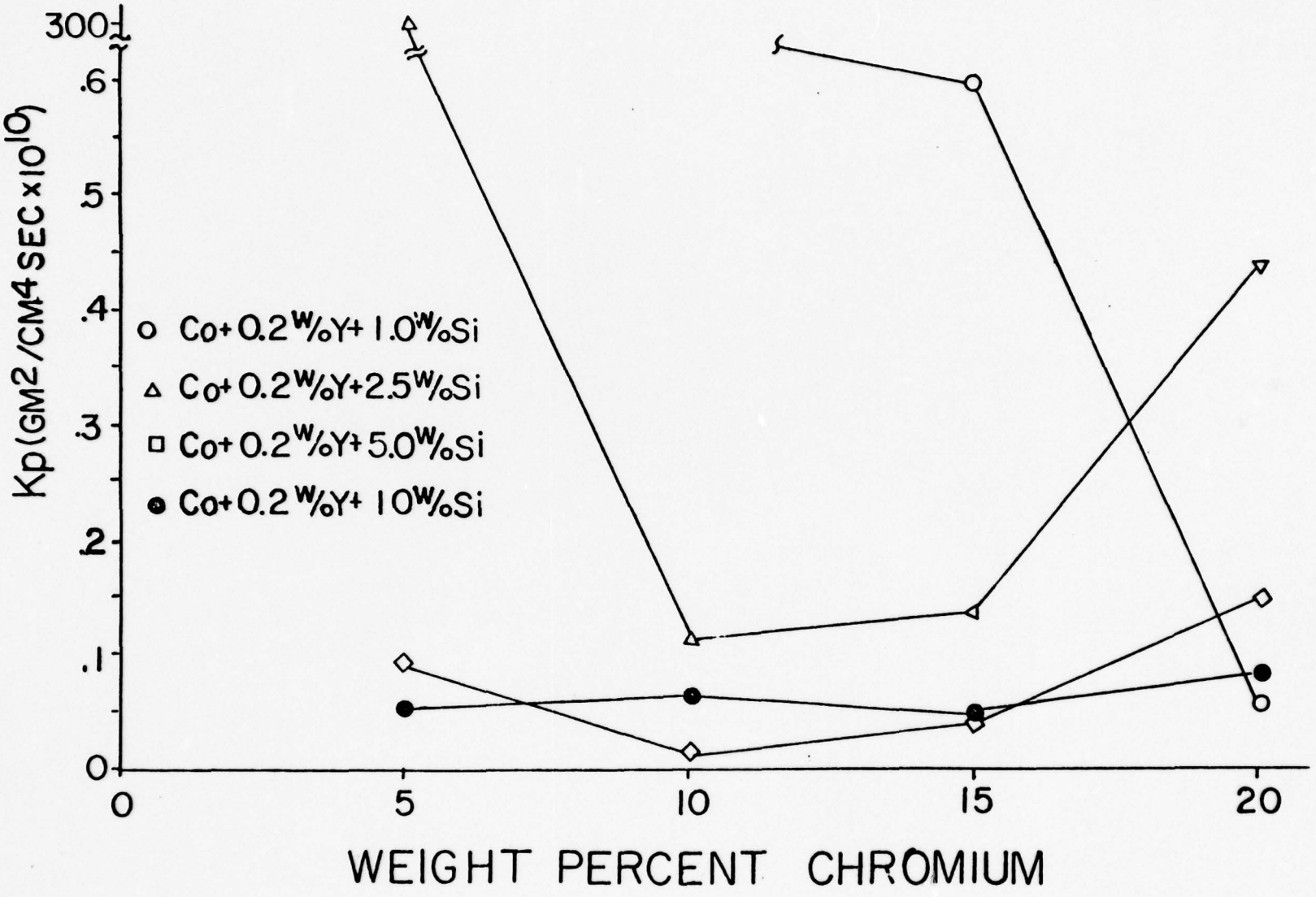
function of increased silicon concentrations in the alloy. This increase is apparently responsible for the reduction in the oxidation rate of this alloy set as a function of increased silicon concentration.

The effects of chromium additions upon the oxidation rates of Co-Si-Y alloys may be viewed in Figure 18. The addition of chromium drastically reduces the oxidation rate, from 3750 $gm^2\ cm^{-4}\ sec^{-1}$ for the Co-20 Cr-1 Si-0.2 Y alloy. X-ray and microprobe analysis showed that this reduction is due to increased concentrations of $CoCr_2O_4$ and Cr_2O_3 within the oxide. The same reduction is noted for the 2.5% Si alloys, with the exception that the higher chromium alloys showed a slight increase in the oxidation rate as a function of increased chromium concentrations.

The 5% Si alloys showed a similar behavior to the 2.5 Si alloys. As the chromium concentration was raised from 5 to 10% Cr, the oxidation rate decreased. Higher chromium additions increase the oxidation rate slightly. This behavior is contrary to the results obtained by Hock (4), for similar alloys which showed a steady decrease in Kp as a function of increased silicon concentration. As was noted previously, the major difference between the alloys investigated by Hock and the alloys produced for this study, is that yttrium was added to promote scale adhesion. Yttrium, however, was not found by chemical analysis to be present in concentrations greater than 0.01 wt %. No attempt was made to determine concentrations below 0.01 wt %. Doping theory would predict an increase in ionic transport as a result of yttrium impurities, and therefore low yttrium concentrations, if somewhat higher in the Co-5 Si-15 Cr-0.2 Y and the Co-5 Si-20 Cr-0.2 Y alloys, would cause an increase

Blank

Figure 18. Parabolic oxidation rates of Co- Cr- 0.2Y- Si alloys versus weight percent chromium.


300
.6
.5
.4
.3
.2
.1
0
Kp (GM2/CM4 SEC x 10^10)
o Co+0.2 W%Y+1.0 W%Si
△ Co+0.2 W%Y+2.5 W%Si
□ Co+0.2 W%Y+5.0 W%Si
● Co+0.2 W%Y+10 W%Si
0
5
10
15
20
WEIGHT PERCENT CHROMIUM

in the oxidation rate. It should be noted that the oxidation rates observed are all extremely low. The samples show very good oxidation resistance.

The effect of increased chromium concentrations on the oxidation rate of the 10 wt % Si alloys is insignificant. These alloys show good oxidation resistance. Ionic transport is limited by the formation of a fine distribution of SiO_2 particles which may or may not form a complete SiO_2 scale at the alloy/scale interface. Increased chromium concentrations show a very slight increase in the oxidation rate of the Co-15 Cr-10 Si-0.2 Y from 0.046×10^{-11} gm^2 cm^{-4} sec^{-1} to 0.08×10^{-11} gm^2 cm^{-4} sec^{-1} for the Co-20 Cr-10 Si-0.2 Y.

2. Hot Corrosion of Co-Cr-Y-Si Alloys

The oxidation behavior of an alloy under hot corrosive conditions differs significantly from the behaviors noted under a strictly oxidizing environment. Mild hot corrosive conditions as produced with the salt coating method of testing are still severe as compared to a purely oxidizing environment. For these reasons, and to further substantiate the effect of silicon additions to reduce an alloy's susceptibility to the accelerated oxidation attack, it was decided to study all the alloys investigated in an oxidizing environment under a hot corrosion environment.

Concerning the oxidation rate and total weight gain per unit area values, it should be noted that the oxidation rate values listed for hot corrosion are not parabolic oxidation rates. Hot corrosive attack does not follow parabolic behavior. The rate constants listed

$(\frac{\Delta m}{A})^2$ vs time plots from data taken during the final hours of hot corrosion. The rate constants have been included for comparison purposes only. The total weight gained per unit area is a much better evaluation of the hot corrosion behavior, and will be the main consideration in the following discussion of hot corrosion.

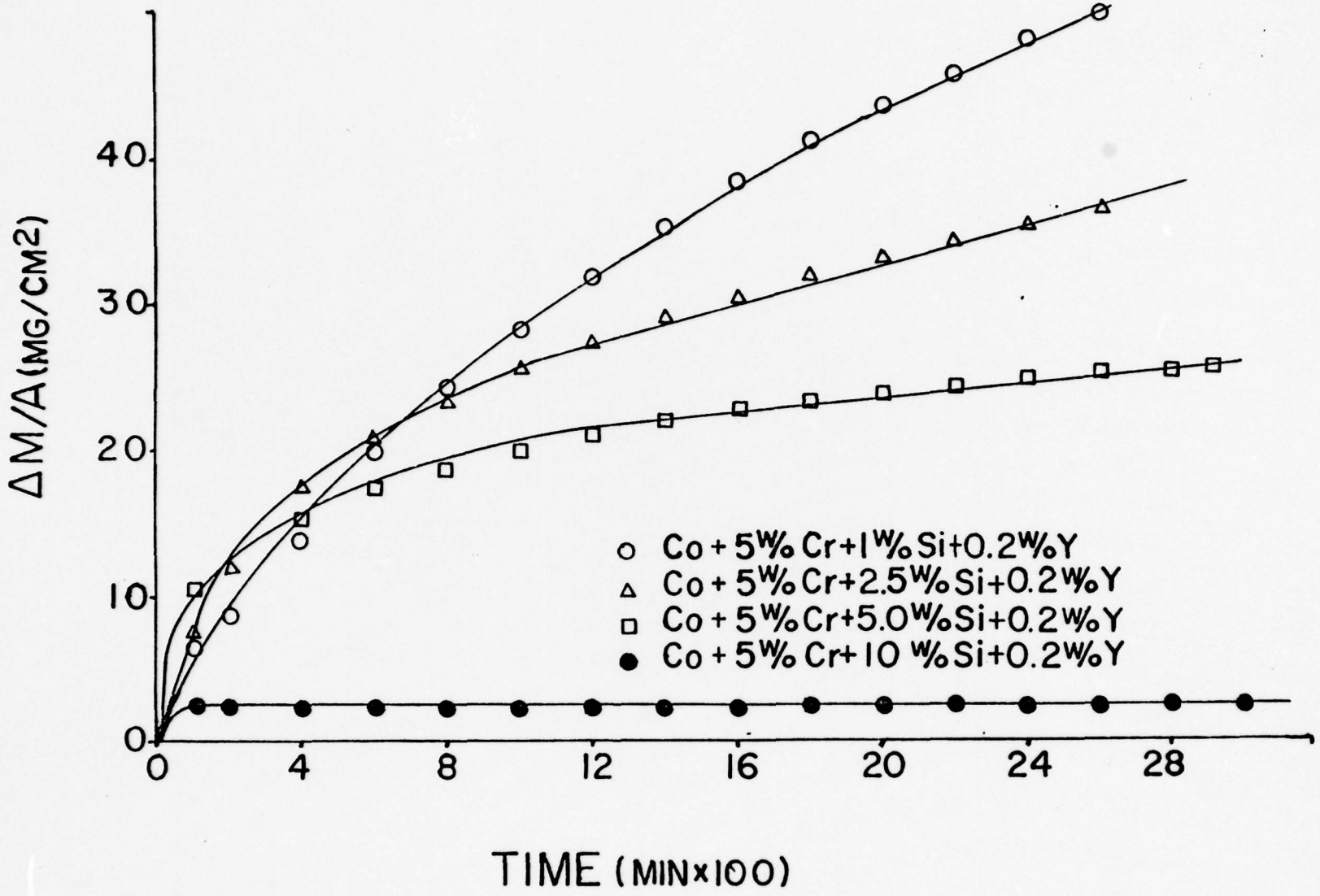
The hot corrosion of the Co-Cr-Si-Y alloys exhibits typical accelerated oxidation. The results of the thermogravimetric studies of the hot corrosion behavior of the Co-5 Cr-0.2 Y-Si alloys is shown in Figure 19. The results are listed in Table 2. The hot corrosion behavior appears parabolic for the 2.5% Si and 5% Si alloys, while a somewhat deviated behavior occurs with the 1% Si and 10% Si alloys.

The oxidation under hot corroding conditions is greatly accelerated especially with the low silicon alloys. Much higher oxidation rate constants and total weight gain values are reported, as compared to those reported under strictly oxidizing conditions. Increasing the silicon concentration greatly reduces the oxidation rate and total weight gain under hot corrosive conditions. The Co-5 Cr-0.2 Y-10 Si alloy oxidized under hot corrosive conditions exhibits a slight reduction in the oxidation rate as compared to the value determined under solely oxidizing conditions. The amount of weight gained is slightly higher: 2.47 mg under hot corrosion as compared to 1.16 mg weight gain per unit area in an oxidizing environment.

The Co-10 Cr-0.2 Y-Si alloys show the same tendencies as noted for the Co-5 Cr-0.2 Y-Si alloys oxidized under hot corroding conditions. Figure 20 illustrates the parabolic behavior for the Co-10 Cr-0.2 Y-Si alloys hot corroded. A decrease of four orders of magnitude in the oxidation rate occurs as the silicon concentration was increased from

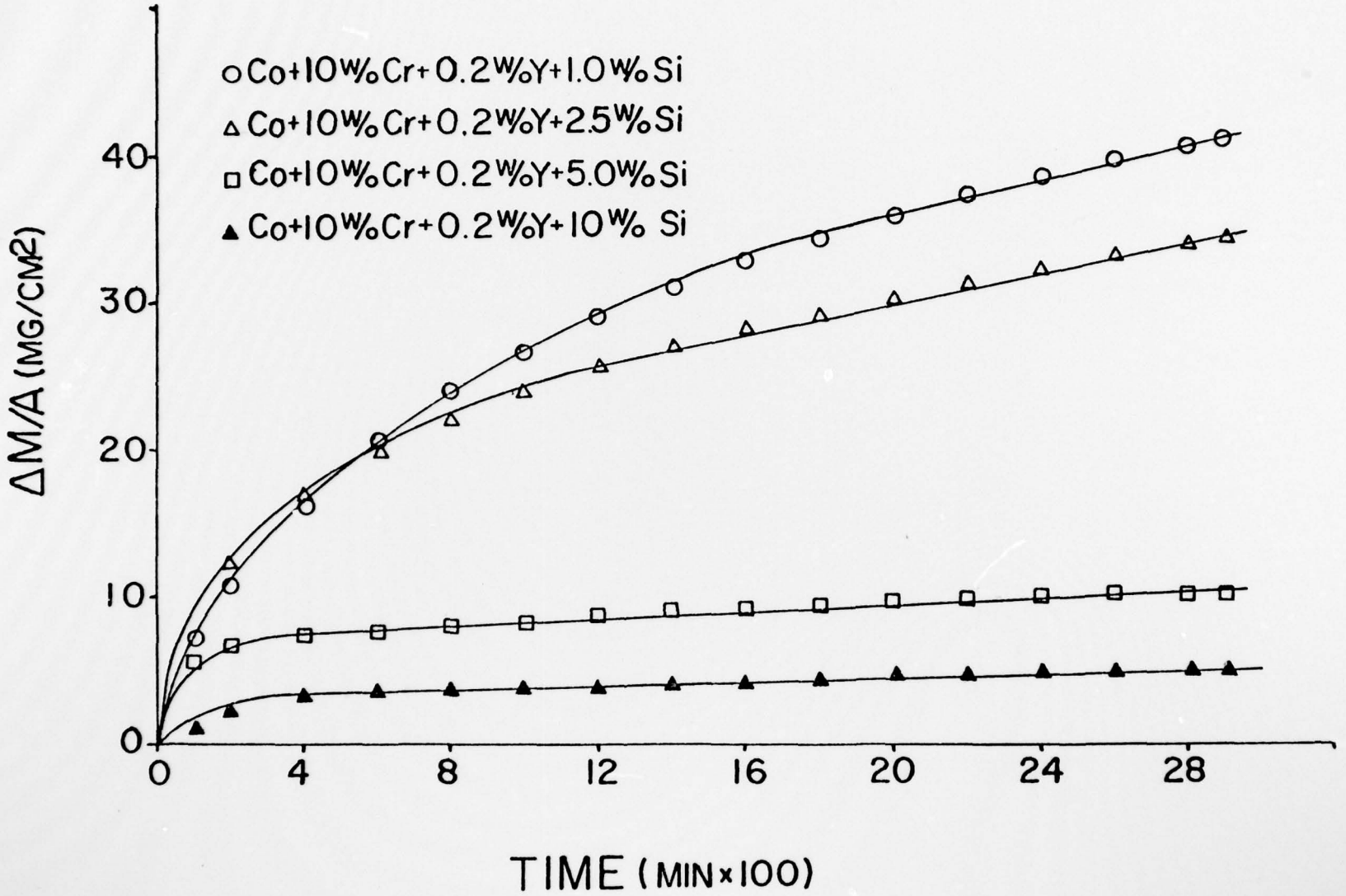
Blank.

Figure 19. ($\Delta M/A$) versus time of hot corrosion of Co- 5Cr- 0.2Y- Si alloys.


ΔM/A (MG/CM2)
40
30
20
10
0
0
4
8
12
16
20
24
28
TIME (MIN×100)
○ Co + 5W% Cr + 1W% Si + 0.2W% Y
△ Co + 5W% Cr + 2.5W% Si + 0.2W% Y
□ Co + 5W% Cr + 5.0W% Si + 0.2W% Y
● Co + 5W% Cr + 10 W% Si + 0.2W% Y

Blank

Figure 20. ($\Delta M/A$) versus time of hot corrosion of Co- 10Cr- 0.2Y- Si alloys.


○ Co+10W%Cr+0.2W%Y+1.0W% Si
△ Co+10W%Cr+0.2W%Y+2.5W% Si
□ Co+10W%Cr+0.2W%Y+5.0W% Si
▲ Co+10W%Cr+0.2W%Y+10W% Si
ΔM/A (MG/CM2)
0
10
20
30
40
0
4
8
12
16
20
24
28
TIME (MIN×100)

1% Si to 10% Si in the alloy. The total weight gained per unit area is decreased simultaneously.

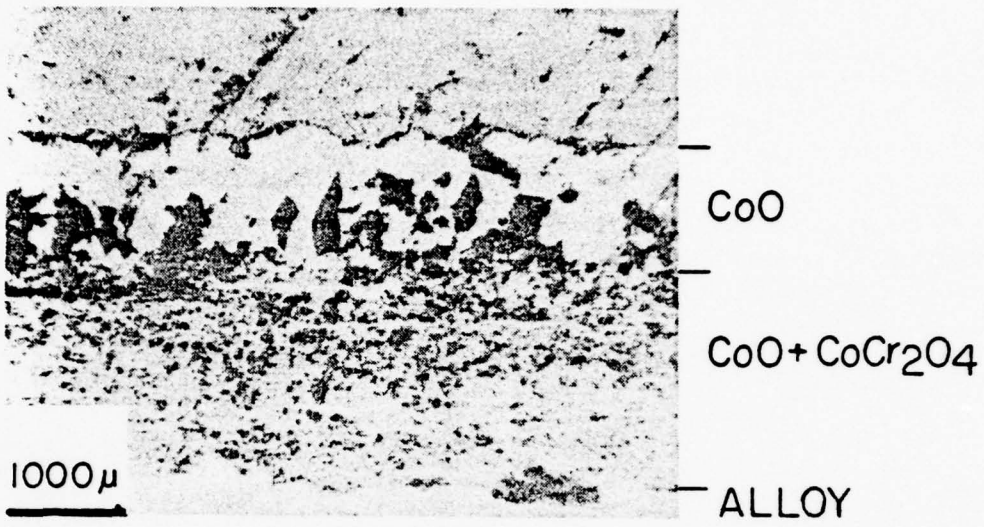
The scales formed under hot corroding conditions were generally thicker than under oxidizing conditions but were still double layered. The outer layer, identified by x-ray diffraction studies as being primarily CoO, consisted of large pores concentrated near the interface between the outer and inner layer as seen in the photomicrograph of the Co-10 Cr-0.2 Y-2.5 Si alloy in Figure 21. The inner layer contained much smaller pores and was much more compact near the alloy/scale interface. X-ray analysis showed the inner layer to consist of $CoCr_2O_4$. No $CoSi_2O_4$ was found. Microprobe results for the Co-10 Cr-0.2 Y-2.5 Si alloy did show significant silicon concentrations in the inner layer of the scale (see Figure 22). The increase in the hot corrosion resistance with increasing silicon content in the alloys can be attributed to an increase in the amounts of silicon oxide within the inner scale, especially near the alloy/scale interface. Microprobe techniques failed to identify any sodium or sulfur concentrations in the alloy or the scale.

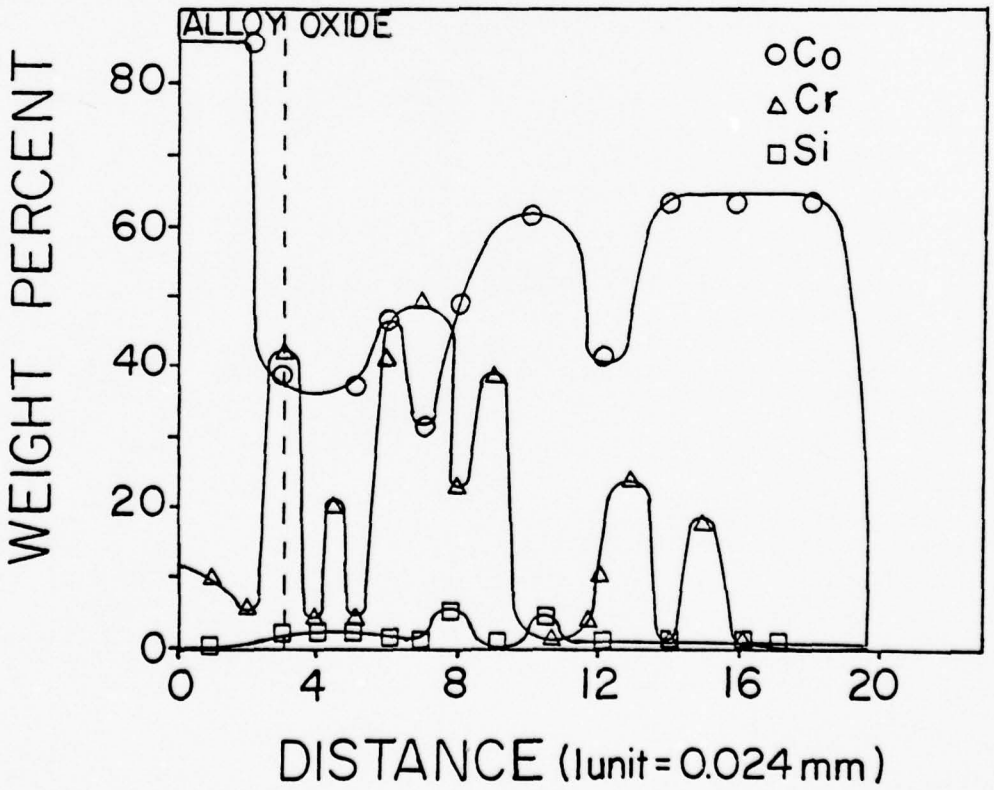
As the chromium concentration was increased to 5% Cr, the hot corrosion behavior began to deviate from the near parabolic hot corrosion behavior noted for the 5 and 10% Cr sets. This may be seen by comparing Figure 23, the hot corrosion behavior curves for the Co-15 Cr-0.2 Y-Si alloys, with Figures 19 and 20, the hot corrosion behavior curves for the 5 and 10% Cr containing alloys. This deviation is only observed in the 1 and 2.5% Si alloys. The 5% Si alloy shows a more reduced reaction rate, following the initial period of accelerated weight gain, than would be expected from normal parabolic behavior.

Blank

Figure 21. Photomicrograph of the cross-section of the scale formed on Co- 10Cr- 0.2Y- 2.5Si alloy after hot corrosion.

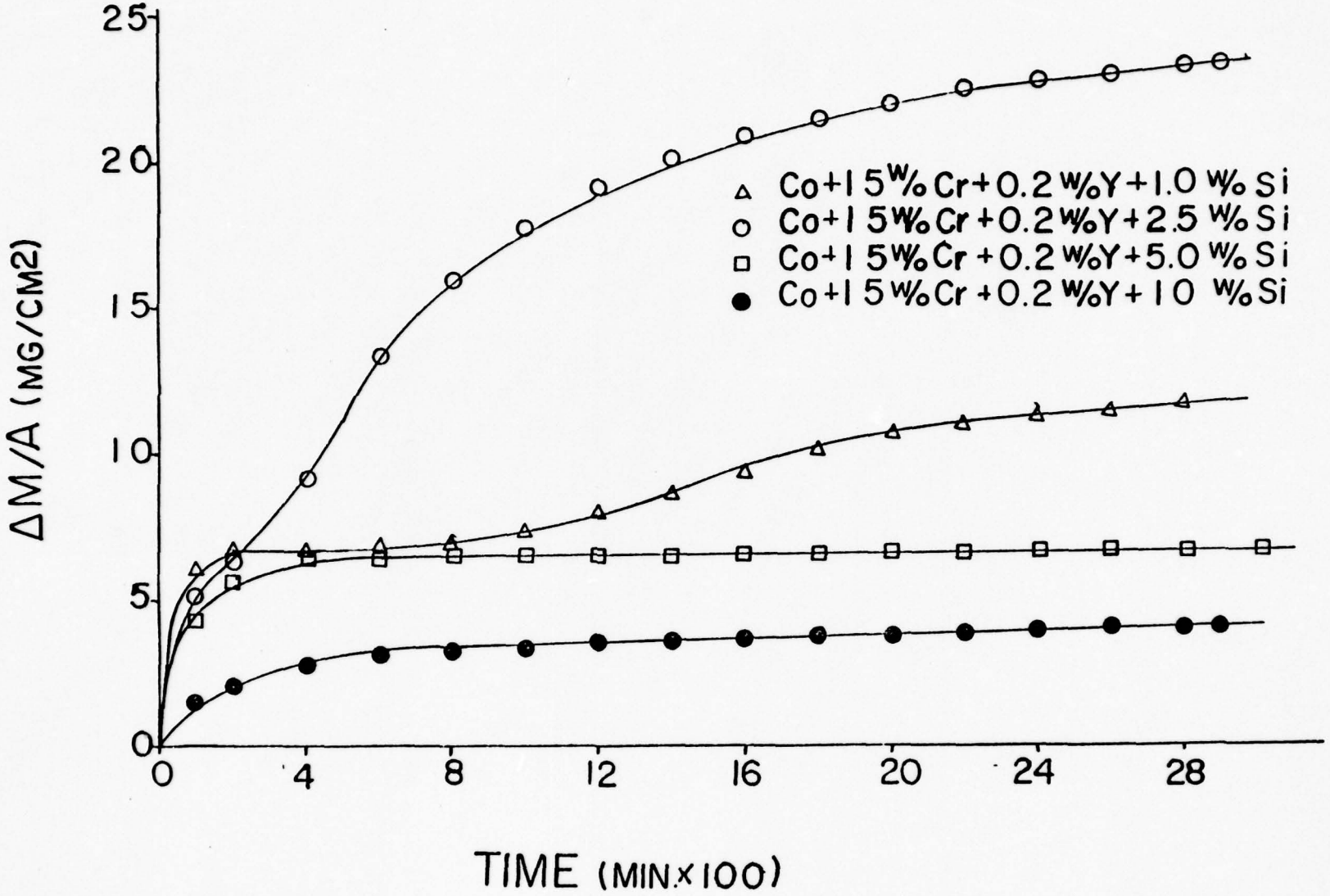
Figure 22. Microprobe profile of Co- 10Cr- 0.2Y- 2.5Si alloy after hot corrosion.


CoO
CoO+CoCr2O4
1000μ
ALLOY


ALLOY
OXIDE
Co
Cr
Si
WEIGHT PERCENT
0
20
40
60
80
0
4
8
12
16
20
DISTANCE (1unit = 0.024 mm)

Blank

Figure 23. ($\Delta M/A$) versus time of hot corrosion of Co- 15Cr- 0.2Y- Si alloys.


25
20
15
10
5
0
ΔM/A (MG/CM2)
0
4
8
12
16
20
24
28
TIME (MIN.×100)
Co+15W/o Cr+0.2 W/o Y+1.0 W/o Si
Co+15W/o Cr+0.2 W/o Y+2.5 W/o Si
Co+15W/o Cr+0.2 W/o Y+5.0 W/o Si
Co+15W/o Cr+0.2 W/o Y+10 W/o Si

The changes noted above seem to become less obvious with increased silicon content of the alloy. The behavior of the 1% Si alloys under hot corrosion shows the greatest deviation from "parabolic" behavior. The deviation in the behavior of the 2.5% Si alloy is similar but much less pronounced. The oxidation rate for the 2.5% Si alloy is greater than that of the 1% Si alloy, 8.33×10^{-11} gm^2 cm^{-4} sec^{-1} compared with 3.42×10^{-11} gm^2 cm^{-4} sec^{-1}, respectively. The 5% Si alloy shows a reduction to 0.072×10^{-11} gm^2 cm^{-4} sec^{-1}, in the oxidation rate. This is less than what would be expected for parabolic behavior as discussed previously. The 10% Si alloy's hot corrosion behavior more closely resembles parabolic oxidation than the outer alloys in this set, and weight gain/unit area is the lowest in this set.

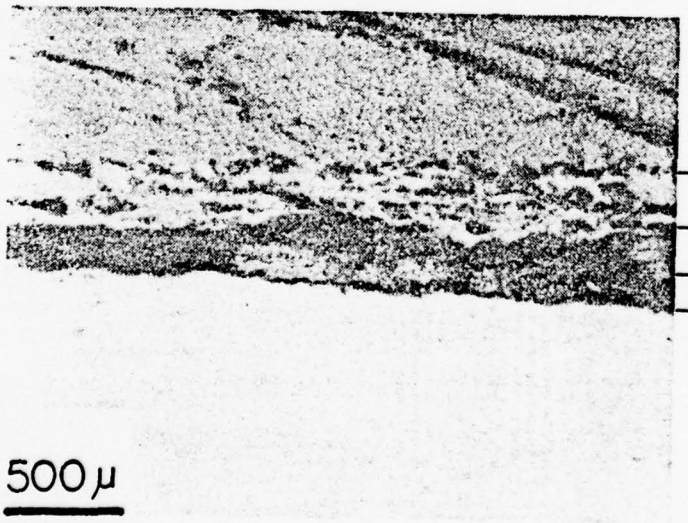
The structure of the scales formed on the 15% Cr alloys was again double layered. The scales were well adhered with the exception of the 10% Si alloy whose outer layer partially flaked off upon cooling. Typical scale cross-sections are seen in the photomicrographs of the 2.5 and 5% Si alloys in Figures 24 and 25, respectively. Scale analysis via microprobe and x-ray techniques show the outer scale to consist almost entirely of CoO with some $CoCr_2O_4$ and silicon oxide particles. The inner scale consisted primarily of $CoCr_2O_4$ and a higher concentration of Si as indicated by the microprobe profiles shown in Figures 26 and 27 for the 2.5 and 5% Si alloys, respectively. The presence of silicon oxides are assumed on the basis of the microprobe analysis. $CoSi_2O_4$ was only identified in the scale formed on the 10% Si alloy. It should also be noted that formation of a Cr_2O_3 layer is indicated by microprobe analysis in the 5 and 10% Si alloys. X-ray analysis of the 10% Si alloy did identify Cr_2O_3 as being present in the oxide.

Blank

Figure 24. Photomicrograph of the cross-section of the scale formed on Co- 15Cr- 0.2Y- 2.5Si alloy after hot corrosion.

Figure 25. Photomicrograph of the cross-section of the scale formed on Co- 15Cr- 0.2Y- 5Si alloy after hot corrosion.

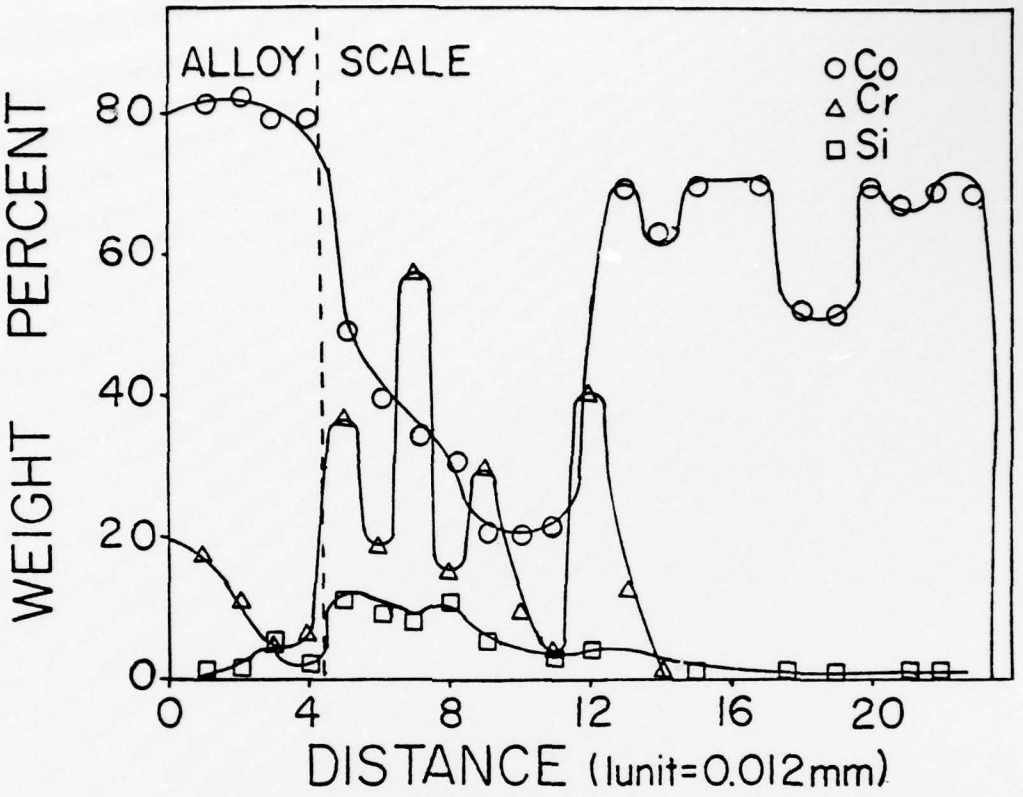

CoO
VOID
CoO + $CoCr_2O_4$
ALLOY
500 μ

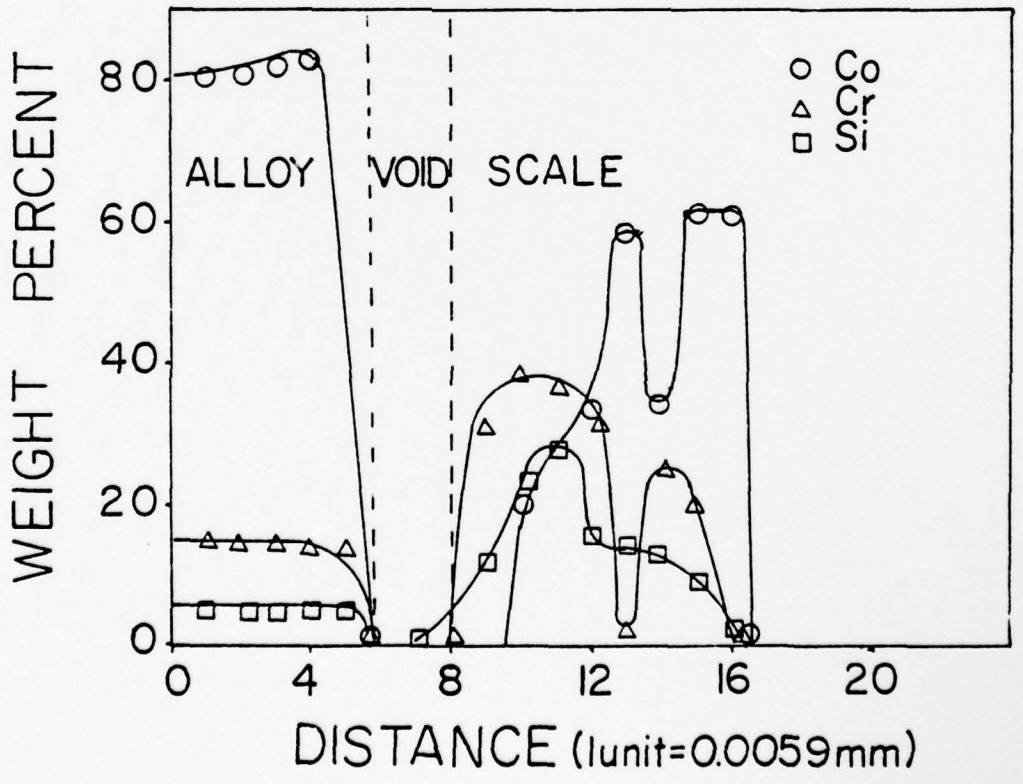

CoO
VOID
$CoCr_2O_4$ + Cr_2O_3
ALLOY
500 μ

Blank

Figure 26. Microprobe profile of Co- 15Cr- 0.2Y- 2.5Si alloy after hot corrosion.

Figure 27. Microprobe profile of Co- 15Cr- 0.2Y- 5Si alloy after hot corrosion.


ALLOY
SCALE
Co
Cr
Si
WEIGHT PERCENT
80
60
40
20
0
0
4
8
12
16
20
DISTANCE (1unit=0.012mm)


Co
Cr
Si
ALLOY
VOID
SCALE
WEIGHT PERCENT
80
60
40
20
0
0
4
8
12
16
20
DISTANCE (1unit=0.0059mm)

A possible explanation for the deviations in the hot corrosion behavior of this set of alloys may now be presented bearing the above discussion in mind. The accelerated rate of attack caused by a fluxing action of a liquid Na_2SO_4 layer decreased as a function of increased silicon content of the alloy. The 1% Si alloy showed the greatest rate of accelerated oxidation, which after 200 minutes became reduced to almost zero. This event may occur because of the formation of a protective Cr_2O_3 layer. During the following 600 minutes the concentration of CoO in the scale increased while the remaining Na_2SO_4 evaporated away. Due to the lack of chromium, the Cr_2O_3 layer is not stable and reacted with CoO forming a less protective $CoCr_2O_4$ layer, and the growth of the scale increased and approached a parabolic growth behavior. The 2.5 Si alloy showed an accelerated oxidation rate throughout the duration of the experiment possibly due to the inability to form a protective oxide layer during the initial 200 minutes of hot corrosion. The increased silicon concentration may be responsible for this by tieing up more oxygen and reducing the amount of Cr_2O_3 formed during the early stages of hot corrosion. The 5 and 10% Si alloys contain sufficient silicon to possibly form a protective SiO_2 layer during the early stages of oxidation. At longer times a Cr_2O_3 layer may eventually form below the initially formed SiO_2 layer, as the protectiveness of the SiO_2 layer breaks down.

The hot corrosion of the Co-20 Cr-0.2 Y-Si alloy deviated significantly from the nearly parabolic behavior noted previously for the 5 and 10% Cr alloy set. This behavior is shown in Figure 28. It may be characterized by an initial accelerated oxidation followed

by a rapid decrease in the reaction rate to very low values which remain throughout the duration of the test. The 1% Si alloy showed a slightly accelerated rate after 800 minutes which was very similar to the behavior of the Co-15 Cr-0.2 Y-1 Si alloy.

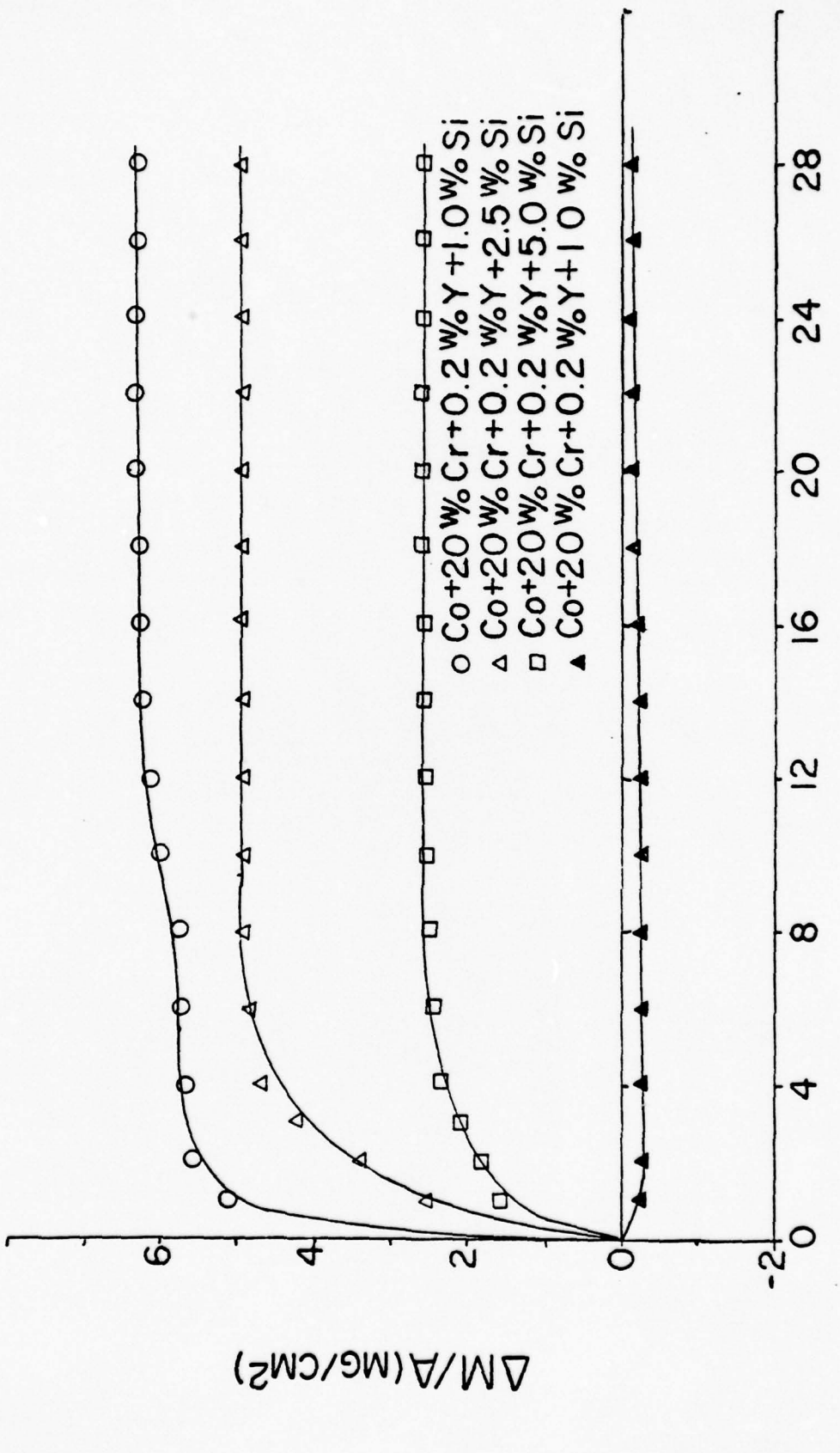
The results of the thermogravimetric studies are presented in Table 2. The total weight gained during hot corrosion is decreased as a function of increased silicon content in the alloy. Also the rate of the initial accelerated weight gain is reduced accordingly. The weight loss noted for the 10% Si alloy is probably due to the evaporation of the liquid Na_2SO_4 layer. The 10% Si alloy appears very immune to fluxing action caused by a condensed layer of Na_2SO_4.

Metallographic examination showed the scales to be double layered. The photomicrograph of the 1% Si alloy presented in Figure 29, shows massive gaps and voids typical of the scales formed on severely hot corroded alloys. The photomicrograph of the 5% Si alloy presented in Figure 30 shows a much more compact scale. In general the scales formed had a tendency to partially spall upon cooling to room temperature, with the exception of the 10% Si alloy which formed a compact, well-adhered scale.

Microprobe and x-ray analysis indicated that the 1 and 2.5% Si alloys formed outer scales consisting of CoO, and inner scales of $CoCr_2O_4$ and Co_2SiO_4 particles in a CoO matrix. The higher silicon alloys formed an outer layer of CoO and Cr_2O_3 particles, and an inner layer consisting of Co_2SiO_4 and CoO in a Cr_2O_3 matrix. The microprobe profiles of the 1% Si and the 5% Si alloys are presented in Figures 31 and 32, respectively.

Blank

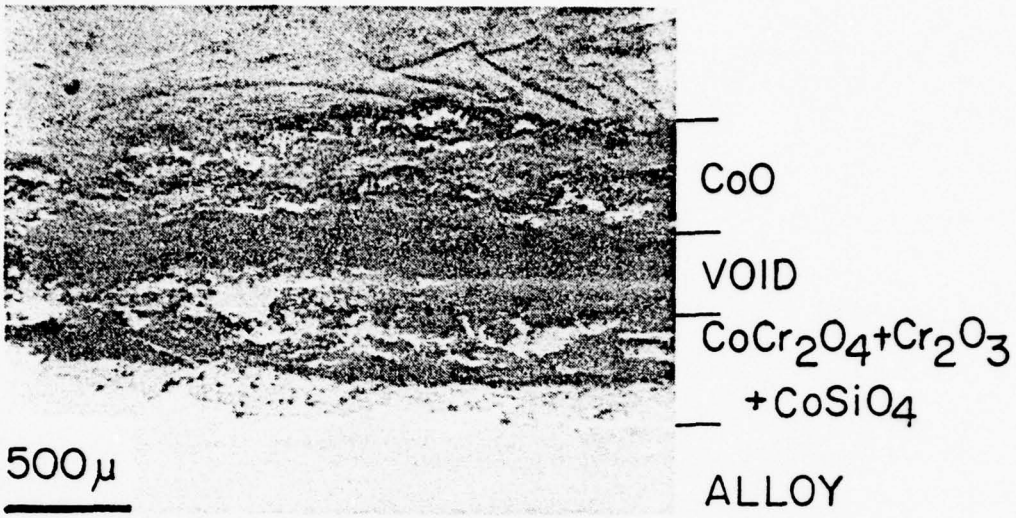
Figure 28. (ΔM/A) versus time of hot corrosion of Co- 20Cr- 0.2Y- Si alloys.

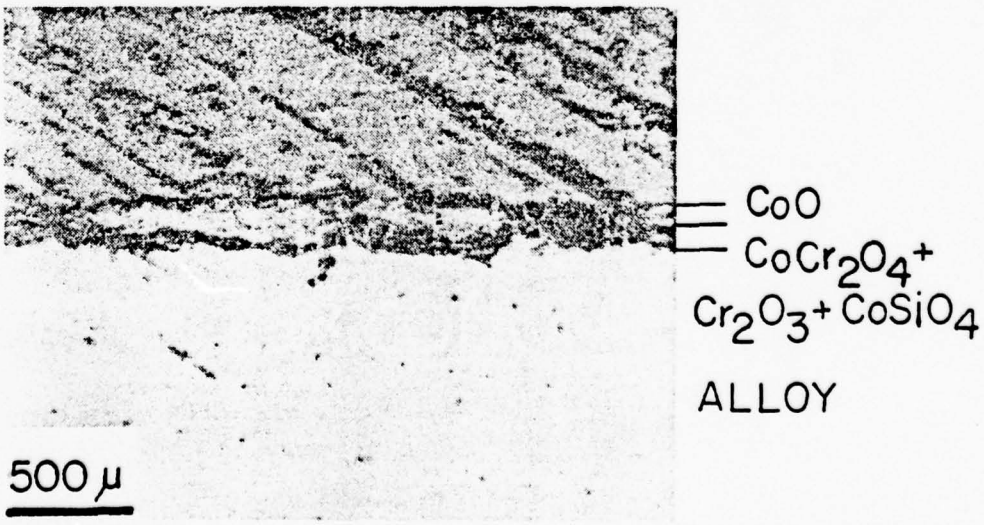

ΔM/A(MG/CM2)
6
4
2
0
-2
0
4
8
12
16
20
24
28
TIME (MIN×100)
○ Co+20 W% Cr+0.2 W% Y+1.0 W% Si
△ Co+20 W% Cr+0.2 W% Y+2.5 W% Si
□ Co+20 W% Cr+0.2 W% Y+5.0 W% Si
▲ Co+20 W% Cr+0.2 W% Y+1 0 W% Si

Blank

Figure 29. Photomicrograph of the cross-section of the scale formed on Co- 20Cr- 0.2Y- 1Si alloy after hot corrosion.

Figure 30. Photomicrograph of the cross-section of the scale formed on Co- 20Cr- 0.2Y- 5Si alloy after hot corrosion.


CoO
VOID
$CoCr_2O_4+Cr_2O_3$
$+CoSiO_4$
ALLOY
500 μ


CoO
$CoCr_2O_4+$
$Cr_2O_3+CoSiO_4$
ALLOY
500 μ

B. G.E. X-40 Series

1. Oxidation

The commercial cobalt-based superalloy, G.E. X-40, has been modified with increasing silicon contents in order to determine the changes in the oxidation resistance and the hot corrosion resistance accompanying silicon additions, The alloying modifications investigated, the nominal composition of G.E. X-40 and the results of oxidation in a P_{O_2} of 0.1 atm at 1000°C are reported in Table 3. Figure 33 shows the oxidation behavior of this set of alloys. The parabolic oxidation rates determined were all very low. Silicon additions resulted in a decrease of the parabolic rate constant and $\frac{\Delta m}{A}$ (total weight gain) as a function of increased silicon concentrations. The oxidation rate of the 10 wt % Si modified G.E. X-40 alloy (0.66×10^{-11} gm^2 cm^{-4} sec^{-1}) is more than an order of magnitude smaller than the oxidation rate of the unmodified G.E. X-40 alloy (2.46×10^{-11} gm^2 cm^{-4} sec^{-1}).

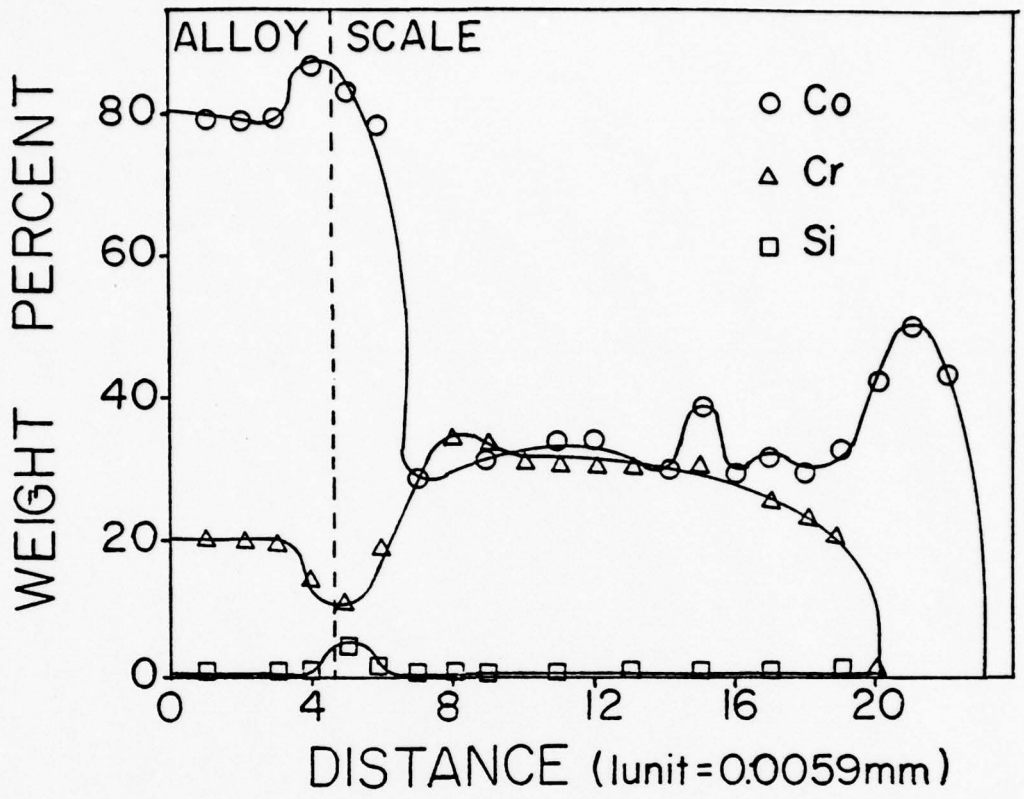
Attempts were made to add 0.2% Y to these alloys to aid in scale adherence. Chemical analysis of selected samples failed to identify any yttrium concentrations greater than 0.01 wt % Y. No attempts were made to analyze for concentrations below 0.01 wt % Y.

The silicon and yttrium modified alloys did however behave slightly different from the alloys modified only with silicon. Silicon modifications to this set of alloys caused a decrease in the oxidation rate as a function of increased silicon concentration. The exception is the 7.5 Si-0.2 Y alloy which showed a slightly higher oxidation rate as compared to the 5.0 Si-0.2 Y alloy. These results are tabulated in Table 3.

Blank

Figure 31. Microprobe profile of Co- 20Cr- 0.2Y- 1Si alloy after hot corrosion.

Figure 32. Microprobe profile of Co- 20Cr- 0.2Y- 5Si alloy after hot corrosion.


ALLOY
SCALE
Co
Cr
Si
WEIGHT PERCENT
0
20
40
60
80
0
4
8
12
16
20
DISTANCE (1unit=0.0059mm)

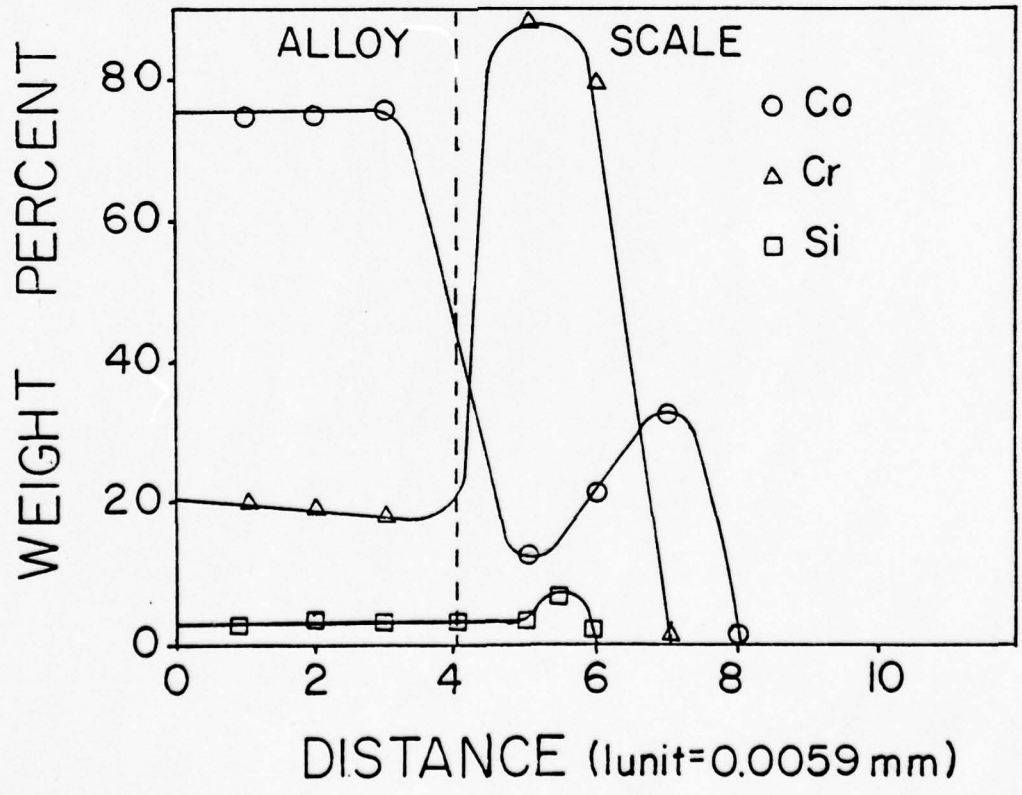

ALLOY
SCALE
Co
Cr
Si
WEIGHT PERCENT
0
20
40
60
80
0
2
4
6
8
10
DISTANCE (1unit=0.0059 mm)

Table 3

Parabolic-Rate Constant Data for G. E. X-40 Series

Co	Cr	C	Si	Mn	Fe	Ni	W
52.5	25.2	.5	1	1	2	11	7.5

Alloying Modifications	Oxidation		Hot Corrosion	
	$K_p \times 10^{11}$ ($gm^2 cm^{-4} sec^{-1}$)	$\frac{\Delta m}{A}$* (mg)	$K_r \times 10^{11}$ ($gm^2 cm^{-4} sec^{-1}$)	$\frac{\Delta m}{A}$** (gm)
None	2.46	2.72***	0.119	0.59
2.5% Si	1.36	1.73	0. 2	1.43
5% Si	1.08	1.63	0.063	1.78
10% Si	0.66	1.24	0.729	0.39
0.2% Y	1.69	2.22	0.263	0.69
2.5% Si + 0.2% Y	0.64	1.12****	0.292	1.104
5% Si + 0.2% Y	0.58	1.16	---	-0.90
7.5% Si + 0.2% Y	0.91	1.50	---	0.159
(7.5% Si + 0.2% Y)*****	0.87	1.41	---	---

*Standard Test Duration 4200 min.

**Standard Test Duration 2900 min.

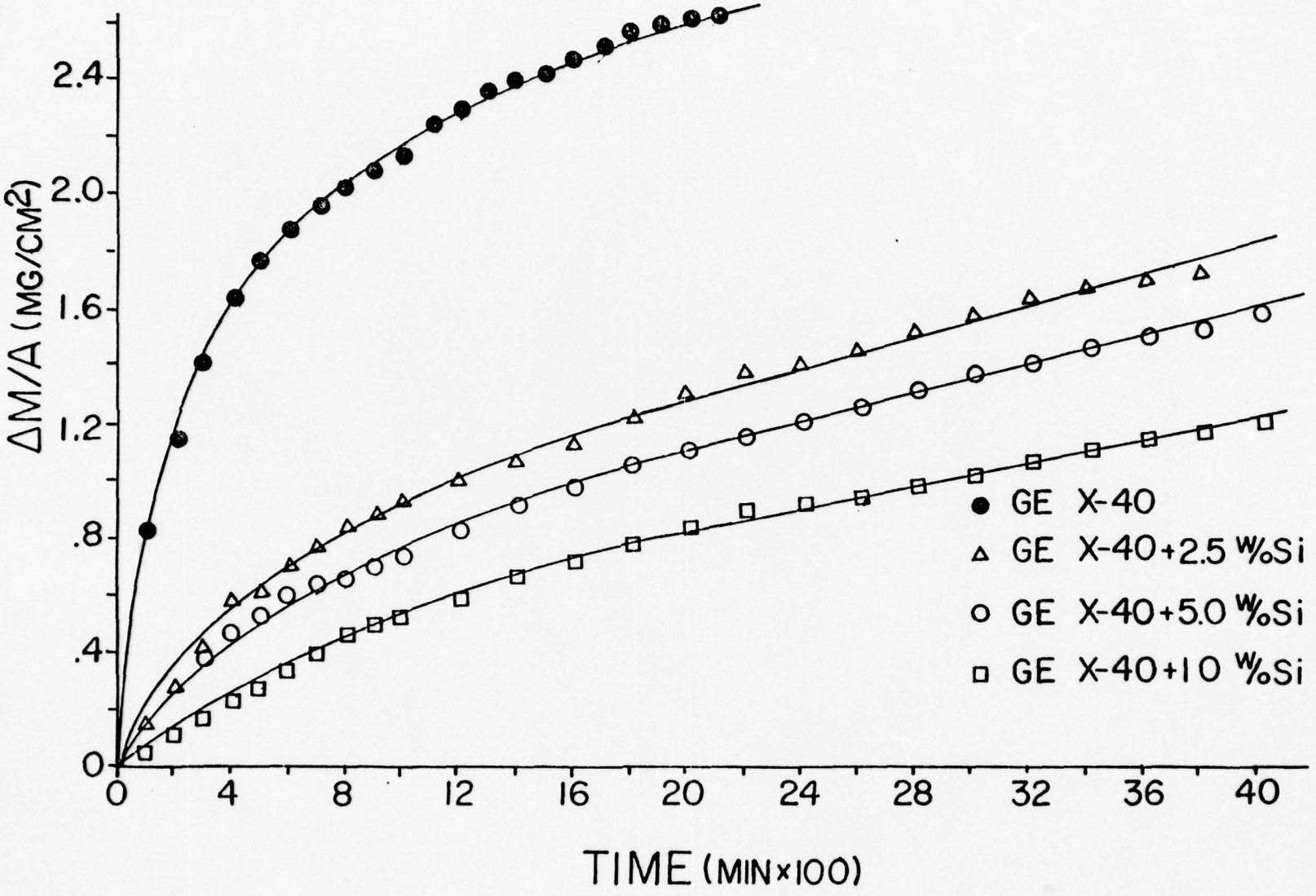
***Test Duration 2200 min.

****Test Duration 3300 min.

*****Reproducibility Check.

Blank

Figure 33. ($\Delta M/A$) versus time of oxidation of G.E. X-40 + Si set of alloys.


ΔM/A (MG/CM2)
2.4
2.0
1.6
1.2
.8
.4
0
0
4
8
12
16
20
24
28
32
36
40
TIME (MIN×100)
GE X-40
GE X-40+2.5 W%Si
GE X-40+5.0 W%Si
GE X-40+10 W%Si

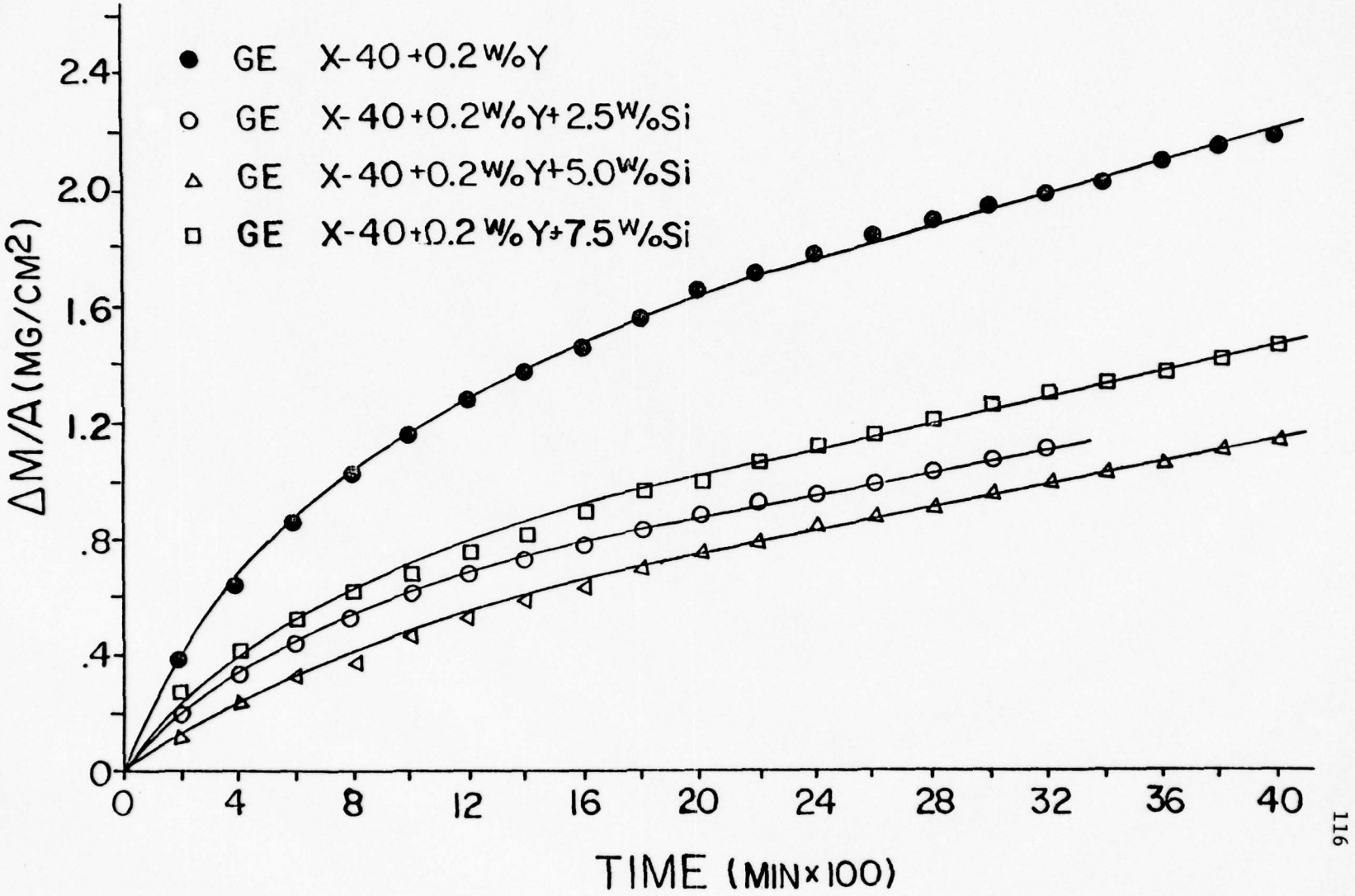
The oxidation behavior of the G.E. X-40 alloys modified with silicon and yttrium are presented in Figure 34. In general the Si-Y modified G.E. X-40 alloys showed a factor of 2 decrease in the oxidation rate compared to similarly composed silicon modified alloys.

The scales formed on these alloys during oxidation were very thin. Two layers were formed: an outer layer consisting primarily of CoO and some NiO and an inner layer consisting of $CoCr_2O_4$, Cr_2O_3, Co_2SiO_4, $CoWO_4$ with a mixture of maganese oxides. These compounds were identified with x-ray diffraction techniques. The outer layers formed on the 5, 7.5 and 10 wt % Si alloys were susceptible to spalling upon cooling to room temperature. A typical scale cross section is shown in Figure 35.

Micro analysis accomplished with the use of an electron microprobe revealed the distribution of elements across the oxide scale. Selected profiles are shown in Figures 36 and 37. In general, Co was distributed throughout the oxide. Chromium concentrations were also high, however, a complete layer of Cr_2O_3 was probably not formed. The low oxidation rates found for this set of alloys are primarily due to a dense layer of spinels $CoCr_2O_3$, Cr_2O_3, $CoSiO_2$, and $CoWO_4$. Elements such as nickel and iron were evenly distributed throughout the alloy or not present at all. Increased silicon concentrations in the alloy resulted in a densification of the spinel constituted inner layer, acting as a more effective block against ionic diffusion.

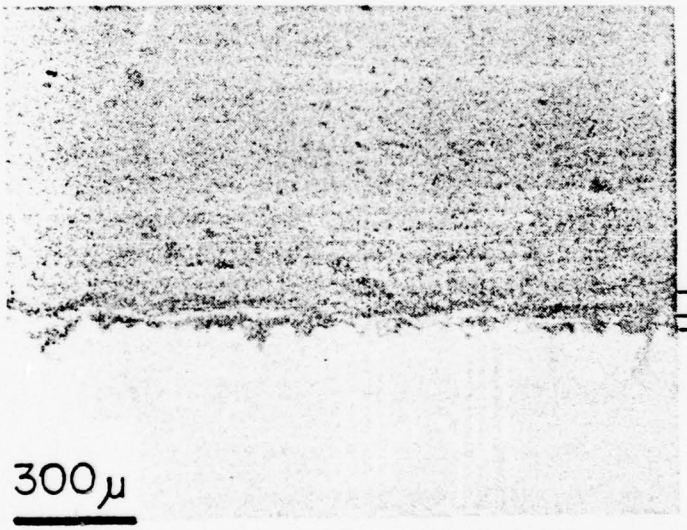
Blank

Figure 34. ($\Delta M/A$) versus time of oxidation of G.E. X-40 + Si + 0.2Y set of alloys.


GE X-40+0.2 W/o Y
GE X-40+0.2 W/o Y+2.5 W/o Si
GE X-40+0.2 W/o Y+5.0 W/o Si
GE X-40+0.2 W/o Y+7.5 W/o Si
ΔM/A (MG/CM2)
0
.4
.8
1.2
1.6
2.0
2.4
0
4
8
12
16
20
24
28
32
36
40
TIME (MIN×100)

Blank

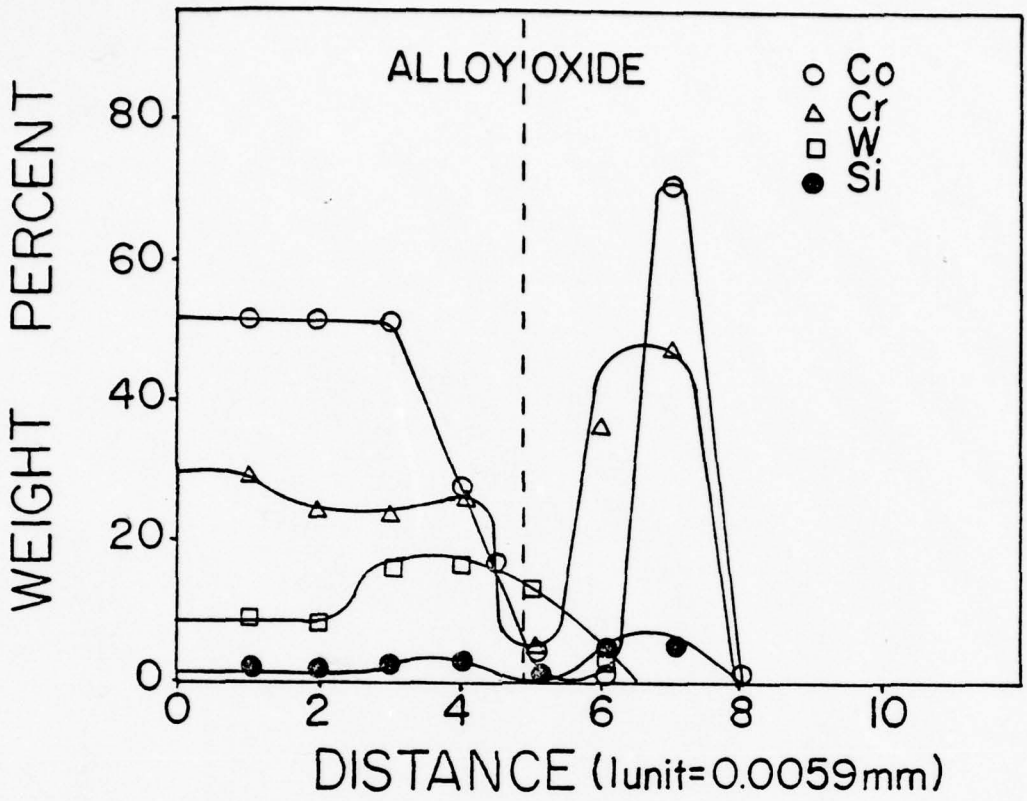
Figure 35. Photomicrograph of the cross-section of the scale formed on G.E. X-40 + 5Si alloy after oxidation.

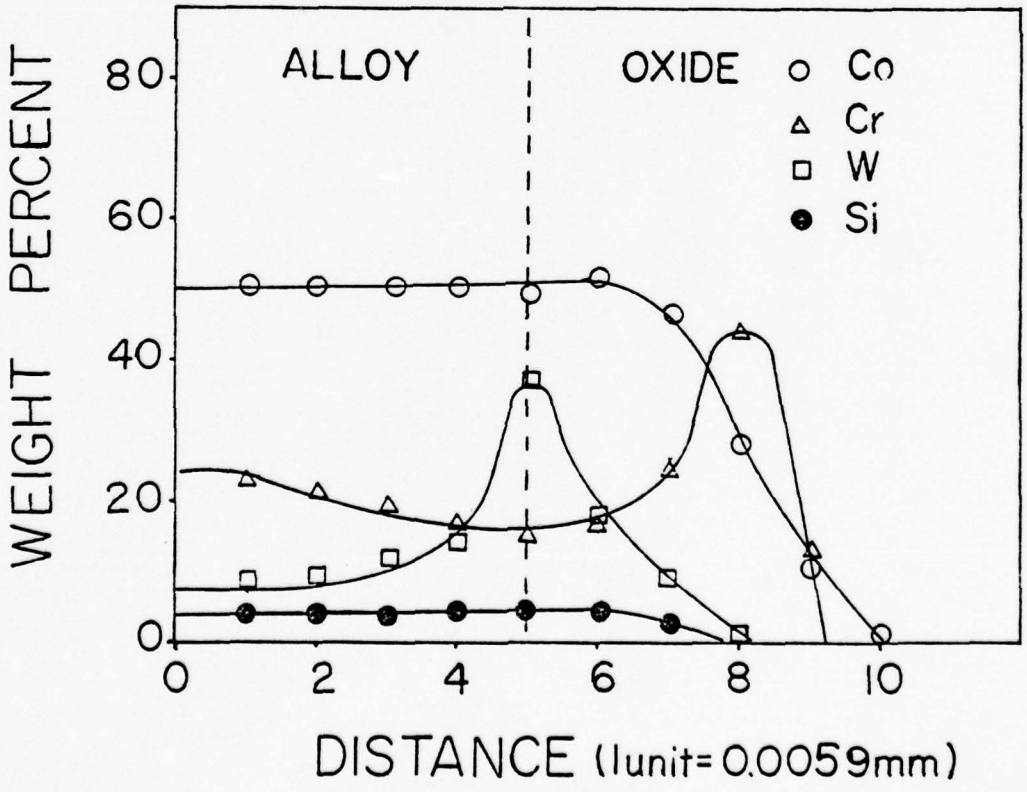

CoO
$CoCr_2O_4 + Cr_2O_4$
$+ CoWO_4 + Co_2SiO_4$
ALLOY
300μ

Blank

Figure 36. Microprobe profile of G.E. X-40 + 2.5Si + 0.2Y alloy after oxidation.

Figure 37. Microprobe profile of G.E. X-40 + 5Si alloy after oxidation.


ALLOY
OXIDE
Co
Cr
W
Si
WEIGHT PERCENT
80
60
40
20
0
0
2
4
6
8
10
DISTANCE (1unit=0.0059mm)


ALLOY
OXIDE
Co
Cr
W
Si
WEIGHT PERCENT
80
60
40
20
0
0
2
4
6
8
10
DISTANCE (1unit=0.0059mm)

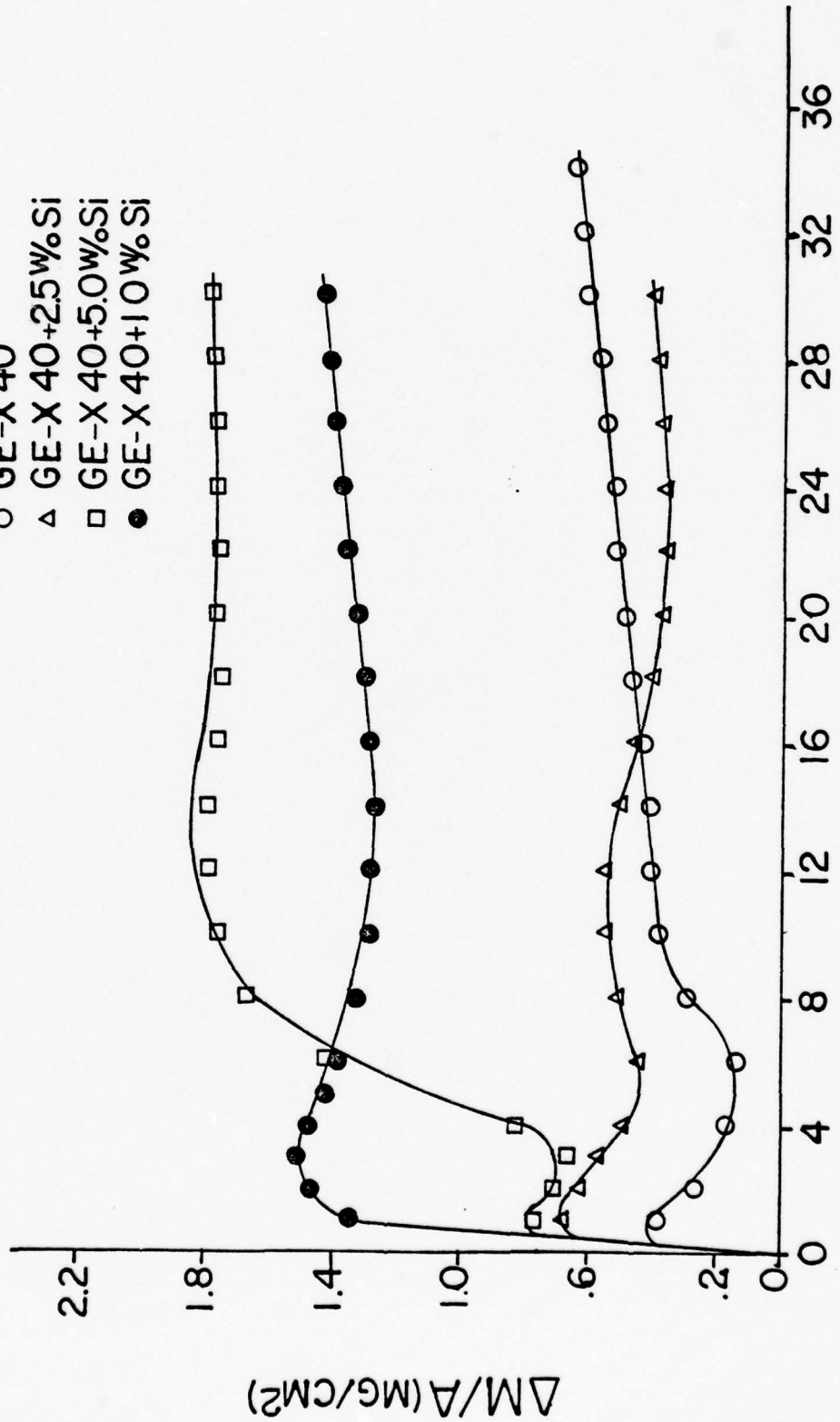
2. Hot Corrosion

The hot corrosion behavior of the G.E. X-40 series of alloys is shown in Figures 38 and 39 for the silicon modified alloys and the silicon-yttrium modified alloys, respectively. Table 3 lists the weight gain data and the calculated rate constants for each alloy studied. The hot corrosion behavior is characterized by an initial very rapid weight gain, followed by a weight loss. SO_2 and SO_3 gas evolution resulted from the increased sulfur activity due to the changed salt chemistry accompanying the fluxing of susceptible elements within the alloy. It is also possible that sodium sulfate may have itself vaporized. Following the period of weight loss, the samples gained weight at a very reduced rate. No effects from increased silicon concentration can be seen in the results of the thermogravimetric studies. It should be noted that G.E. X-40 alloys modified with silicon and yttrium displayed lower initial weight gains. In general all the alloys in this series showed lower or comparative weight gains to those observed during oxidation.

Metallographic examination of the scales formed on these alloys showed a very uneven metal/scale interface. The scales were thicker with significantly higher concentrations of pores distributed throughout the cross-section of the scale. Typical examples may be seen in Figures 40 and 41. The scales appeared to be single phase and not duplex in nature. The scales were very susceptible to spalling during cooling to room temperature. X-ray analysis identified the oxides comprising the scales. The hot corroded 2.5 wt % Si alloys formed CoO, Cr_2O_3 and $CoCr_2O_4$. The 5 wt % Si alloys formed Cr_2O_3, $CoCr_2O_4$,

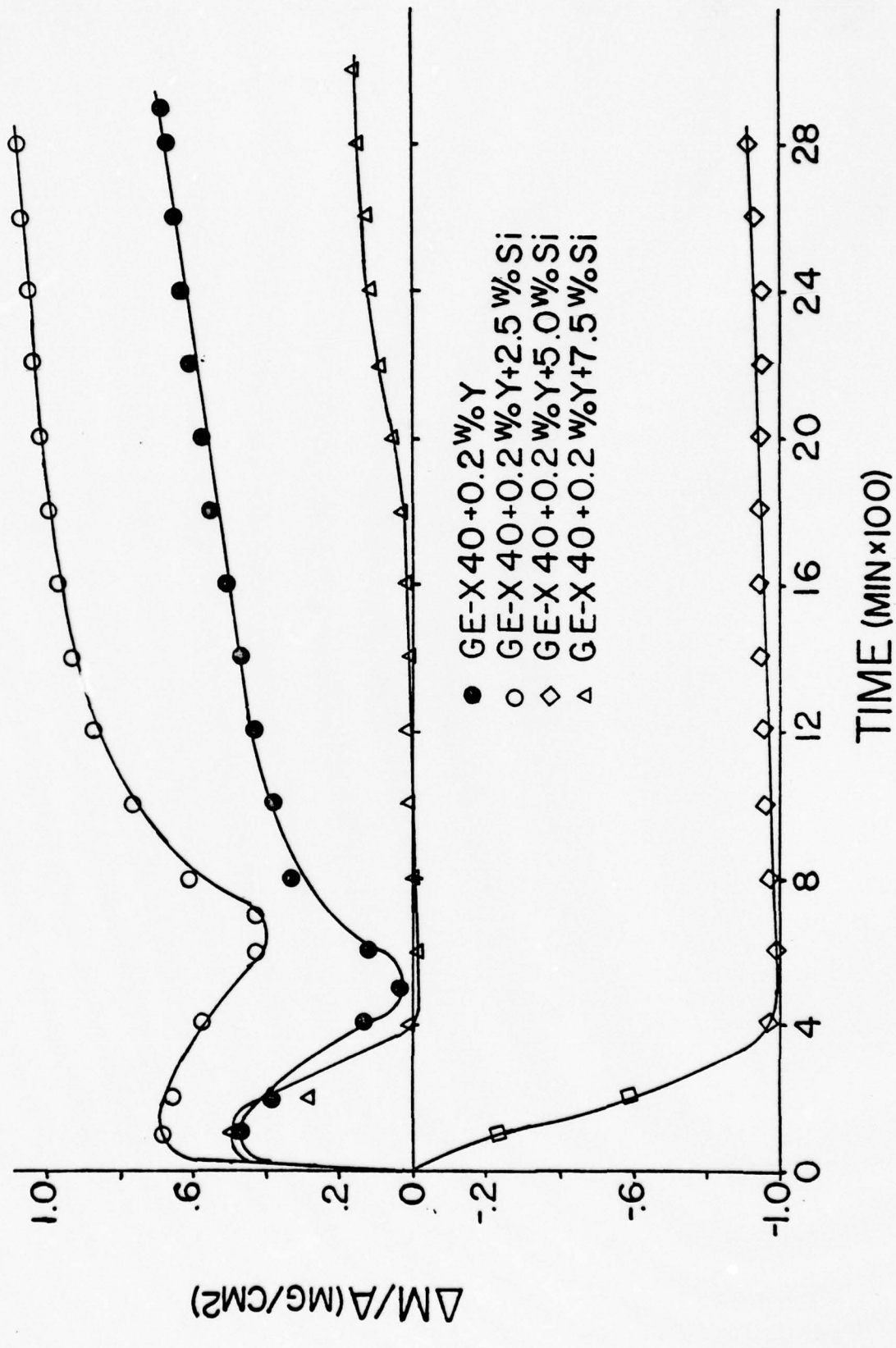
Blank

Figure 38. ($\Delta M/A$) versus time of hot corrosion of G.E. X-40 + Si set of alloys.


○ GE-X 40
△ GE-X 40+2.5W%Si
□ GE-X 40+5.0W%Si
● GE-X 40+10W%Si
ΔM/A (MG/CM2)
2.2
1.8
1.4
1.0
.6
.2
0
0
4
8
12
16
20
24
28
32
36
TIME (MIN×100)

Blank

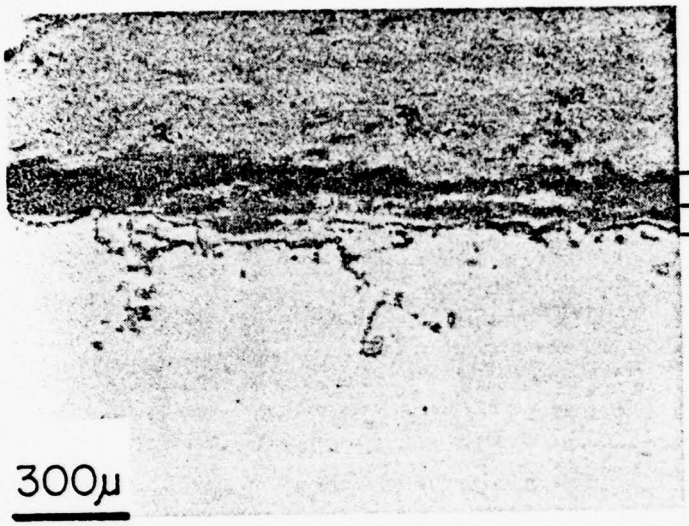
Figure 39. (ΔM/A) versus time of hot corrosion of G.E. X-40 + Si + 0.2Y set of alloys.


ΔM/A(MG/CM2)
1.0
.6
.2
0
-.2
-.6
-1.0
0
4
8
12
16
20
24
28
TIME (MIN×100)
GE-X40+0.2W%Y
GE-X40+0.2W%Y+2.5W%Si
GE-X40+0.2W%Y+5.0W%Si
GE-X40+0.2W%Y+7.5W%Si

Blank

Figure 40. Photomicrograph of the cross-section of the scale formed on G.E. X-40 alloy after hot corrosion.

Figure 41. Photomicrograph of the cross-section of the scale formed on G.E. X-40 + 10Si alloy after hot corrosion.


CoO
$CoCr_2O_4$
Cr_2O_3
ALLOY
300μ


CoO
$CoCr_2O_4$
Co_2SiO_4
ALLOY
300μ

some metallic cobalt and WO_3. The metallic cobalt became entrapped by the growing scale and remained unreacted due to the very low oxygen potentials present in the high silicon alloys. The 7.5 wt % Si alloys formed $CoCr_2O_4$ and Co_2SiO_4.

Microprobe investigations of the scales showed the existence of a Cr_2O_3 layer within the scale. The concentration of silicon was evenly distributed throughout the scale at concentrations no greater than that in the alloy. Manganese was distributed in much the same manner as the silicon.

The G.E. X-40 + 7.5 Si + 0.2 Y alloy showed a very high build-up of tungsten at the alloy surface and in the scale near the alloy/scale interface. The corresponding alloy modified with 10% Si showed no such build-up of tungsten. No evidence of sodium or sulfur was found in the scales or the alloy.

Results from the thermogravimetric studies showed no significant difference between the kinetics of the hot corrosion of G.E. X-40 + 7.5 Si + 0.2 Y and any other sample studied in this series. The relatively low weight gains found are due to the formation of a Cr_2O_3 protective layer following the period of initial accelerated weight gain. A continuous supply of Na_2SO_4, if used, may have continued the fluxing reaction and prevented the formation of this Cr_2O_3 protective layer.

C. Haynes 188 Series

1. Oxidation

The composition of the commercial cobalt-based alloy Haynes 188 is given in Table 4. This base alloy was modified further

Table 4

Parabolic-Rate Constant Data for Haynes 188 Series

Cr	C	Si	Mn	Fe	Ni	W	La
20-24	.05-.15	.2-.5	1.25 max	3.0	20-24	13-16	.03-0.15

Alloying Modifications	Oxidation		Hot Corrosion	
	$K_p \times 10^{11}$ ($gm^2 cm^{-4} sec^{-1}$)	$\frac{\Delta m}{A}$* (mg)	$K_r \times 10^{11}$ ($gm^2 cm^{-4} sec^{-1}$)	$\frac{\Delta m}{A}$** (mg)
None	0.48	0.91***	---	- 0.056
2.5% Si	0.78	1.04****	144.0	18.90
5% Si	1.06	1.74	13.2	4.74
7.5% Si	1.96	2.35	---	- 0.24
0.2% Y	0.37	0.93	5	13.66
2.5% Si + 0.2% Y	0.76	1.31	116	16.63
5% Si + 0.2% Y	1.00	1.44	---	- 0.425
7.5% Si + 0.2% Y	0.72	1.21	---	- 1.11

*Standard Test Duration 4200 min.

**Standard Test Duration 2900 min.

***Test Duration 2600 min.

****Test Duration 2900 min.

with silicon and yttrium additions. The alloy modifications and the results of the oxidation kinetic studies are also listed in Table 4.

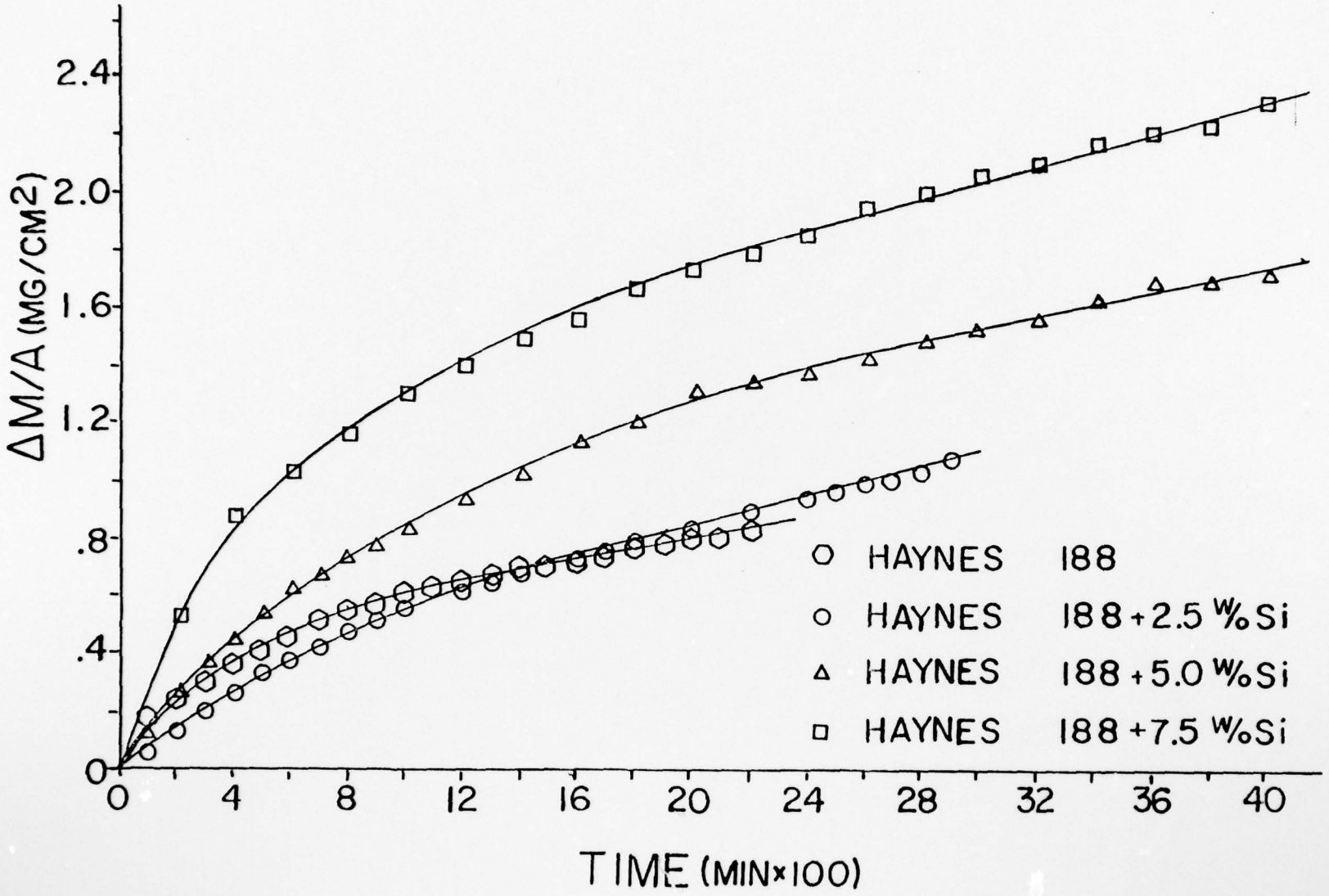
The results of the thermogravimetric studies are shown in Figure 42, for the silicon modified alloys, and Figure 43, for the silicon and yttrium modified alloys. The effect of increased silicon additions on the oxidation rate of these alloys is completely opposite to the trends established by the Co-Cr-Si-Y alloys and the G.E. X-40 series of silicon modified alloys. An increase in the oxidation rate was seen as a function of increased silicon concentration, see Figure 44. All the alloys exhibited a parabolic oxidation behavior. The silicon and yttrium modified alloys showed the same behavior as the silicon modified alloys with the exception of the 7.5 Si-0.2 Y modified alloy, whose rate decreased to 0.72×10^{-11} gm^2 cm^{-4} sec^{-1} from 1×10^{-11} gm^2 cm^{-4} sec^{-1}, the rate of the 5.0 Si-0.2 Y modified alloy.

Metallographic examination of the scales formed on these alloys revealed a duplex scale. Both layers were very thin. The high silicon containing alloys (5, 7.5 wt % Si), were very susceptible to spalling of the outer oxide layer upon cooling. A typical photomicrograph of the cross-section of the oxide layer formed on Haynes 188 alloy is shown in Figure 45.

X-ray analysis of the oxides formed on these alloys showed the formation of Cr_2O_3, $CoCr_2O_4$, CoO, and $CoWO_4$, with possible traces of NiO and manganese oxides. The base alloy, Haynes 188, contained no silicates whereas the higher silicon alloys (2.5, 5, 7.5 wt % Si alloys) formed Co_2SiO_4 within the inner oxide layer. Microprobe analysis indicated that the $CoWO_4$ phase is concentrated at the alloy oxide interface, followed by a distribution of Cr_2O_3, $CoSiO_4$, and $CoCr_2O_4$ spinels.

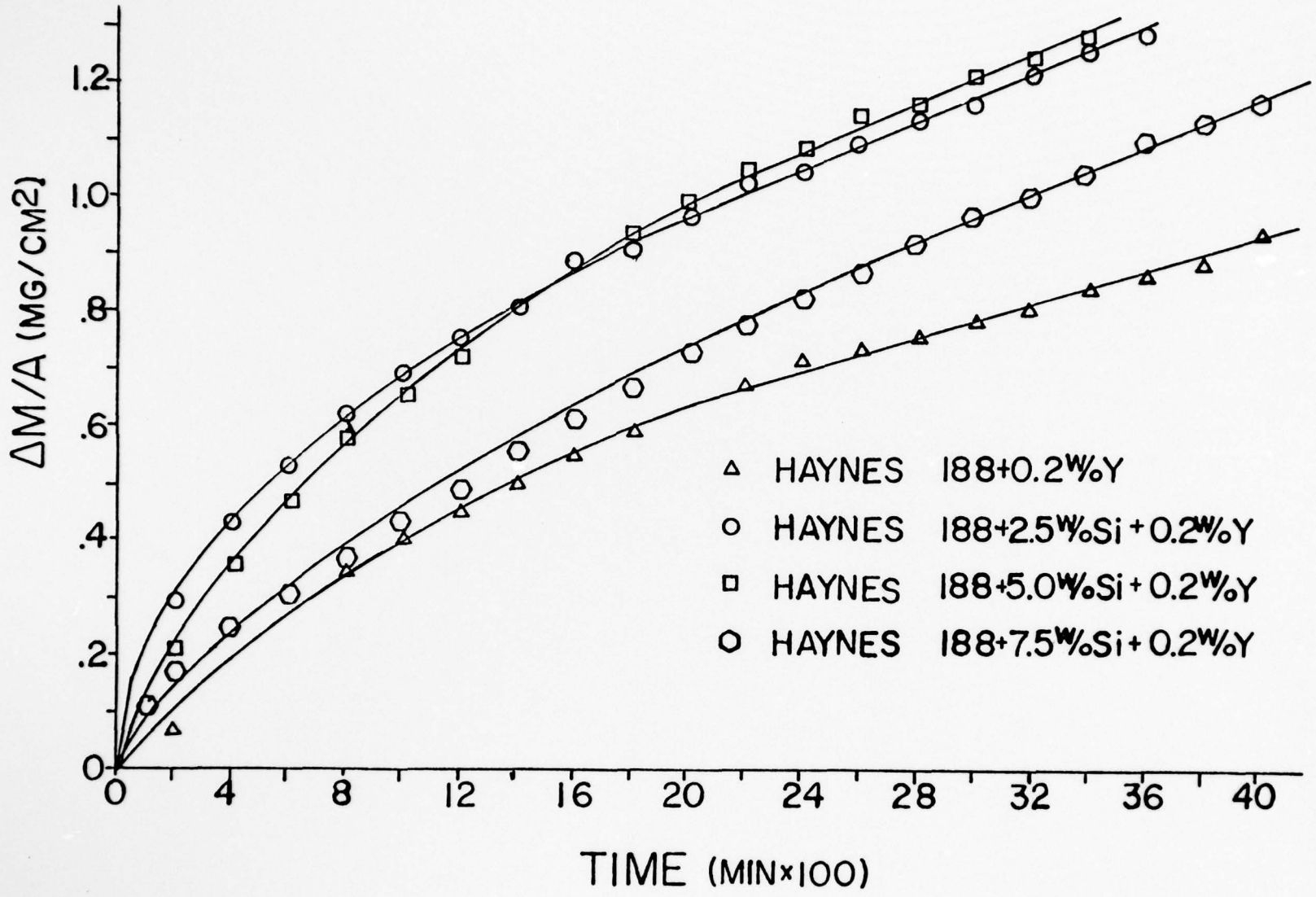
Blank

Figure 42. ($\Delta M/A$) versus time of oxidation of Haynes 188 + Si set of alloys.


ΔM/A (MG/CM2)
2.4
2.0
1.6
1.2
.8
.4
0
0
4
8
12
16
20
24
28
32
36
40
TIME (MIN×100)
HAYNES 188
HAYNES 188+2.5 W/o Si
HAYNES 188+5.0 W/o Si
HAYNES 188+7.5 W/o Si

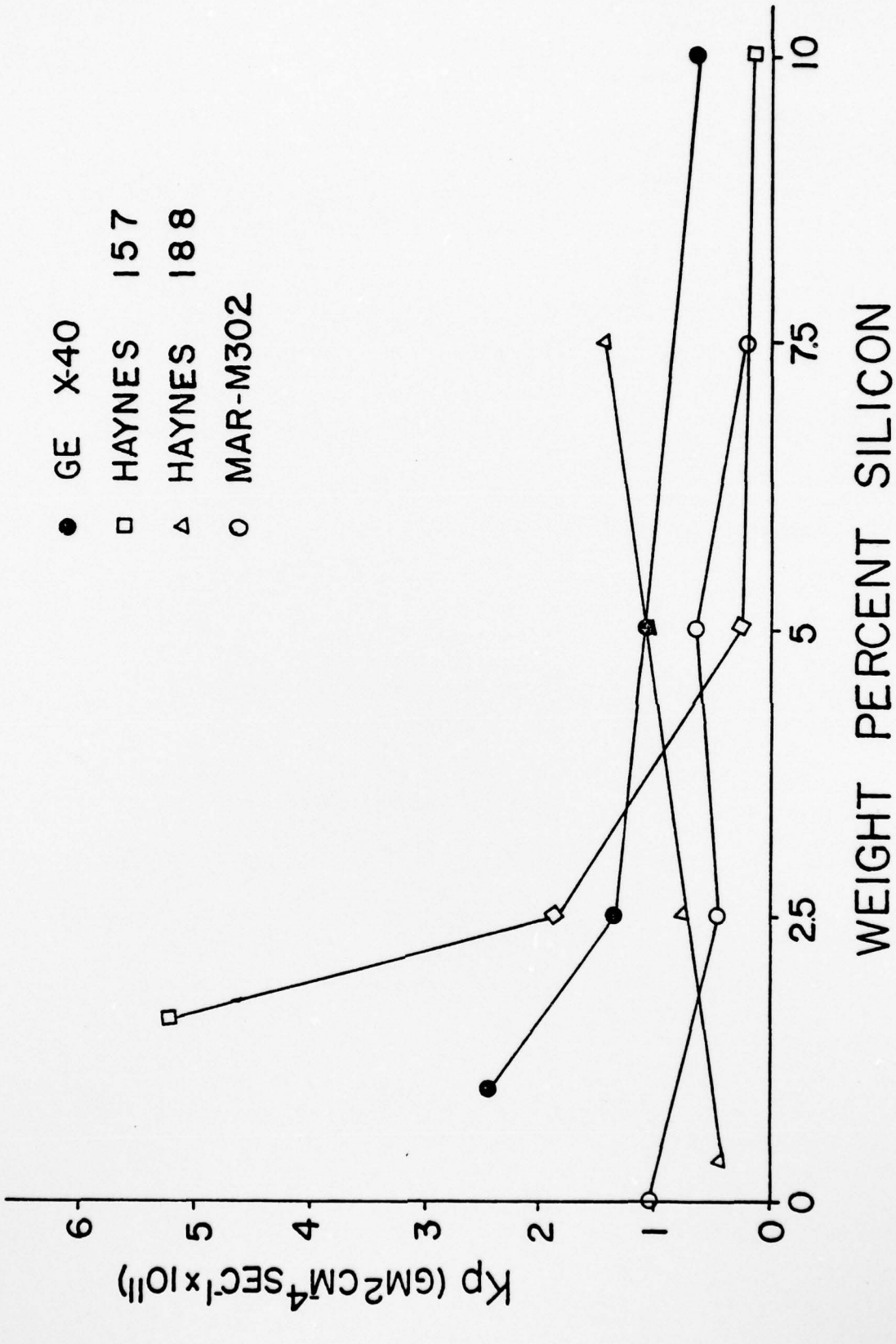
Blank

Figure 43. ($\Delta M/A$) versus time of oxidation of Haynes 188 + Si + 0.2Y set of alloys.


ΔM/A (MG/CM2)
1.2
1.0
.8
.6
.4
.2
0
0
4
8
12
16
20
24
28
32
36
40
TIME (MIN×100)
HAYNES 188+0.2W/oY
HAYNES 188+2.5W/oSi + 0.2W/oY
HAYNES 188+5.0W/oSi + 0.2W/oY
HAYNES 188+7.5W/oSi + 0.2W/oY

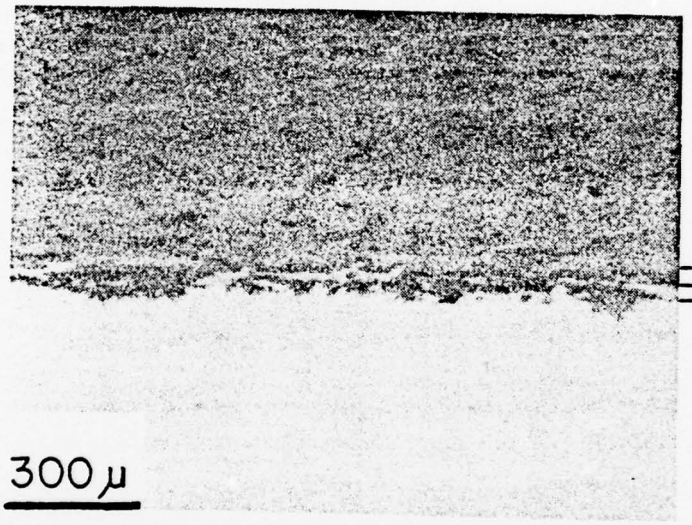
Blank

Figure 44. Parabolic oxidation rates of Haynes 188 series of alloys versus weight percent silicon.


GE X-40
HAYNES 157
HAYNES 188
MAR-M302
Kp (GM2CM4SEC-1x10II)
0
1
2
3
4
5
6
0
2.5
5
7.5
10
WEIGHT PERCENT SILICON

Blank

Figure 45. Photomicrograph of the cross-section of the scale formed on Haynes 188 alloy after oxidation.


CoO
Cr_2O_4 + $CoWO_4$
+ $CoCr_2O_4$
ALLOY
300 μ

Figures 46 and 47 are representative microprobe profiles. The outer oxide was very brittle and was significantly lost during polishing for microprobe analysis. The microprobe profiles show little about the outer oxide. One further observation is that silicon concentrations in the oxide peak at the same position where chromium concentrations peak. Scale scraping techniques for removing oxide specimens from the oxidized alloys for x-ray analysis showed a complete layer of a greenish oxide probably Cr_2O_3.

The analysis of the scales formed on the Haynes 188 series of alloys seem to indicate that the low oxidation rates are attributable to the formation of a complete Cr_2O_3 oxide layer within the oxide scale. The fact that the oxidation rate increased with increased silicon content of the alloys may be attributable to doping effects of SiO_2 in a Cr_2O_3 layer. Since Cr_2O_3 is a p-type semiconducting oxide, the addition of a higher valent cation species (SiO_2) will increase ionic transport through the rate controlling Cr_2O_3 oxide. This would be similar to the effect described by equation 12, representing the addition of SiO_2 in CoO.

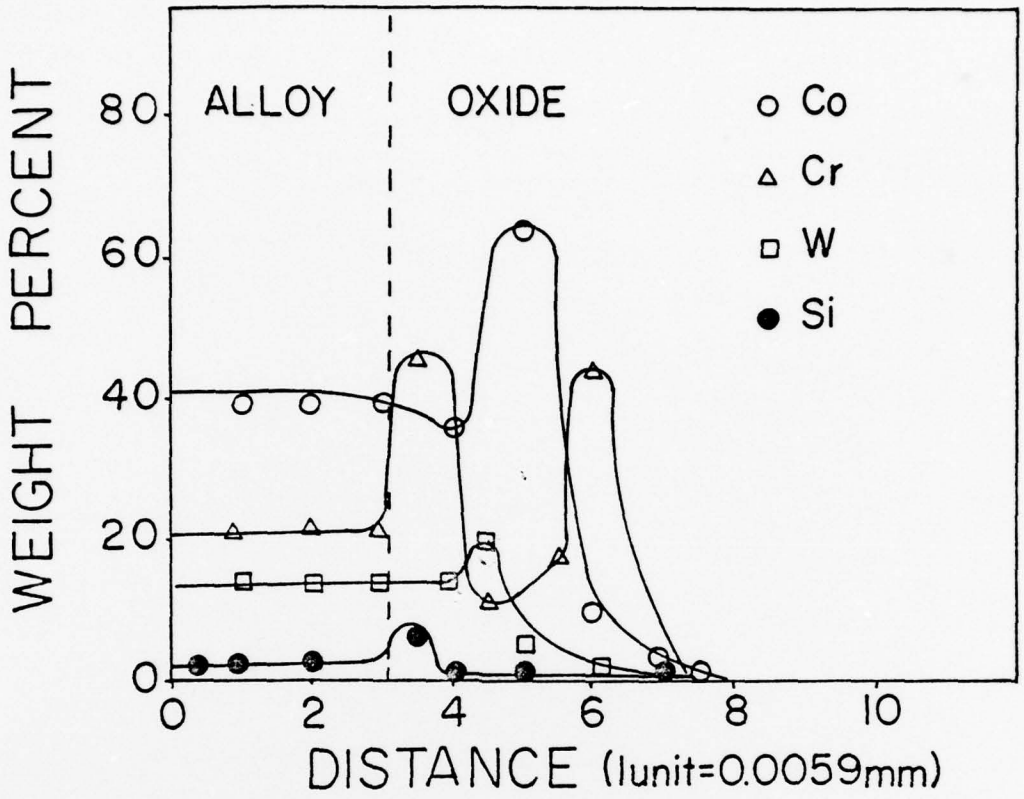
2. Hot Corrosion

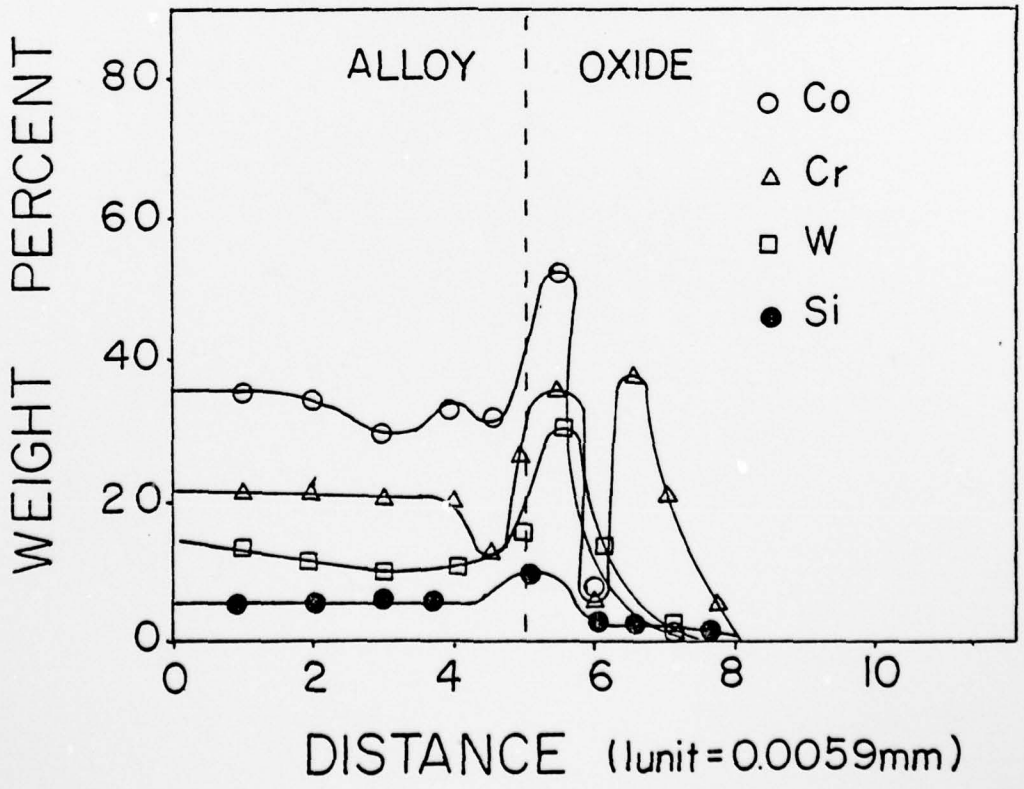
The hot corrosion of the Haynes 188 series of alloys showed no general trends of the weight gained per unit area as a function of increased silicon concentration. The results of the thermogravimetric analysis may be seen in Table 4, and Figures 48, 49 and 50. The hot corrosion behavior of both 2.5 wt % Si alloys appeared parabolic. Total weight gains per unit area were an order of magnitude greater than the weight gains reported for oxidation.

Blank

Figure 46. Microprobe profile of Haynes 188 + 2.5Si alloy after oxidation.

Figure 47. Microprobe profile of Haynes 188 + 2.5Si + 0.2Y alloy after oxidation.


ALLOY
OXIDE
Co
Cr
W
Si
WEIGHT PERCENT
0
20
40
60
80
0
2
4
6
8
10
DISTANCE (1unit=0.0059mm)

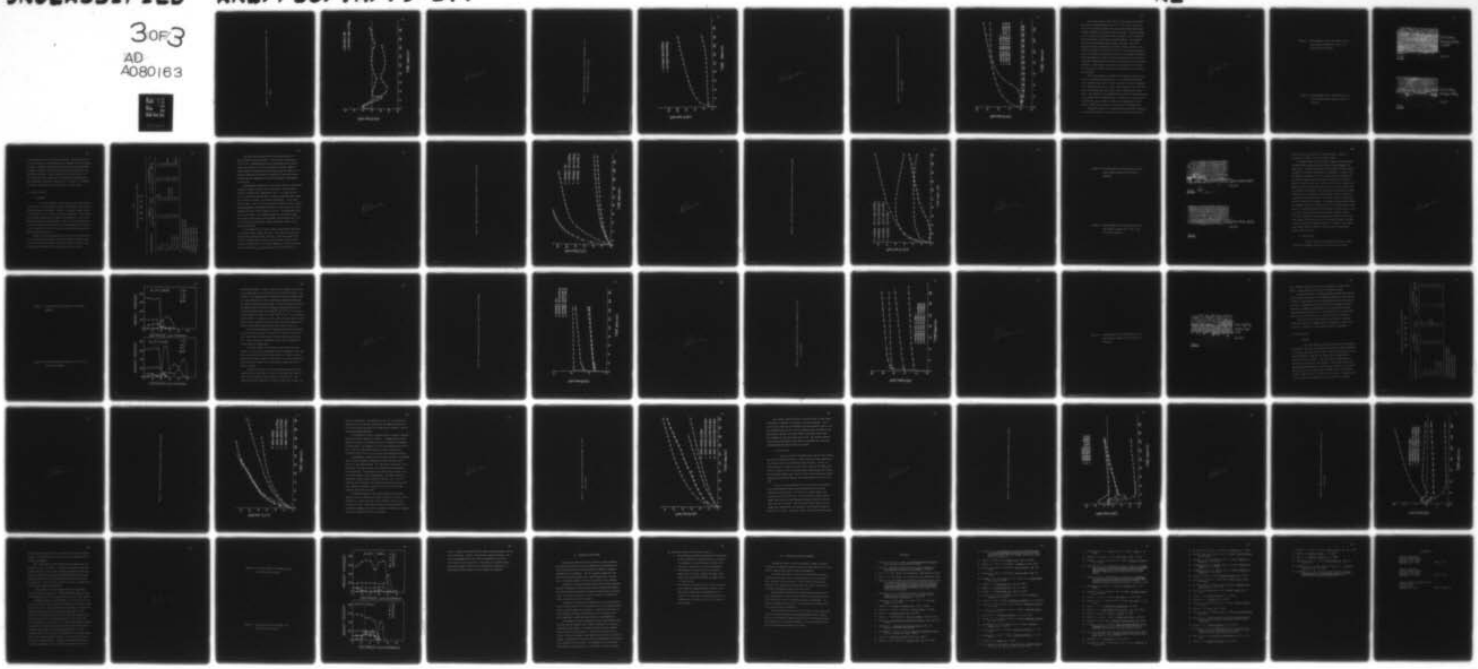

ALLOY
OXIDE
Co
Cr
W
Si
WEIGHT PERCENT
0
20
40
60
80
0
2
4
6
8
10
DISTANCE (1unit=0.0059mm)

Blank

AD-A080 163 PENNSYLVANIA STATE UNIV UNIVERSITY PARK APPLIED RESE--ETC F/G 11/6
HOT CORROSION AND OXIDATION STUDIES OF COBALT BASED SUPERALLOYS--ETC(U)
OCT 79 G A DRIES N00024-79-C-6043

UNCLASSIFIED ARL/PSU/TM/79-177 NL

3 OF 3
AD
A080163



END
DATE
FILMED
3-80
DDC

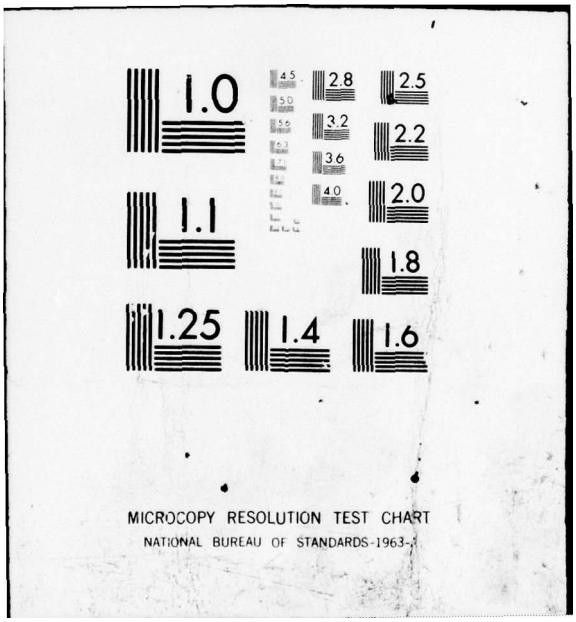
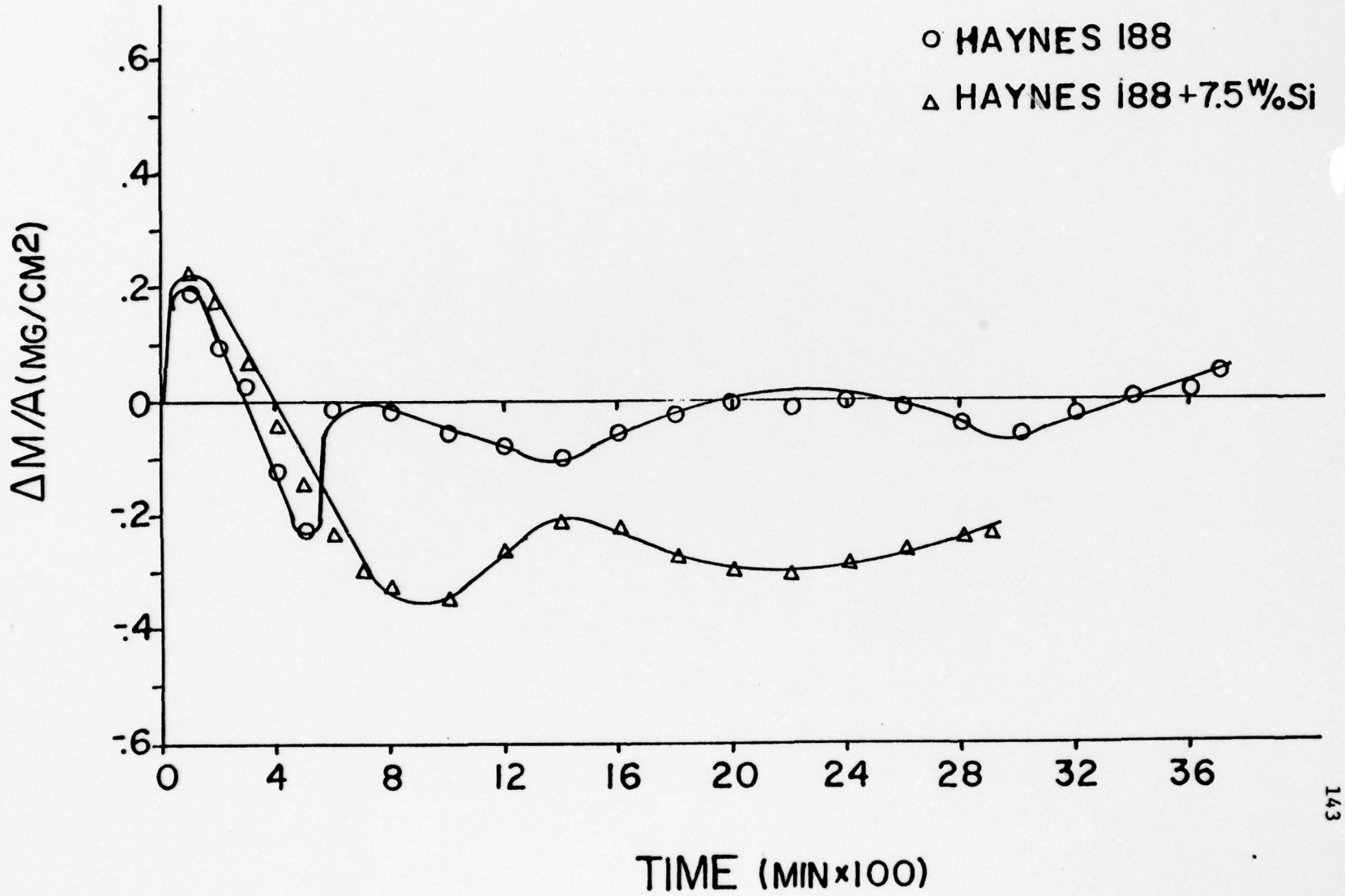
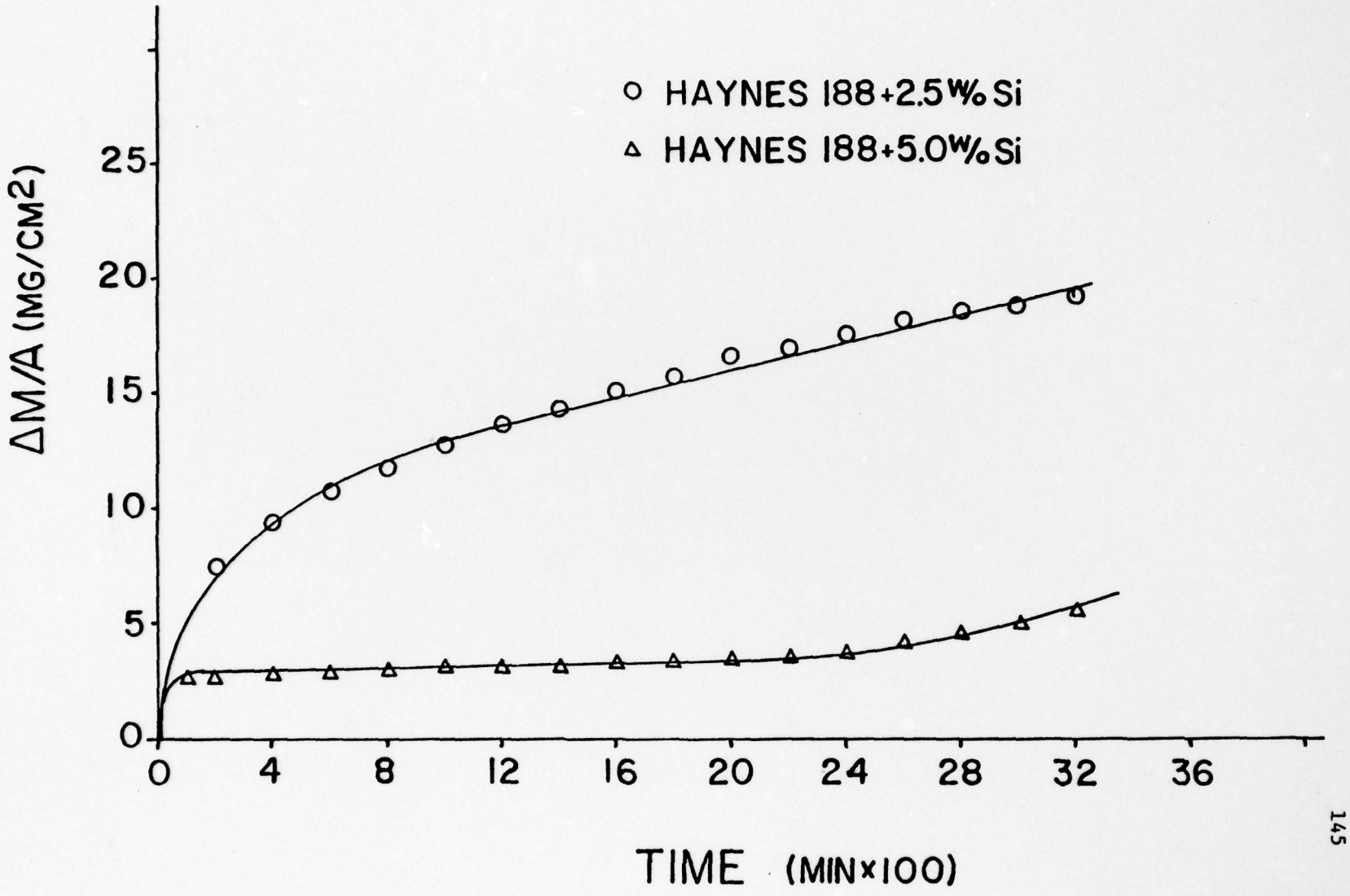

1.0
1.1
1.25
1.4
1.6
1.8
2.0
2.2
2.5
2.8
3.2
3.6
4.0
4.5
5.0
5.6
6.3
MICROCOPY RESOLUTION TEST CHART
NATIONAL BUREAU OF STANDARDS-1963-A

Figure 48. ($\Delta M/A$) versus time of hot corrosion of Haynes 188 and Haynes 188 + 7.5Si alloys.


o HAYNES 188
Δ HAYNES 188+7.5 W% Si
ΔM/A (MG/CM2)
.6
.4
.2
0
-.2
-.4
-.6
0
4
8
12
16
20
24
28
32
36
TIME (MIN×100)

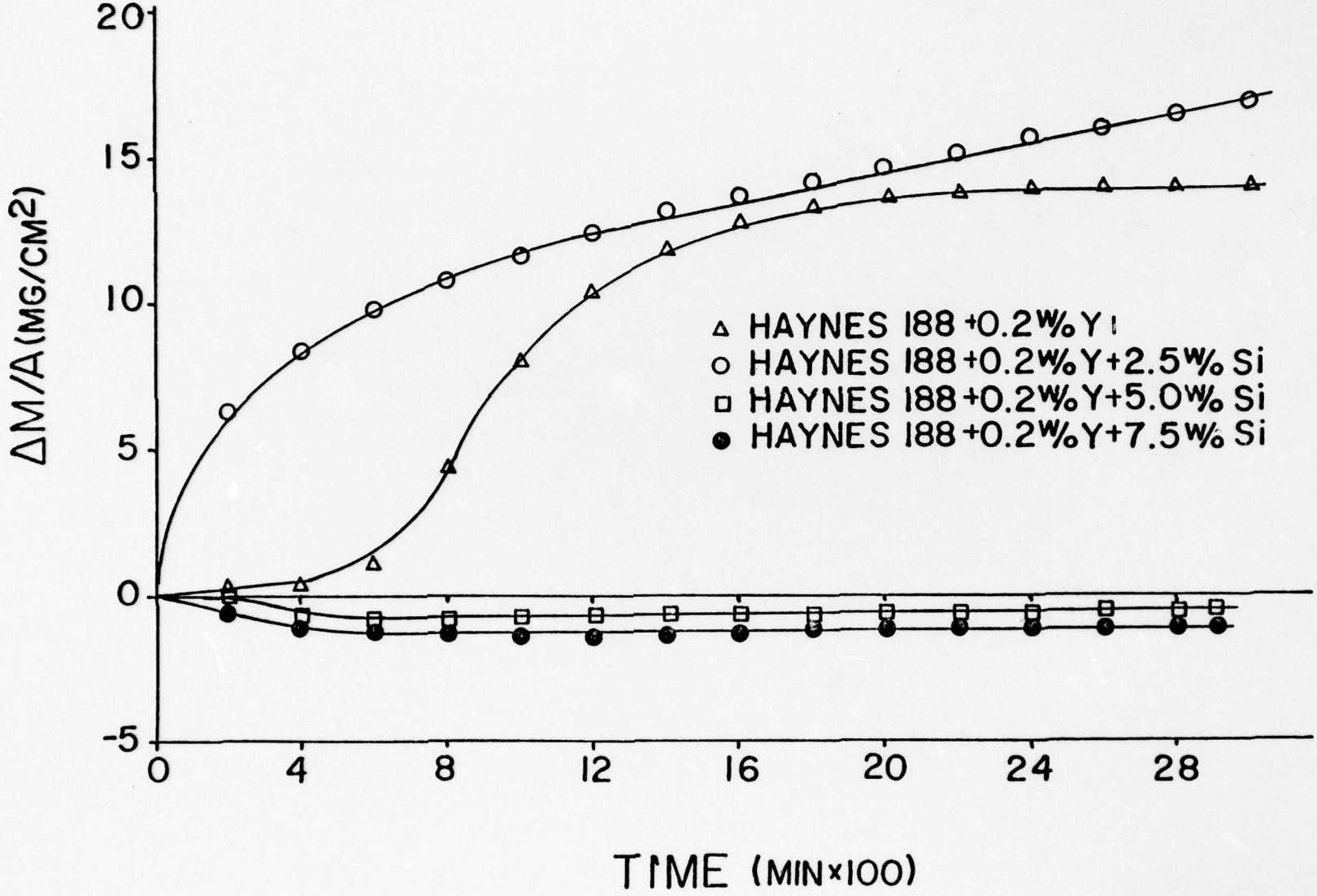
Blank

Figure 49. ($\Delta M/A$) versus time of hot corrosion of Haynes 188 + 2.5 Si alloy and of Haynes 188 + 5 Si alloy.


HAYNES 188+2.5W% Si
HAYNES 188+5.0W% Si
ΔM/A (MG/CM2)
0
5
10
15
20
25
0
4
8
12
16
20
24
28
32
36
TIME (MIN×100)

Blank

Figure 50. ($\Delta M/A$) versus time of hot corrosion of Haynes 188 + Si + 0.2Y set of alloys.


20
15
10
5
0
-5
0
4
8
12
16
20
24
28
ΔM/A (MG/CM2)
TIME (MIN×100)
△ HAYNES 188 +0.2W% Y
○ HAYNES 188 +0.2W% Y+2.5W% Si
□ HAYNES 188 +0.2W% Y+5.0W% Si
● HAYNES 188 +0.2W% Y+7.5W% Si

The scales formed on this series of alloys were multi-layered. The severely attacked samples (the 2.5 Si, 5 Si, the 0.2 Y and the 2.5 Si-0.2 Y alloys) developed thick outer layers which spalled upon cooling, revealing a very porous black inner layer. The scale formed on the 2.5 Si-0.2 Y alloy may be seen in Figure 51, and is typical of the scales formed on the severely corroded samples. X-ray analysis of these scales revealed $CoCr_2O_4$, $CoNiO_4$, and $CoWO_4$. The thick porous outer layer consisting of (Co, Ni)O (a solid solution of CoO and NiO) followed by an inner porous layer of the spinels $CoCr_2O_4$ and $CoWO_4$. Microprobe profiles showed low levels of manganese distributed evenly throughout the scales and an even distribution of silicon with some higher concentrations of silicon in the scale near the alloy/scale interface. Probe results also indicate the development of a protective Cr_2O_3 layer, however, Cr_2O_3 was not identified by x-ray diffraction analysis.

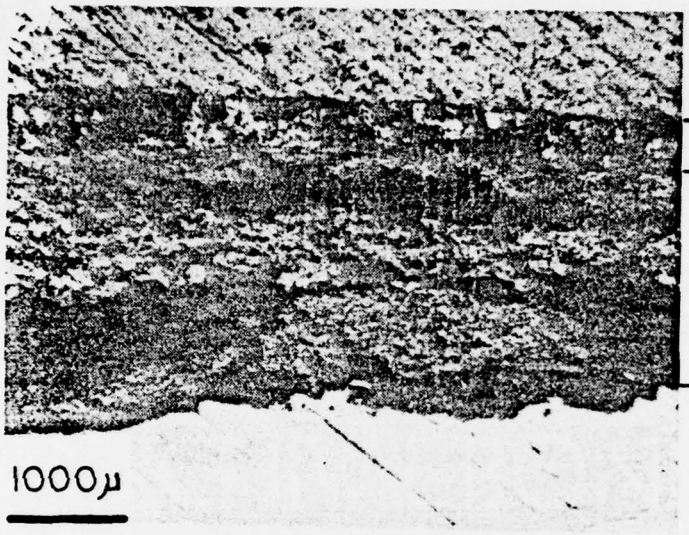
The scales formed on the samples which showed a negative value for the total weight gained/unit area, i.e., Haynes 188 unmodified, 7.5 Si modified alloy, the 5.0 Si-0.2 Y and the 7.5 Si-0.2 Y modified alloy, developed thin scales. These scales consisted of an outer black layer which spalled upon cooling and a better adhered inner grayish layer. The exception is the unmodified Haynes 188 alloy which developed a very compact and well adhered scale, see Figure 52. X-ray analysis identified $CoCr_2O_4$, CoO-NiO, and $CoWO_4$ as the components of these scales. $CoSiO_4$ was identified in the 5.0 Si-0.2 Y modified alloy.

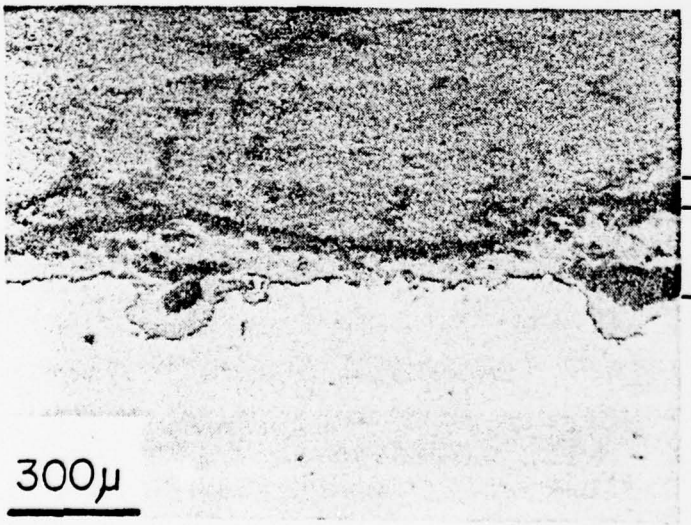
Microprobe profiles of the unmodified Haynes 188 alloy indicated the possible formation of a Cr_2O_3 layer at the alloy scale interface.

Blank

Figure 51. Photomicrograph of the cross-section of the scale formed on Haynes 188 + 2.5Si + 0.2Y alloy after hot corrosion.

Figure 52. Photomicrograph of the cross-section of the scale formed on Haynes 188 alloy after hot corrosion.


CoO+CoNiO2
CoCr2O4+CoWO4
+VOIDS
ALLOY
1000μ


CoO+CoNiO2
CoCr2O4+CoWO4
ALLOY
300μ

An even distribution of Mn and Ni was revealed. The profiles of the 7.5 Si alloy showed a high concentration of tungsten at the alloy/scale interface. Chromium concentrations were high and evenly distributed throughout the scale. The silicon concentration was enriched at the alloy/scale interface. Similar results were found for the 7.5 Si-0.2 Y alloy with the exception that the chromium concentration was much lower than in the scale formed on the 7.5 Si alloy. No evidence of sodium or sulfur was found in the scales or in the alloys.

D. Haynes 157 Series

1. Oxidation

The third commercial alloy studies in this investigation is Haynes 157. This base material differs significantly from the other superalloys used in this study. Firstly, it contains a higher silicon concentration (1.6 wt % Si) than most other superalloys. Other differences include a relatively low tungsten concentration (4.5 wt %) and abnormally high boron concentrations. Table 5 lists the nominal alloy composition along with the results from the thermogravimetric studies of the oxidation and of the hot corrosion silicon and silicon-yttrium modified Haynes 157 alloys.

Figure 53 shows the weight gain per unit area versus time plots of the oxidation of the Haynes 157 alloys modified only with silicon. These alloys oxidized parabolically and the parabolic oxidation rates decreased with increased silicon concentrations in the alloys.

Table 5

Parabolic-Rate Constant Data for Haynes 157 Series

Cr	C	Si	B	W
21	0.07	1.6	2.4	4.5

Alloying Modifications	Oxidation		Hot Corrosion	
	$Kp \times 10^{11}$ ($gm^2 cm^{-4} sec^{-1}$)	$\frac{\Delta m}{A}$* (mg)	$Kr \times 10^{11}$ ($gm^2 cm^{-4} sec^{-1}$)	$\frac{\Delta m}{A}$** (mg)
None	5.23	3.11***	13.00	7.31
2.5% Si	1.87	2.44****	9.12	4.41
5% Si	0.25	0.79	5.14	4.09
10% Si	0.16	0.69	2.71	7.89
2% Y	0.39	0.63 (.80 max)	17.60	8.24*****
2.5% Si + 0.2% Y	0.10	0.313 (.41 max)	3.54	3.44
5% Si + 0.2% Y	0.44	1.29	10.00	5.80
7.5% Si + 0.2% Y	0.13	0.52	4.03	6.92******

*Standard Test Duration 4200 min.

**Standard Test Duration 2900 min.

***Test Duration 2200 min.

****Test Duration 2300 min.

*****Test Duration 2600 min.

******Test Duration 2400 min.

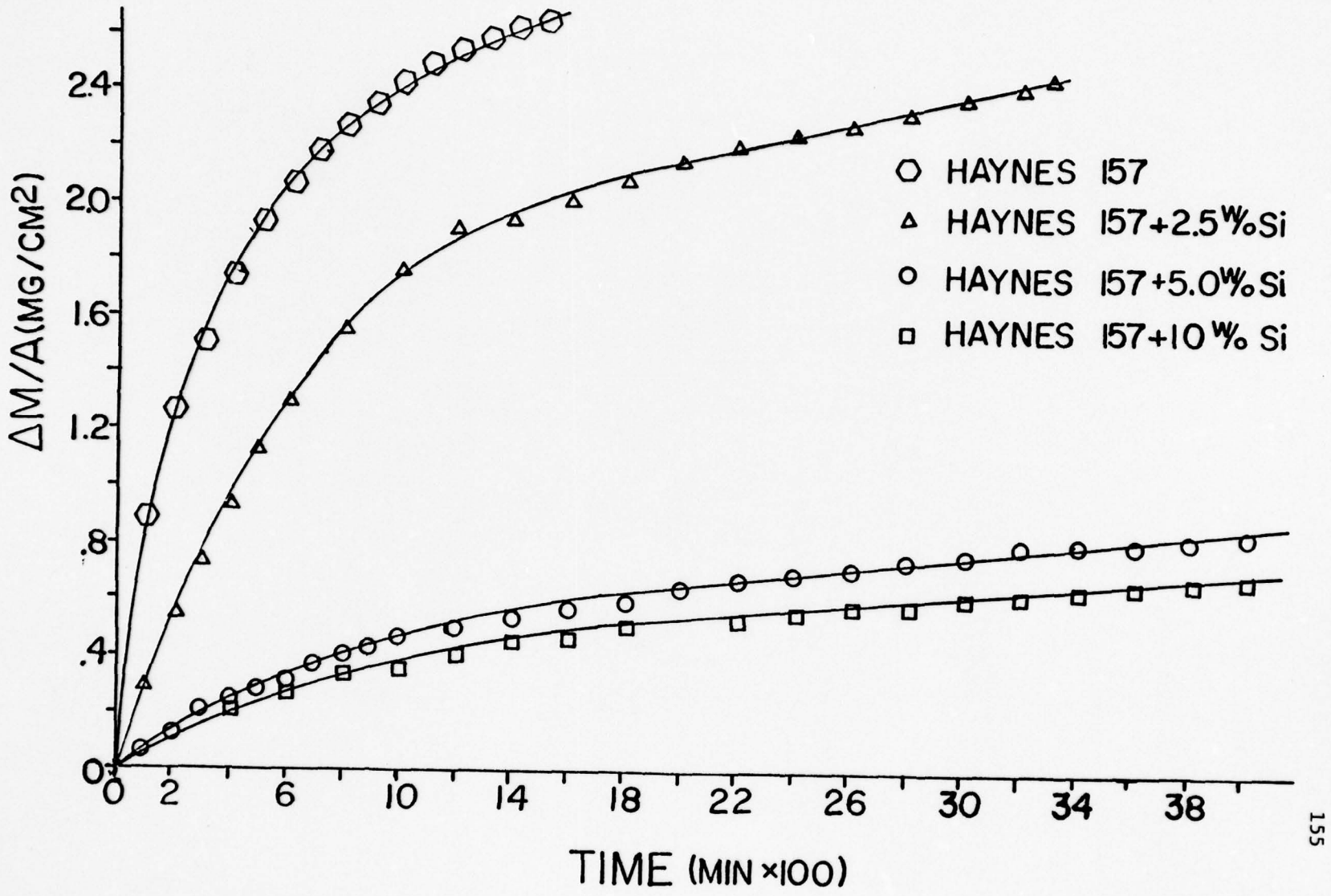
The alloys which were modified with silicon and 0.2 wt % yttrium showed an unusual behavior. The base alloy containing 1.6 wt % Si + 0.2 Y (modification) and the alloy whose silicon concentration was raised to 2.5 wt % by additions of silicon, showed a weight decrease following the initial weight gain, see Figure 54. It should be noted that the oxidation resistance of this alloy set was very good and was comparable to the other superalloys investigated in this study.

Metallographic examinations of the scales formed on these alloys indicated a single relatively thick oxide layer. The oxide layer formed on the base alloy (unmodified), the 2.5% Si alloys and the 5 wt % Si alloys had the appearance of having solidified from a liquid phase existing at 1000°C, the oxidation temperature. It was light green in color. The 7.5 wt % Si alloy did not appear as such. Typical photomicrographs of the unmodified Haynes 157 alloy and a 2.5 Si-0.2 Y modified alloy are shown in Figures 55 and 56. The metal/oxide interface is very smooth. The unmodified Haynes 157 alloy grew a much more compact oxide scale and was internally oxidized while the 2.5 Si-0.2 Y alloy was not internally oxidized and grew a thinner, finer, grained oxide scale.

X-ray analysis of the scales formed on these alloys identified the presence of B_2O_3, $CrBO_3$, and Cr_2O_3. The 5% Si alloys contained $CoCr_2O_4$ along with B_2O_3, $CrBO_3$, and Cr_2O_3. The scale formed on the 10 wt % Si modified alloy contained only Cr_2O_3 and metallic cobalt. This may be attributed to the initial formation of a SiO_2 layer which may have lowered the P_{O_2} gradient present in the oxide layer to a

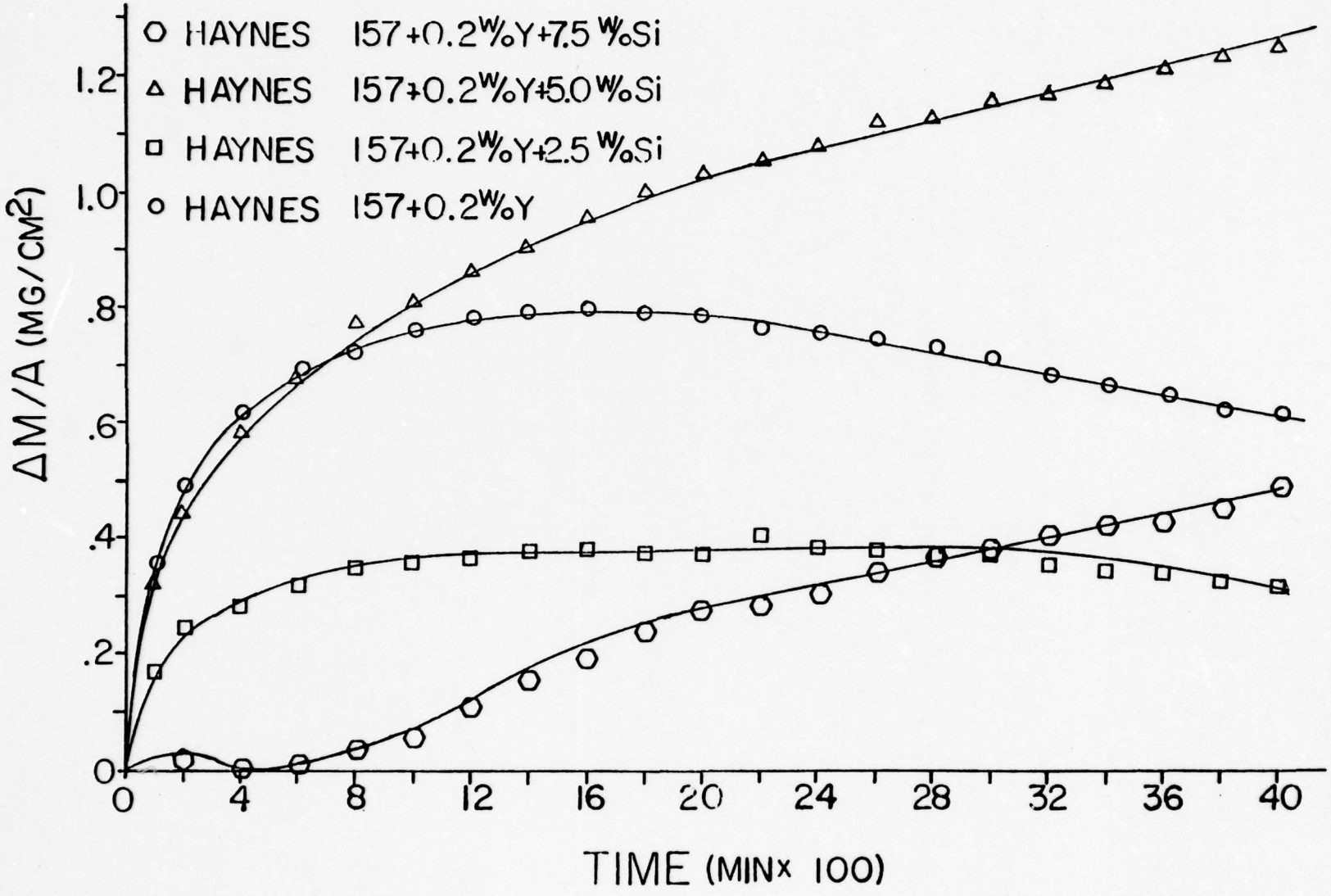
Blank

Figure 53. (ΔM/A) versus time of oxidation of Haynes 157 + Si set of alloys.


ΔM/A(MG/CM2)
2.4
2.0
1.6
1.2
.8
.4
0
0
2
6
10
14
18
22
26
30
34
38
TIME (MIN ×100)
HAYNES 157
HAYNES 157+2.5 W% Si
HAYNES 157+5.0 W% Si
HAYNES 157+10 W% Si

Blank

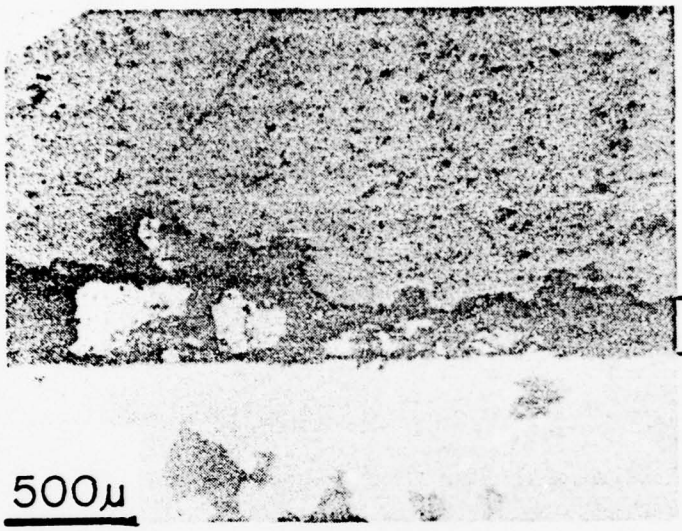
Figure 54. (ΔM/A) versus time of oxidation of Haynes 157 + Si + 0.2Y set of alloys.

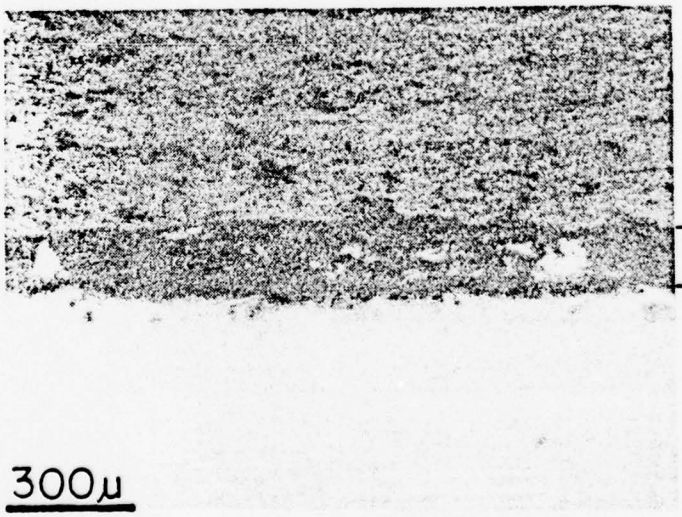

HAYNES 157+0.2W/oY+7.5 W/oSi
HAYNES 157+0.2W/oY+5.0W/oSi
HAYNES 157+0.2W/oY+2.5 W/oSi
HAYNES 157+0.2W/oY
ΔM/A (MG/CM2)
0
.2
.4
.6
.8
1.0
1.2
0
4
8
12
16
20
24
28
32
36
40
TIME (MINx 100)

Blank

Figure 55. Photomicrograph of the cross-section of the scale formed on Haynes 157 alloy after oxidation.

Figure 56. Photomicrograph of the cross-section of the scale formed on Haynes 157 + 2.5Si + 0.2Y alloy after oxidation.


$Cr_2O_3+CrBO_3+B_2O_3$
ALLOY
500μ


$Cr_2O_3+CrBO_3+B_2O_3$
ALLOY
300μ

value below the P_{O_2} necessary for cobalt oxidation. However no silicates were found by x-ray diffraction studies.

Microprobe analysis was performed on several selected samples. In general high chromium concentrations were found throughout the oxide scales. Silicon concentrations were high near the metal/oxide interface for the base alloy Haynes 157 unmodified. A similar scale was formed on the Haynes 157 + 0.2 Y alloy, with the exception that the silicon concentration was virtually undetectable in the oxide. Figures 57 and 58 are the probe profiles for the scales formed on the Haynes 157 alloy and the Haynes 157-7.5 Si-0.2 Y alloy, respectively. The formation of silicates or SiO_2 within the oxide scales is probably responsible for the decrease in the oxidation rate as a function of increased silicon concentration in the alloy. However x-ray studies failed to identify any silicates. The weight decrease observed during the oxidation of the low silicon (1.6 and 2.5 Si) alloys may be attributed to the possible failure of these alloys to form an SiO_2 or silicate layer. B_2O_3 which has a vapor pressure at 1000°C of about 10^{-3} to 10^{-4} mm Hg (79), may be diffusing out rapidly, aided by the finer grained oxide formed on the yttrium modified alloys, facilitating ionic transport via grain boundaries. It should be noted again that chemical analysis failed to show any yttrium concentration greater than 0.01 wt % Y.

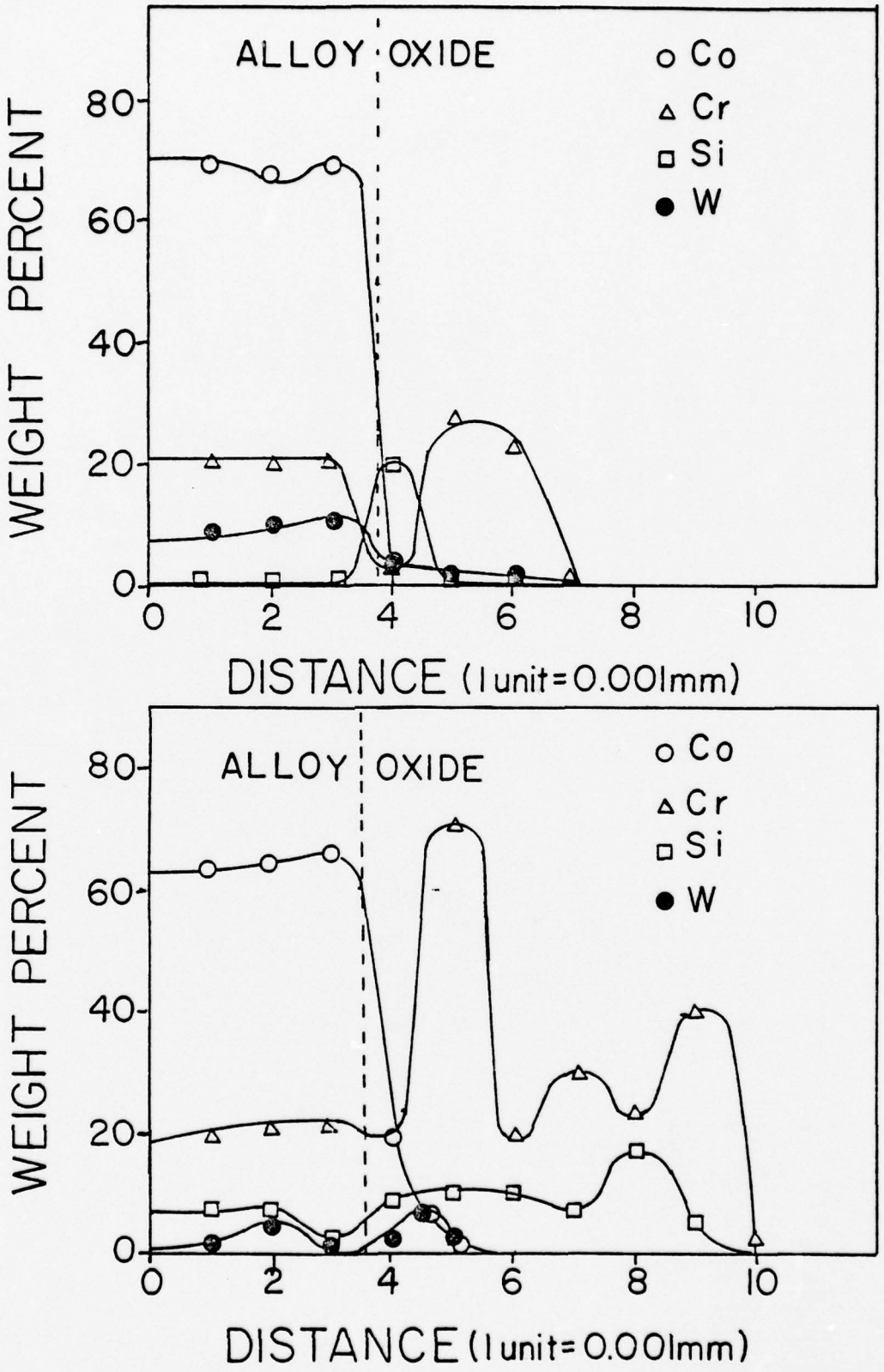
2. Hot Corrosion

The hot corrosion of the Haynes 157 series of alloys resulted in a somewhat accelerated attack than under a purely

Blank

Figure 57. Microprobe profile of Haynes 157 alloy after oxidation.

Figure 58. Microprobe profile of Haynes 157 + 7.5Si + 0.2Y alloy after oxidation.


ALLOY
OXIDE
Co
Cr
Si
W
WEIGHT PERCENT
80
60
40
20
0
0
2
4
6
8
10
DISTANCE (1 unit = 0.001mm)
ALLOY
OXIDE
Co
Cr
Si
W
WEIGHT PERCENT
80
60
40
20
0
0
2
4
6
8
10
DISTANCE (1 unit = 0.001mm)

oxidizing environment. Table 5 lists the hot corrosion rate and the total weight gain per unit area data for this series of alloys. The results of the thermogravimetric studies are given in Figures 59 and 60. These alloys did not show a significant weight loss following the initial accelerated weight gains. The alloys modified only with increased silicon concentrations showed a constant decrease in the calculated reaction rates from 13.0×10^{-11} gm^2 cm^{-4} sec^{-1} for the unmodified Haynes 157 alloy to 2.71×10^{-11} gm^2 cm^{-4} sec^{-1} for the 10% Si modified alloy. In general the total weight gain data showed the same trend with the exception being the 10% Si alloy which showed a much greater initial weight gain than the other alloys in this set.

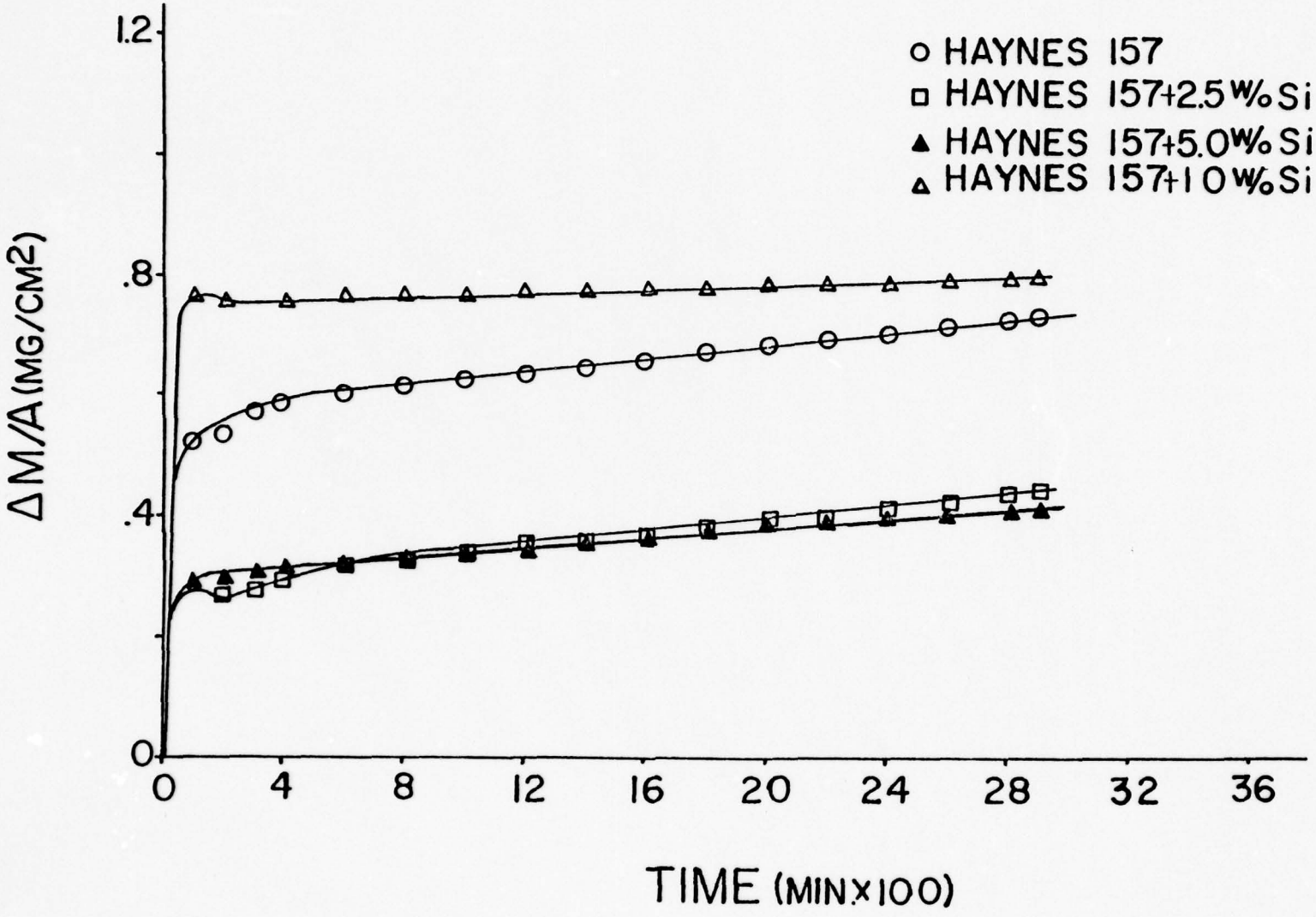
The "yttrium containing set" was much poorer behaved; however, the same trend is indicated. The 5% Si-0.2 Y and the 7.5% Si-0.2 Y alloy showed higher reaction rates and total weight gains per unit area. Again there was no significant weight losses following the initial period of weight gains.

The scales formed on this series of alloys were very well adhered. The outer scale was grayish black in appearance and not the light green oxide which formed during oxidation. Figure 61 shows a representative cross section of these scales. The scale appears very porous which may account for the much greater weight gains of the series of alloys.

Attempts to analyze the x-ray diffraction patterns from the scales formed on this series of alloys was very difficult, and as a result many diffraction lines could not be accounted for. Some compounds that were identified are Co_2SiO_4, $CrBO_3$, W_3O, $CrCr_2O_4$, and

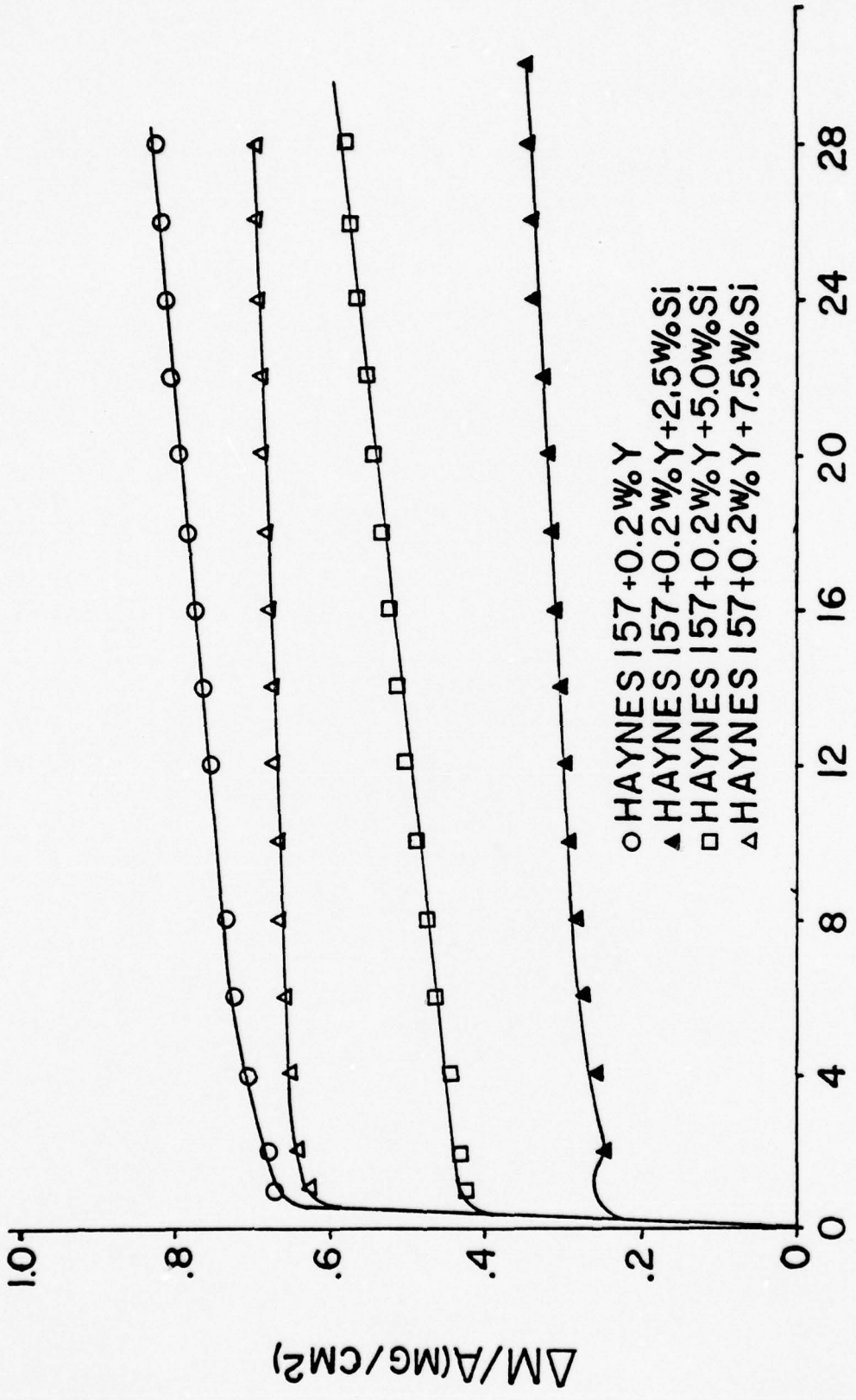
Blank

Figure 59. (ΔM/A) versus time of hot corrosion of Haynes 157 + Si set of alloys.


o HAYNES 157
□ HAYNES 157+2.5 W% Si
▲ HAYNES 157+5.0 W% Si
△ HAYNES 157+10 W% Si
ΔM/A (MG/CM2)
1.2
.8
.4
0
0
4
8
12
16
20
24
28
32
36
TIME (MIN X 100)

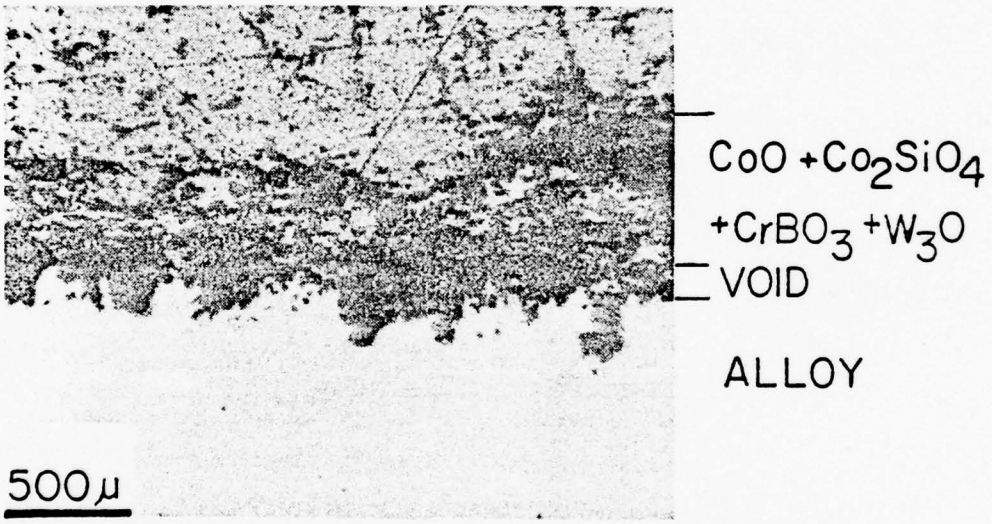
Blank

Figure 60. (ΔM/A) versus time of hot corrosion of Haynes 157 + Si + 0.2Y set of alloys.


ΔM/A(MG/CM2)
1.0
.8
.6
.4
.2
0
0
4
8
12
16
20
24
28
TIME(MINX100)
○HAYNES 157+0.2W% Y
▲HAYNES 157+0.2W% Y+2.5W%Si
□HAYNES 157+0.2W% Y+5.0W%Si
△HAYNES 157+0.2W% Y+7.5W%Si

Blank

Figure 61. Photomicrograph of the cross-section of the scale formed on Haynes 157 alloy after hot corrosion.


CoO + Co_2SiO_4
+ $CrBO_3$ + W_3O
VOID
ALLOY
500μ

CoO. Elemental cobalt and boron were identified in the high silicon alloys. These compounds are not the only compounds formed.

The results from the microprobe analysis were much more complete. The low silicon alloys such as the unmodified Haynes 157 alloy, and the 2.5%-0.2 Y alloy showed very high concentrations of silicon throughout the scale. Chromium concentrations were spread throughout the scale. There was no evidence of the formation of a Cr_2O_3 protective layer. Tungsten concentrations were low or non-existant in the scales formed. Boron could not be profiled due to problems within the instrument.

The results of the scale analysis do not appear to shed any light on the subject of explanations for the behavior of this series of alloys. A much more in depth analysis should be undertaken.

E. Mar-M302 Series

1. Oxidation

The final commercial alloy utilized in this investigation is Mar-M302. The alloy was modified with silicon and yttrium similarly to the other commercial alloys studied. These modifiecations, the base alloy composition, along with the results from thermogravimetric studies are given in Table 6. Figure 62 shows the weight gain per unit area as a function of time oxidized. These alloys followed the parabolic oxidation kinetics. The oxidation rates were low (1.8×10^{-11} $gm^2\ cm^{-4}\ sec^{-1}$) for the unmodified Mar M-M302 alloy, and decreased to 0.24×10^{-11} $gm^2\ cm^{-4}\ sec^{-1}$, for the 7.5 wt % Si alloy. In general there was a decrease in the oxidation rate as a function of increased

Table 6

Parabolic-Rate Constant Data for Mar-M302 Series

$\frac{Cr}{21.5}$ $\frac{C}{.85}$ $\frac{W}{10}$ $\frac{B}{.005}$ $\frac{Zr}{.2}$ $\frac{Ta}{9.0}$

Alloying Modifications	Oxidation		Hot Corrosion	
	$Kpx10^{11}$ $(gm^2cm^{-4}sec^{-1})$	$\frac{\Delta m}{A}$* (mg)	$Krx10^{11}$ $(gm^2cm^{-4}sec^{-1})$	$\frac{\Delta m}{A}$** (gm)
None	1.08	1.34***	---	0.14
2.5% Si	0.45	1.04	---	0.19
5% Si	0.65	1.45	---	-1.17
7.5% Si	0.24	0.73****	---	0.14
0.2% Y	0.31	0.66****	---	-0.32
2.5% Si + 0.2% Y	0.14	0.61	---	-1.59
5% Si + 0.2% Y	0.51	1.24	---	0.25
7.5% Si + 0.2% Y	1.31	1.11	6.02	3.15

*Standard Test Duration 4200 min.

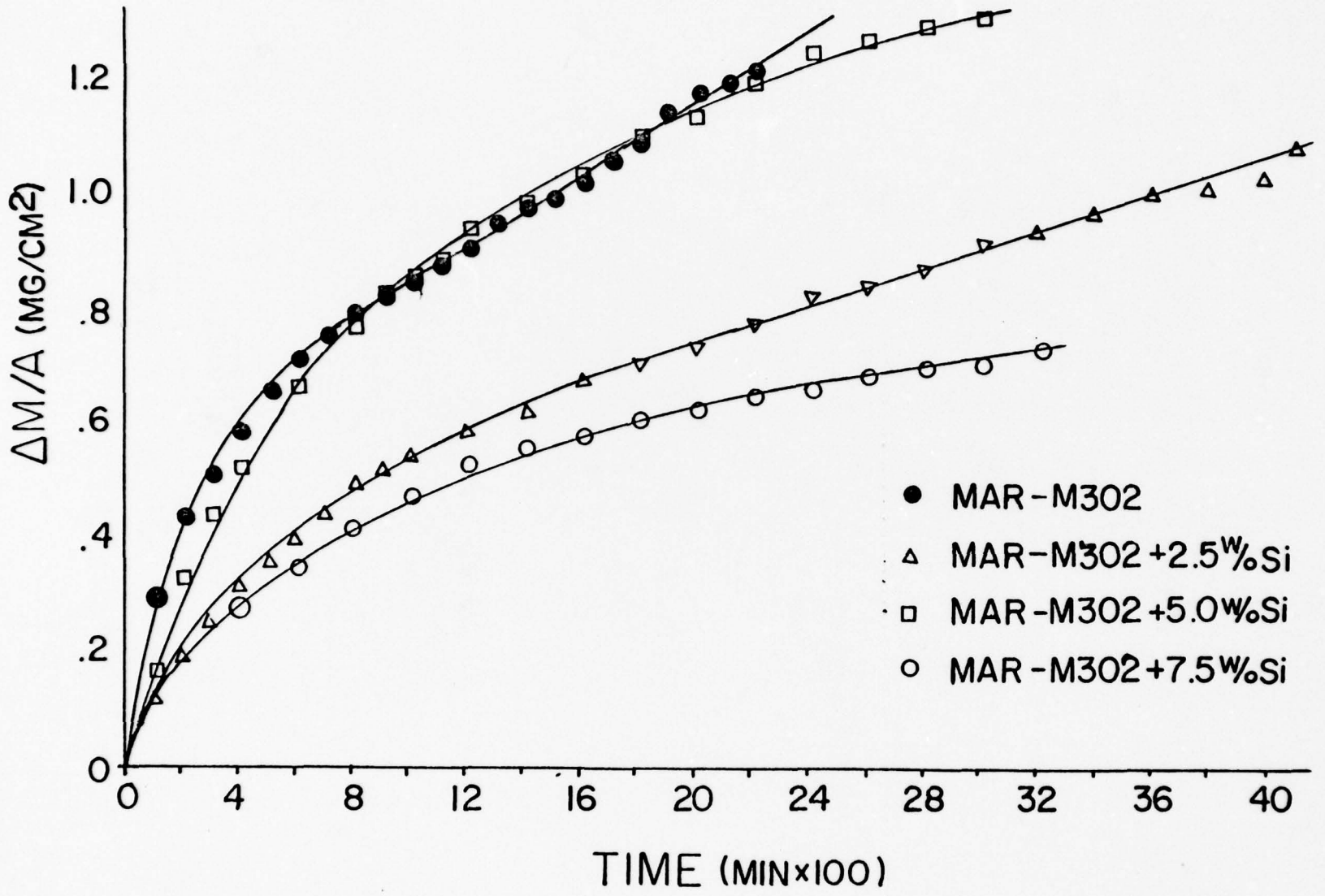
**Standard Test Duration 2900 min.

***Test Duration 3000 min.

****Test Duration 3200 min.

Blank

Figure 62. ($\Delta M/A$) versus time of oxidation of Mar-M302 + Si set of alloys.


ΔM/A (MG/CM2)
1.2
1.0
.8
.6
.4
.2
0
0
4
8
12
16
20
24
28
32
36
40
TIME (MIN×100)
MAR-M302
MAR-M302+2.5W%Si
MAR-M302+5.0W%Si
MAR-M302+7.5W%Si

silicon concentration. The exception is the 5 wt % Si alloy whose oxidation rate was slightly greater than the oxidation rate of the 2.5 wt % Si alloy, and whose total weight gain is similar to that of the unmodified Mar-M302 alloy.

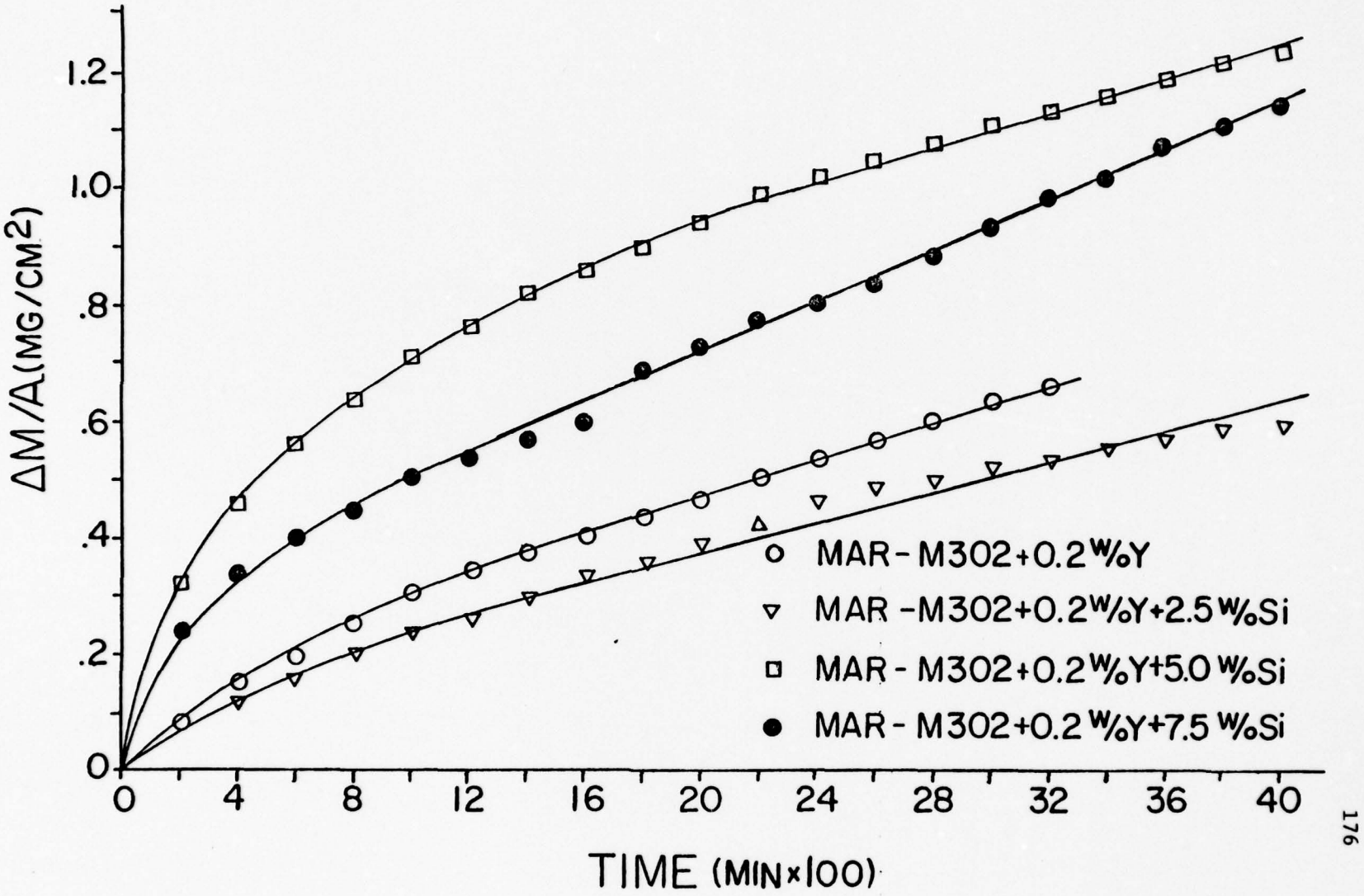
The oxidation of the Si-Y modified alloys is shown in Figure 63. The kinetic data is presented in Table 6. In general these alloys showed an increase in the oxidation rate as a function of increased silicon content. The exception in the Si and Y modified alloy set is the 2.5 Si-0.2 Y alloy which showed the lowest oxidation rate (0.14×10^{-11} gm^2 cm^{-4} sec^{-1}) in the series of Mar-M302 based alloys.

Metallographic examination of the oxides formed on the Mar-M302 series of alloys showed the formation of very thin oxide scales. Again they were double layered. The outer oxide identified by x-ray diffraction techniques was CoO, which spalled off upon cooling to room temperature. This spalling of the outer oxide occurred on all the alloys oxidized in this investigation. The inner layers were composed of $CoCr_2O_4$, Cr_2O_3, $CoTa_2O_6$ and $CrTaO_4$. The 7.5 Si-0.2 Y alloy did not form $CoCr_2O_4$, but instead formed Ta_2O_5 along with the other compounds mentioned. Co_2SiO_4 was not found in the scales formed on this series of alloys.

Microprobe analysis of the scales formed on these alloys indicates that the oxidation resistance of this set of alloys is due primarily to a dense inner layer of the spinels, $CoCr_2O_4$, Cr_2O_3, $CoTa_2O_6$ and $CrTaO_4$. Microprobe analysis did show the presence of silicon and tungsten in the scales, although no silicates or tungsten oxides were identified in the x-ray studies.

Blank

Figure 63. ($\Delta M/A$) versus time of oxidation of Mar-M302 + Si + 0.2Y set of alloys.


ΔM/A(MG/CM2)
1.2
1.0
.8
.6
.4
.2
0
0
4
8
12
16
20
24
28
32
36
40
TIME (MIN×100)
MAR-M302+0.2W/oY
MAR-M302+0.2W/oY+2.5W/oSi
MAR-M302+0.2W/oY+5.0W/oSi
MAR-M302+0.2W/oY+7.5W/oSi

The slightly atypical behavior of certain alloys in this series is difficult to explain on the basis of the scale analysis. The 2.5 wt % Si alloy, which had an abnormally low rate compared to that of the pure Mar-M302 alloy and the 5 wt % Si modified alloy, was shown by the microprobe as having a very dense spinel concentrated inner layer. The thickness of this inner layer was 0.01 mm. The atypical behavior of the yttrium containing alloys cannot be explained and a much more indepth microprobe analysis would be required.

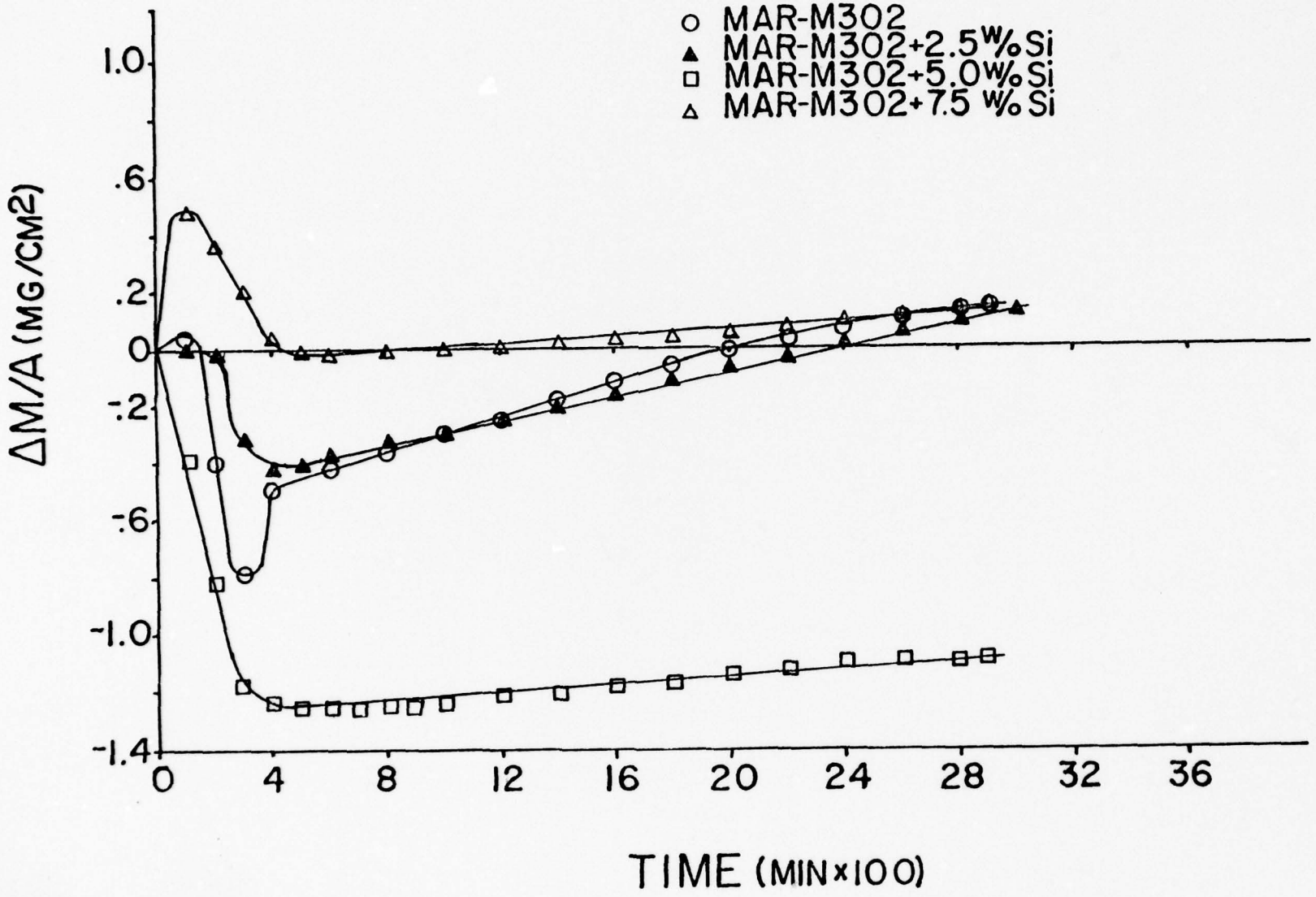
2. Hot Corrosion

The hot corrosion of Mar-M302 alloys modified with silicon may be seen in Figures 64 and 65. Table 6 lists the total weight gain per unit area data for the Mar-M302 series of alloys. The hot corrosion behavior is similar to the G.E. X-40 series and the Haynes 188 series of alloys, in that the alloys showed a rapid weight loss following the initial weight gain. The 5% Si alloy failed to show an initial weight gain, but instead showed a very large weight loss, over 1.2 mg cm^{-2}.

The set of alloys modified with 0.2 Y along with the standard silicon modifications showed different behaviors than the group modified only with silicon. In this set the largest weight loss occurred with the 2.5% Si-0.2% Y. The 10% Si-0.2% Y alloy showed no weight loss and more closely approached parabolic behavior than any other alloy in this series. The 5% Si-0.2% Y alloy started loosing weight after 1000 minutes and continued to loose weight through the duration of the test. No general trends could be observed concerning

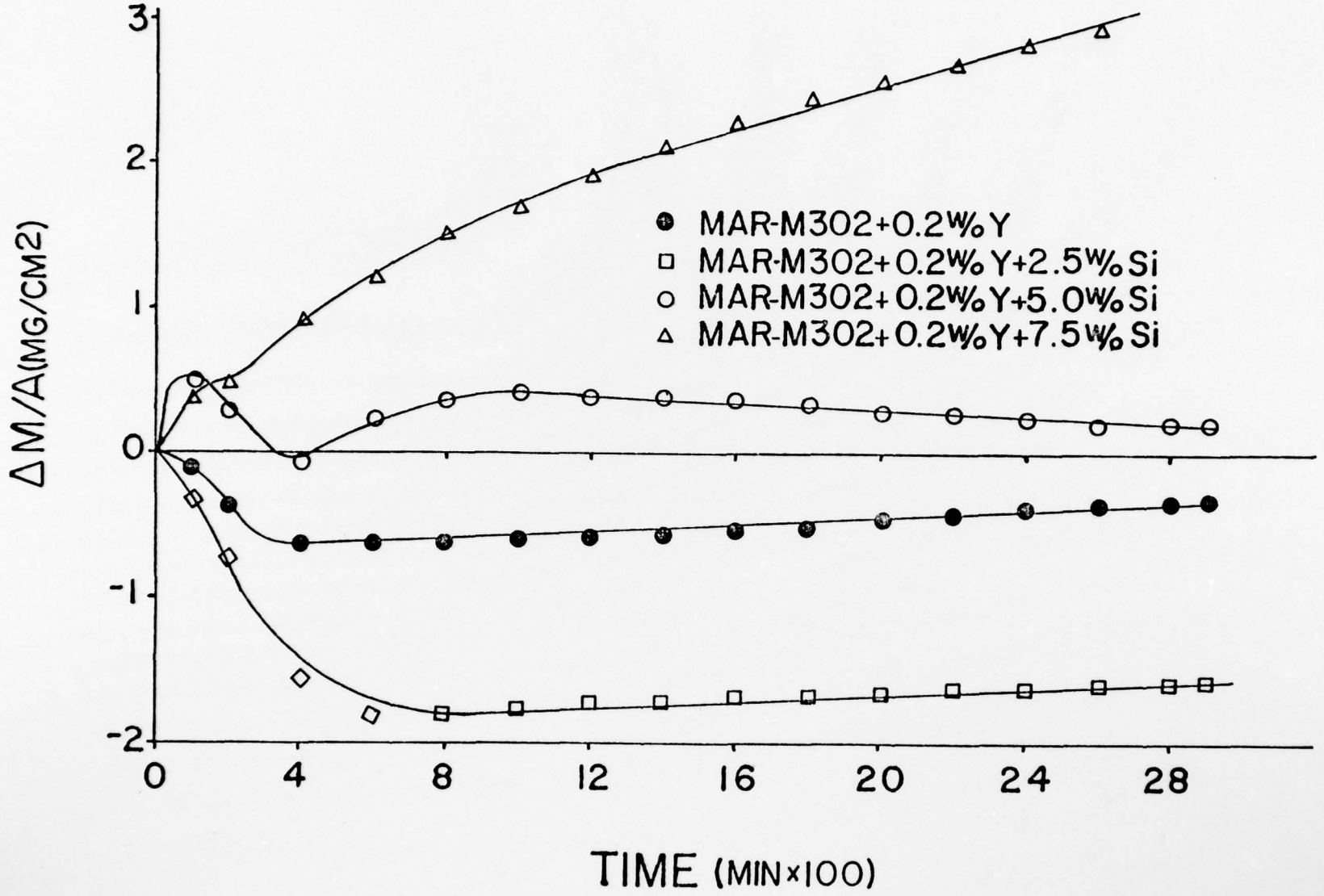
Blank

Figure 64. ($\Delta M/A$) versus time of hot corrosion of Mar-M302 + Si set of alloys.


MAR-M302
MAR-M302+2.5 W/o Si
MAR-M302+5.0 W/o Si
MAR-M302+7.5 W/o Si
ΔM/A (MG/CM2)
1.0
.6
.2
0
-.2
-.6
-1.0
-1.4
0
4
8
12
16
20
24
28
32
36
TIME (MIN×100)

Blank

Figure 65. ($\Delta M/A$) versus time of hot corrosion of Mar-M302 + Si + 0.2Y set of alloys.


MAR-M302+0.2W% Y
MAR-M302+0.2W% Y+2.5W% Si
MAR-M302+0.2W% Y+5.0W% Si
MAR-M302+0.2W% Y+7.5W% Si
ΔM/A(MG/CM2)
TIME (MIN×100)
3
2
1
0
-1
-2
0
4
8
12
16
20
24
28

the effects of increased silicon concentrations on the hot corrosion behavior. No alloy appeared to have excessively oxidized in the hot corrosion environment.

The scales formed on these alloys were well adhered with the exception of the 7.5 Si alloys. The scales were double layered with a black "crusty" outer layer and a compact greenish gray inner layer. The scales formed on the unmodified Mar-M302 alloy were very porous which may account for the large weight gain noted after the period of weight loss. The alloy/scale interface was rough as compared with the interface formed during oxidation.

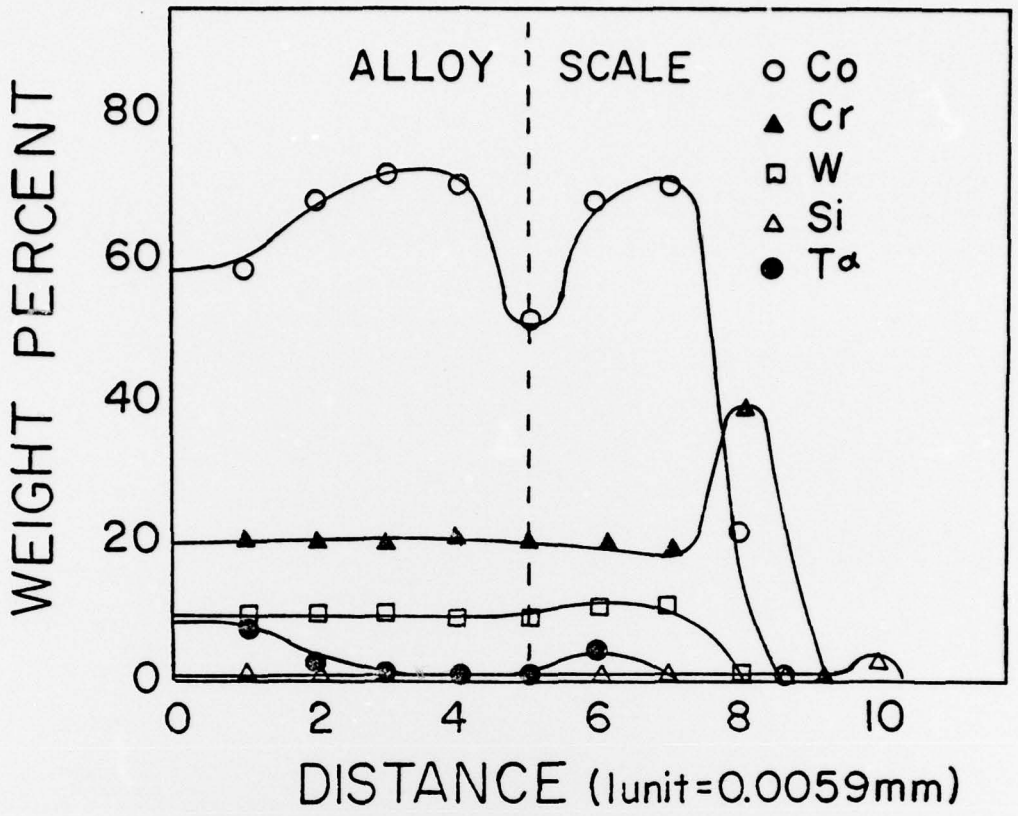
X-ray analysis of selected samples showed the formation of $CoCr_2O_4$, $CrTaO_4$ and elemental Co. Additionally some Cr_2O_3 and Ta_2O_5 were identified in the scales formed on the 5% Si and 7.5% Si alloys.

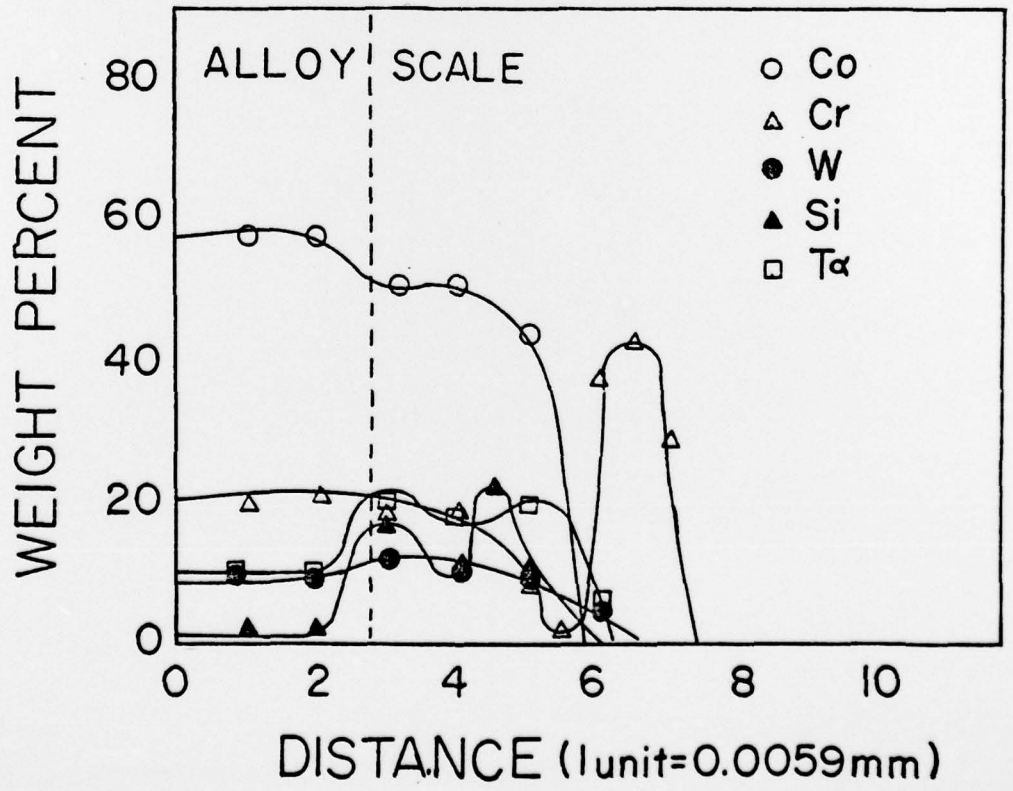
Microprobe analysis on the Mar-M302 + 0.2 Y alloy, the 2.5% Si alloy, and the 5% Si alloy, showed the formation of a protective Cr_2O_3 layer in the scale. This may account for the absence of the initial weight gain period noted for other alloys investigated. X-ray analysis of the scales formed on the 5% Si alloy did identify Cr_2O_3. Figures 66 and 67 are the microprobe profiles of the 2.5% Si and 5% Si, respectively. The 5% Si + 0.2% Y alloy which showed a continuous weight loss during hot corrosion was shown to have a very high tungsten concentration near the gas/scale interface. Volatile tungsten oxides, such as WO_3 may be responsible for the steady weight loss of this alloy during hot corrosion. X-ray analysis failed to identify any tungsten oxides. Silicon concentrations were found to be highly concentrated at the alloy/scale interface for the 5% Si

Blank

Figure 66. Microprobe profile of Mar-M302 + 2.5Si alloy after hot corrosion.

Figure 67. Microprobe profile of Mar-M302 + 5Si alloy after hot corrosion.


ALLOY
SCALE
Co
Cr
W
Si
Tα
WEIGHT PERCENT
80
60
40
20
0
0
2
4
6
8
10
DISTANCE (1unit=0.0059mm)


ALLOY
SCALE
Co
Cr
W
Si
Tα
WEIGHT PERCENT
80
60
40
20
0
0
2
4
6
8
10
DISTANCE (1unit=0.0059mm)

alloys. Tantalum concentrations also showed this same behavior but not in all the alloys. Tungsten concentrations remained constant in the alloy and throughout the scale with the exception of the 5% Si + 0.2% Y alloy as noted previously. The effects of increased silicon concentrations may be hidden by the already high concentration of high oxygen affinity elements such as tantalum and tungsten.

VI. SUMMARY AND CONCLUSIONS

The rates of oxidation and hot corrosion of cobalt-chromium-silicon-yttrium alloys and the four commercial alloys modified with silicon and silicon-yttrium were determined at 1000°C in oxygen at a pressure of 0.1 atmosphere. The hot corrosion studies were conducted by coating the samples with 1 mg/cm^2 Na_2SO_4 prior to oxidation. Yttrium was added to evaluate its effects on scale adhesion.

Generally, the cobalt-chromium-silicon-yttrium alloys exhibited parabolic oxidation in both oxidizing and hot corroding environments. The lowest rates were obtained for alloys with high silicon concentrations. One alloy in particular, Co-20 Cr-10 Si-0.2 Y exhibited the lowest reaction rate for hot corrosion.

The effects of yttrium on the adherence of the scales formed on Co-Cr-Si alloys could not be ascertained due to the low concentrations (ppm) of yttrium present in the alloys. It should be noted that the scales formed on the high silicon alloys (5 wt % or greater) were more susceptible to spalling during cooling to room temperature.

The commercial alloys investigated in this study oxidized parabolically and the oxidation rate constants decreased as a function of increased silicon content. The Haynes 188 series is the exception since reaction rates increased as a function of increased silicon content. The hot corrosion of the commercial alloys was not parabolic, however it appeared that increased silicon concentrations did increase the resistance to hot corrosion. The complexity of the commercial alloys makes an exact appraisal of the effects of silicon difficult.

The conclusions drawn from the present study are:

a. The mechanism governing the oxidation of cobalt-based alloys at 1000°C and a partial pressure of oxygen at 0.1 atmosphere is the solid state diffusion of Co cations in a CoO matrix via a vacancy mechanism.

b. The diffusion is influenced by the formation of spinels such as $CoCr_2O_4$, Co_2SiO_4, and $CoWO_4$, which inhibit the solid state diffusion of cobalt ions by a blocking effect.

c. The formation of an SiO_2 protective layer during the early stages of oxidation and hot corrosion of the high silicon alloys may be responsible for the "immunity" of high silicon containing alloys to the fluxing action of Na_2SO_4 during the early stages of hot corrosion.

VII. SUGGESTIONS FOR FUTURE RESEARCH

Although the present study has elucidated a number of aspects concerning the oxidation and hot corrosion of cobalt based alloys, there are some aspects which require further investigation.

The scale formation as a function of time should be studied to determine if and when a layer of SiO_2 develops on the alloy surface after oxidation and hot corrosion. Further studies related to the stability of an SiO_2 protective layer should be made to elucidate how to promote and maintain an SiO_2 protective layer.

Further studies utilizing the scanning electron microscope at high magnification to study the thin film oxides formed on alloys with high chromium and silicon concentrations should be undertaken. The effect of elements such as yttrium on improving scale adherence and scale growth should be determined.

The self-diffusion rates of Co, Cr, Si and Y in CoO, Cr_2O_3, SiO_2 and also through $CoO-CoCr_2O_3$ and $CoO-Co_2SiO_4$ oxides should be determined and correlated with observed growth rates of cobalt-based alloys. This information is of primary importance in any study concerning the solid state diffusion processes in the scale.

REFERENCES

1. Stetson, A. R. and V. S. Moore, Gas Turbine Materials Conference, Naval Ship Engineering Center, 43 (1972).

2. Felix, W., "The Role of Materials in Gas Turbine Engineering," High Temperature Materials in Gas Turbine, 18 (1974).

3. Kerr, T. W., M.Sc. Thesis, The Pennsylvania State University (1975).

4. Hock, V. F., M.Sc. Thesis, The Pennsylvania State University (1977).

5. Wright, I. G., "Development of Dispersion Strengthened CoCrAl Alloys for Combined High Temperature Oxidation and Hot Corrosion Resistance," Proceedings of the 1974 Gas Turbine Materials in the Marine Environment Conference, Metals and Ceramics Information Center, Battelle, Columbus Laboratories, MCIC-75-27, pp 357-378 (1974).

6. Wheatfall, W. L., "Are Cobalt-Base Alloys Intrinsically More Resistant to Hot Corrosion than Alloys Based on Nickel," AGARD Conference Proceedings, No. 120 (1973).

7. Giggons, C. S., B. H. Kear, F. S. Pettit, and J. K. Tein, Met. Trans, 5, 1685 (1974).

8. Tammann, G., Z. Anorg. U. Allgem. Chem., 111, 78 (1920).

9. Pilling, N. B. and R. E. Bedworth, J. Inst. Metals, 29 (1923).

10. Wagner, C., Z. Physik. Chem., B21, 25 (1933).

11. Wagner, C., "Atom Movements," Amer. Soc. Metals, Cleveland (1951).

12. Kofstad, P., High Temperature Oxidation of Metals, Wiley, New York (1966).

13. Douglass, D. L., Oxidation of Metals and Alloys, Amer. Soc. Metals, Metals Park, Ohio (1971).

14. Kubaschewski, O. and B. E. Hopkins, Oxidation of Metals and Alloys, 2nd ed., Butterworths, London (1967).

15. Hauffe, K., Oxidation of Metals, Plenum Press (1965).

16. Wagner, C. and W. Schottky, Z. Physik. Chem., B11, 163 (1930).

17. Mahorter, R. G., Proceedings of the 1974 Gas Turbine Materials in the Marine Environment Conference, Metals and Ceramics Information Center, Battelle, Columbus Laboratories, MCIC-75-27, pp 1-10 (1974).

18. Wagner, C. and E. Koch, Z. Physik. Chem., 32B, 439 (1936).

19. Carter, R. E. and F. D. Richardson, J. Metals, 6, 1244 (1954).

20. Carter, R. E. and F. D. Richardson, Trans. A.I.M.E., 200, 1244 (1954).

21. Carter, R. E. and F. D. Richardson, Trans. A.I.M.E., 203, 336 (1955).

22. Bridges, D. W., J. P. Baur, and W. M. Fassel, Jr., J. Electrochem. Soc., 103, 614 (1956).

23. Wagner, C., J. Electrochem. Soc., 99, 369 (1952).

24. Wagner, C., Z. Electrochem. Soc., 63, 772 (1959).

25. Wagner, C., J. Electrochem. Soc., 103, 627 (1956).

26. Whittle, D. P., M. E. El-Dahshan, and J. Stringer, Corrosion Science, 17, 879 (1977).

27. Jones, D. E. and J. Stringer, Oxidation of Metals, 9, 5, 409 (1975).

28. Allam, I. M., D. P. Whittle, and J. Stringer, Oxidation of Metals, 9, 1 (1978).

29. Irving, G. N., J. Stringer, and D. P. Whittle, Corrosion Science, 15, 337 (1975).

30. Angerman, C. L., Oxidation of Metals, 5, 2, 149 (1972).

31. Irving, G. N., J. Stringer, and D. P. Whittle, Oxidation of Metals, 8, 6, 393 (1974).

32. El-Dahshan, M. E., D. P. Whittle, and J. Stringer, Corrosion Science, 16, 77 (1976).

33. Lowell, C. E. and D. L. Deadmore, Oxidation of Metals, 7, 1, 55 (1973).

34. Douglass, D. L. and J. S. Armijo, Oxidation of Metals, 2, 2, 207 (1970).

35. Beltran, A. M., Cobalt, 46, 3 (1970).

36. Sims, Chester T. and William C. Hagel (Editors), The Superalloys John Wiley and Sons, New York, New York (1972).

37. El-Dahshan, M. E., J. Stringer, and D. P. Whittle, Cobalt, 4, 86 (1974).

38. Giggins, C. S. and F. S. Pettit, Met. Trans., 1071, 3 (1971).

39. Stringer, J., B. A. Wilcox, and R. I. Jaffee, Oxidation of Metals, 5, 11 (1972).

40. Bornstein, N. S., M. A. DeCrescente, and H. A. Roth, In: Proceedings of the 1974 Gas Turbine Materials in the Marine Environment Conference, Metals and Ceramics Information Center, Battelle, Columbus Laboratories, MCIC-75-27, pp 115-160 (1974).

41. Goebel, J. A., E. J. Felton, and F. S. Pettit, In: Proceedings of the 1974 Gas Turbine Materials in the Marine Environment Conference, Metals and Ceramics Information Center, Battelle, Columbus Laboratories, MCIC-75-27, pp 93-114 (1974).

42. DeCrescente, M. A. and N. S. Bornstein, Corrosion, 24, 5, 127 (1968).

43. Johnson, D. M., D. P. Whittle, and J. Stringer, Corrosion Science, 15, 721 (1975).

44. Goebel, J. A. and F. S. Pettit, Met. Trans., 1, 1943 (1970).

45. Goebel, J. A., F. S. Pettit, and G. W. Goward, Met. Trans., 4, 261 (1973).

46. Danek, G. J., Jr., Journal Navel Engineering, 12 (1965).

47. Seybolt, A. U., Trans. Metall. Soc., A.I.M.E., 242, 1955 (1968).

48. Quets, J. M. and W. H. Dresher, J. Mater., 4 (1969).

49. Pontony, D. A. and K. I. Vasu, J. Inorg. Nucl. Chem., 30 (1968).

50. Vialatte, M. and C. Apert, Corrosion et Anticorrosion, 14 (1966).

51. Stringer, J. and D. P. Whittle, High Temperature Materials in Gas Turbines, eds. P. R. Sahm and M. O. Speidel, Elsevier Scientific Publishing Co., Amsterdam, pp 283-311 (1974).

52. Dibs, R. R., "Dynamic Gas Temperature Measurements in a Gas Turbine Transition Duct Exit," American Society of Mechanical Engineers, paper no. 73-GT-7 (1972).

53. Tschinkel, J. G., Corrosion, 28, 5, 161 (1972).

54. Bornstein, N. S., M. A. DeCrescente, and H. A. Roth, Corrosion, 28 7, 265 (1972).

55. DeCrescente, M. A. and N. S. Bornstein, Corrosion, 24, 5 (1968).

56. Johnson, D. M., D. P. Whittle, and J. Stringer, Corrosion Science, 15, 649 (1975).

57. Stringer, J., M. E. El-Dahshan, and I. G. Wright, Oxidation of Metals, 8, 6, 361 (1974).

58. El-Dahshan, M. E., J. Stringer, and D. P. Whittle, Oxidation of Metals, 8, 4, 211 (1974).

59. El-Dahshan, M. E., D. P. Whittle, and J. Stringer, Oxidation of Metals, 8, 4, 179 (1974).

60. Elliott, P. and S. K. Verma, Corrosion Science, 16, 1 (1976).

61. Bornstein, N. S. and M. A. DeCrescente, Trans. A.I.M.E., 245, 947 (1969).

62. Johnson, D. M., D. P. Whittle, and J. Stringer, Werkstoffe und Korrosion, 26, 8, 611 (1975).

63. Davin, A., D. Coutsourradis, and L. Habraken, Cobalt, 35, 69 (1967).

64. Goward, G. W., Journal of Metals, 10, 31 (1970).

65. Bergman, P. A., Corrosion, 23, 72 (1967).

66. Huang, T., E. A. Gulbransen, and G. H. Meier, Journal of Metals 28 (1979).

67. Beltran, A. M., Cobalt, 46, 3 (1970).

68. Johnson, D. M., D. P. Whittle, and J. Stringer, Corrosion Science, 15 (1975).

69. Seybolt, A. U., "Na_2SO_4-Superalloy Corrosion Mechanism Studies," General Electric Technical Information Series 70-C-189 (June 1970).

70. Seybolt, A. U., Corrosion Science, 11, 751 (1971).

71. Bornstein, N. S., M. A. DeCrescente, and H. A. Roth, "Hot Corrosion of Vanadium Pentoxide and Sodium Sulfate," Contract N-00014-70-C-0234, NR-036-089/1-12-70 (1971).

72. Miner, R. V., Jr., Metallurgical Transactions A, 1950, 8, 1949 (1977).

73. Lowell, C. E., Oxidation of Metals, 7, 95 (1973).

74. Giggins, C. S. and F. S. Pettit, Trans. A.I.M.E., 345, 2495 (1969).

75. Wagner, C., Corrosion Science, 5, 751 (1965).

76. Wood, G. C., Oxidation of Metals, 2, 11 (1970).

77. Kofstad, P. K. and A. Z. Hed, J. Electrochem. Soc., 116, 224, 229 (1969).

78. Bridges, D. W., J. P. Baur, and W. M. Fassell, Jr., J. Electrochem. Soc., 103, 614 (1956).

79. Touloukian, Y. S., Ed., "Oxides and Their Solutions," Thermophysical Properties of High Temperature Materials, Vol. 4, Research Center, Purdue University (1967).

DISTRIBUTION

Commander (NSEA 09G32)
Naval Sea Systems Command
Department of the Navy
Washington, D.C. 20362 — Copies 1 and 2

Commander (NSEA 0342)
Naval Sea Systems Command
Department of the Navy
Washington, D.C. 20362 — Copies 3 and 4

Defense Technical Information Center
5010 Duke Street
Cameron Station
Alexandria, VA 22314 — Copies 5 through 16